

Bent Laue X-ray Beam Expander

A Dissertation Submitted to
the College of Graduate Studies and Research
in Partial Fulfillment of the Requirements
for the degree of Doctor of Philosophy
in the
Department of Physics and Engineering Physics
University of Saskatchewan
Saskatoon

By

Mercedes Martinson

Saskatoon, SK

Canada

© Copyright Mercedes Martinson, 2016. All rights reserved.

Permission to Use

In presenting this thesis in partial fulfilment of the requirements for a Postgraduate degree from the University of Saskatchewan, I agree that the Libraries of this University may make it freely available for inspection. I further agree that permission for copying of this thesis in any manner, in whole or in part, for scholarly purposes may be granted by the professor or professors who supervised my thesis work or, in their absence, by the Head of the Department or the Dean of the College in which my thesis work was done. It is understood that any copying or publication or use of this thesis or parts thereof for financial gain shall not be allowed without my written permission. It is also understood that due recognition shall be given to me and to the University of Saskatchewan in any scholarly use which may be made of any material in my thesis.

Requests for permission to copy or to make other use of material in this thesis in whole or part should be addressed to:

Head of the Department of Physics and Engineering Physics
116 Science Place
University of Saskatchewan
Saskatoon, Saskatchewan
Canada
S7N 5E2

Abstract

Synchrotron imaging beamlines around the world all suffer from a similar limitation, namely a beam that is smaller in the vertical direction than the horizontal. This can produce a beam that is so small in the vertical direction that some imaging applications are limited or even impossible. At the BioMedical Imaging and Therapy (BMIT) beamline facility at the Canadian Light Source (CLS), the vertical beam sizes on the Bend Magnet (BM) and Insertion Device (ID) beamlines are 7 mm and 11 mm, respectively. This limited vertical beam size results in several limitations. Micro-computed-tomography experiments requiring multiple rotations to produce a full three-dimensional representation of the sample result in longer scan times and possible reconstruction errors due to misalignment between rotations. Similarly, projection images requiring vertical scans to cover the entire two dimensional field of view extend acquisition times and lead to potential stitching errors between exposures. Dynamic phase-based imaging (*i.e.* movies), which are being used for some of the most cutting edge biomedical imaging research taking place worldwide, is virtually impossible with samples larger than the vertical beam size.

This problem has been solved at other synchrotrons by building very long beamlines and allowing the beam to naturally diverge to a larger field of view, however this was not possible for BMIT due to budgetary and geographical limitations. In order to vertically expand the beam, a bent Laue double crystal monochromator was used in a non-dispersive divergent geometry to ultimately produce a beam expansion of 12 \times the incident height. Improvements were made to the system to preserve the quality of transverse coherence in the beam, allowing phase-based imaging techniques to be performed with a larger field of view. This was achieved by carefully matching the geometric and single-ray focal points in the so-called “magic condition.”

The quality of the expanded beam was compared to that produced by the beamline’s standard flat Bragg double crystal monochromator and was found to differ in divergence by less than 10% between the two monochromator systems. Further testing was done to evaluate the criticality of matching the two focal types, and to determine at least a minimum energy range over which the system could be used reliably. These tests showed that the system is much more flexible than previously believed, with energy ranges of at least ± 5 keV producing images wherein the vertical and horizontal edge width differ by less than 1%, indicating that the expander does not adversely affect the beam in the diffraction plane. Despite the improvement to the diffraction and focus characteristics of the system, there was an ongoing issue with areas of missing intensity in the beam. The hypothesis that this was caused by imperfect bending of the second crystal has been confirmed using diffraction and mechanical measurement techniques.

Acknowledgements

Special thanks to my supervisor Dr. Dean Chapman whose passion for physics and instrumentation were an inspiration throughout this journey, and co-supervisor Dr. Paul Babyn for encouraging my collaboration with the Monash University's lung imaging group.

I am grateful for the excellent support received from Dr. George Belev and the other CLS staff who contributed to the work; for the experimental assistance from The Ritchie Centre's Lung Development group for their help with the lung imaging experiment; to Dr. Melanie van der Loop and Dr. Gurpreet Aulakh for their animal handling assistance at CLS; and to the APS beamline staff for their assistance with the characterisation experiments.

Mercedes Martinson is a Fellow, and Dean Chapman and Paul Babyn are Mentors, in the Canadian Institutes of Health Research Training grant in Health Research Using Synchrotron Techniques (CIHR-THRUST). This work is supported in part by a Discovery Grant from the Natural Sciences and Engineering Research Council of Canada (NSERC) and by the Canada Research Chair program.

Data was collected in part at the Biomedical Imaging and Therapy bend magnet beamline (05B1-1) at the Canadian Light Source. Research described in this dissertation was performed at the Canadian Light Source, which is funded by the Canada Foundation for Innovation, NSERC, the National Research Council Canada, the CIHR, the Government of Saskatchewan, Western Economic Diversification Canada, and the University of Saskatchewan. Data was collected in part at BL20B2 of SPring-8 with the approval of the Japan Synchrotron Radiation Research Institute (JASRI) (Proposal No. 2013A1591). Data was collected in part at the Optics & Detector Testing Beamline (1-BM-B) at the Advanced Photon Source, Argonne National Laboratory. This research used resources of the Advanced Photon Source, a U.S. Department of Energy (DOE) Office of Science User Facility operated for the DOE Office of Science by Argonne National Laboratory under Contract No. DE-AC02-06CH11357.

Dedication

To my dad Terry for giving me logic genes, and
my mom Lea for the creativity genes to balance them out.

To my husband Grant for keeping me on this side of sanity
and putting a roof over my head throughout school.

Table of Contents

Permission to Use.....	i
Abstract.....	ii
Acknowledgements.....	iii
Dedication	iv
Table of Contents	v
List of Tables	vii
List of Figures	viii
List of Abbreviations & Symbols.....	x
Chapter 1 Introduction	1
1.1 Motivation	1
1.2 Background	2
1.2.1 Diffraction of x-rays from perfect crystals.....	2
1.2.2 Crystal geometries and sign conventions.....	3
1.2.3 Geometric and single-ray foci	4
1.2.4 Inspiration for bent Laue method to expand the beam	5
1.2.5 Monochromators	6
1.3 Other methods of expanding an x-ray beam.....	7
1.3.1 Distance	7
1.3.2 Asymmetric flat Bragg diffraction	7
1.3.3 Curved mirrors	9
Chapter 2 Project Inspiration & Objectives, Summary of Manuscripts	12
2.1 Project Motivation & Objectives	12
2.1.1 Inspiration.....	12
2.1.2 First objective: Expand the beam	12
2.1.3 Second objective: Fix the beam.....	12
2.1.4 Third objective: Evaluate the beam.....	13
2.1.5 Fourth objective: Upgrade the beamline	13
2.2 Summary of Manuscripts	14
2.2.1 Indirect measurement of average alveolar dimension using dynamic phase-contrast imaging (Chapter 3)	14
2.2.2 Development of a bent Laue beam-expanding double-crystal monochromator for biomedical X-ray imaging (Chapter 4).....	14
2.2.3 Phase-preserving beam expander for biomedical X-ray imaging (Chapter 5).	15
2.2.4 Measuring the criticality of the “magic condition” for a beam expanding monochromator (Chapter 6)	16
2.2.5 Characterisation of a bent Laue double crystal monochromator (Chapter 7).	16
Chapter 3 Indirect measurement of average alveolar dimension using dynamic phase-contrast imaging	18
3.1 Introduction	19
3.2 Methods	20
3.3 Results.....	21
3.4 Discussion.....	21
3.5 Conclusion	22

Chapter 4 Development of a Bent Laue Beam Expanding Double Crystal Monochromator for Biomedical X-ray Imaging	23
4.1 Introduction	24
4.2 Design & Implementation	24
4.3 Results.....	27
4.4 Discussion	30
4.5 Conclusion	31
Chapter 5 Phase Preserving Beam Expander for Biomedical X-ray Imaging	33
5.1 Introduction	34
5.2 Background Theory.....	34
5.3 Design & Implementation	38
5.4 Image Analysis and Results	40
5.5 Conclusion	43
Chapter 6 Measuring the criticality of the ‘magic condition’ for a beam expanding monochromator.....	44
6.1 Introduction	45
6.2 Experimental procedure.....	46
6.3 Analysis.....	46
6.4 Discussion	46
6.5 Conclusion	48
Chapter 7 Characterisation of a bent Laue double crystal beam expanding monochromator	49
7.1 Introduction	49
7.2 Background	50
7.3 Finite Element Analysis	51
7.4 Mechanical measurements.....	52
7.5 Bent crystal rocking curve measurements (Bragg-Bragg mode).....	53
7.6 Bent crystal rocking curves (Laue-Laue mode).....	55
Chapter 8 Conclusion & Future work.....	58
8.1 Conclusions.....	58
8.2 Future Research	59
References.....	61
Appendix I Reuse Licenses for Papers and Figures.....	66
Appendix II Technical & experimental details for installation & testing	72

List of Tables

Table 3.1 PCXI and μ -CT results	21
Table 4.1 Summary of expansion results and energy parameters.....	29
Table 5.1 Summary of analysis results	42
Table 6.1 Peak widths of phase and knife edge images as a function of Bragg angle	47

List of Figures

Figure 1.1 Orientations of concavity relative to source, S, in (a) Cauchois geometry with virtual geometric focus (fg) and (b) focusing geometry with real geometric focus.	4
Figure 1.2 (a) Lower-sign and (b) Upper-sign orientations.....	4
Figure 1.3 Single-ray focus in (a) focusing and (b) diverging geometries.....	5
Figure 1.4 Asymmetric crystal beam expander	8
Figure 1.5 Arrangement of Kirkpatrick-Baez (K-B) mirror (figure courtesy of OSA, {Kirkpatrick 1948}).....	10
Figure 3.1 Average alveolar volume as a function of lung divergence.....	21
Figure 4.1 Schematic of crystal geometry and orientation, ray tracing diagrams, and focal lengths.	25
Figure 4.2 Burn paper images showing beam quality. (a) Extreme example of non-uniform intensity. (b) Beam “glitches.” (c) Large (~40 mm) beam with uniform intensity.....	28
Figure 4.3 Micro-CT image of a pine cone. Image was captured in a single rotation. View A is an axial slice, view B is a sagittal slice. The vertical field of view of 21.15 mm would require 7 rotations to capture without beam expansion.	28
Figure 4.4 Flat-dark corrected frame from a movie of a live mouse captured with 200 μm flat panel detector (Hamamatsu C9252DK-14) at 30 fps. Movie sample available in additional data online. Vertical line on the right is an artefact of the detector, not the beam.	29
Figure 4.5 Vertical and horizontal knife edge placed at (A) 140 mm and (B) 5135 mm sample-detector distance.....	31
Figure 5.1 Subfigure (a) depicts the geometric (virtual) focus of two incoming monochromatic rays by a bent Laue crystal. Subfigure (b) depicts the single-ray (virtual) focus of a polychromatic beam by a bent Laue crystal. Subfigure (c) depicts the two crystals aligned such that the single-ray and geometric foci of the first crystal coincide with each other and with the geometric focus of the second crystal. The first crystal satisfies the “magic condition.”	35
Figure 5.2 Upper-sign and Lower-sign geometries.	36
Figure 5.3 Polychromatic focus diagram.....	37
Figure 5.4 (a) First crystal (vacuum-compatible) and (b) second crystal mounted on rigid frame benders. In each figure, the wafers are 5” diameter. As shown, the beam would be coming out of the page.....	39
Figure 5.5 Expanded beam at BMIT-ID beamline on fluorescent paper with cm-scale major grid lines.	39
Figure 5.6 Flat-corrected phase and knife edge images used for analysis, also demonstrates field of view of respective monochromators. (a,b) bent Laue monochromator, (c,d) flat Bragg	

monochromator; (a,c) Lucite Rods, (b,d) Tungsten block. Propagation distance is 134cm. All images have the same scale.....	40
Figure 5.7 Plot profiles with relative intensity on y-axis and pixel range on x-axis. Image type: [K]nife edge or [P]hase fringe. Edge normal: [V]ertical or [H]orizontal. Monochromator type: [B]eamline or [E]xpander. (a) PVE & PVB (b) PHE & PHB (c) KVE & KVB (d) KHE & KHB.....	41
Figure 5.8 Phase image of euthanised mouse. Propagation distance approximately 200cm.	42
Figure 6.1 Experimental setup.....	45
Figure 6.2 Sample (a) phase and (b) knife edge images.....	47
Figure 7.1 Schematic of bent Laue double crystal system.....	50
Figure 7.2 (a) Double-diffracted expanded beam showing intensity distribution due to distortion in crystal. Areas B and C show low and high intensity, respectively, and corresponding reflectivity curves (b) overlapping and (c) failing to adequately overlap.....	51
Figure 7.3 3D physical mapping of 5 m bend radius crystal surface. Colour represents distance in mm from a plane fit parallel to viewing angle and normal to centre of surface. Due to inconsistencies in the measurements, exact distortion cannot be quantified, but is easily visible in the mapping, along with anticlastic bending along the side edges.....	52
Figure 7.4 Variation of Berg-Barrett topography with bent crystal.	53
Figure 7.5 Bragg-Bragg bent crystal rocking curves. (a) 5 m bend radius; note severe distortion in lower-left corner and oscillating distortion along top edge. (b) 0.5 m bend radius; anti-clastic bending evident along sides and corners.....	54
Figure 7.6 Variation of Lang topography with bent crystal.	55
Figure 7.7: Laue-Laue bent crystal rocking curves. (a) 5 m bend radius; the areas of uniformly low intensity at the top and bottom of the 5 m image are caused by absorption in the Aluminium frame. (b) 0.5 m bend radius; Laue-diffracted rays are nearly perfectly straight and parallel.....	56
Figure II.1 Diagram of (a) 0.5 m and (b) 5.636 m bending frames and related components	73
Figure II.2 Beamline diagram {Bmit 2016}.....	74
Figure II.3 Orientation of crystal on frame, looking at the convex side of the second crystal. Shown is older wafer with two flats. Single flat on newer wafers corresponds to shorter flat (lower-right).	74
Figure II.4 Template for mounting crystal to frame.	76
Figure II.5 Laue transmission mapping for (5,1,1) crystal perpendicular to the beam, showing the (3,1,1) reflection below the direct beam which is marked by the cross at the centre.....	77
Figure II.6 Stereographic projection of Si(5,1,1) wafer with (3,1,1) reflection on the perimeter....	77

List of Abbreviations & Symbols

2D / 2d	Two-dimensional
3D / 3d	Three-dimensional
APS	Advanced Photon Source
BM	Bend magnet (beamline)
BMIT	BioMedical Imaging (and) Therapy (facility)
BP	Bragg planes
CIHR	Canadian Institutes (of) Health Research
CLS	Canadian Light Source
cmH ₂ O	centimetres of water (a unit of pressure)
CT	Computed tomography
d	Spacing of the Bragg planes
Δf	Distance between crystals
$\Delta\theta_{\text{rot}}$	Unmodified change in Bragg angle as x-ray traverses crystal
$\Delta\theta'_{\text{rot}}$	Modified change in Bragg angle as x-ray traverses crystal
DOE	(U.S.) Department of Energy
ESRF	European Synchrotron Radiation Facility
f	Focal length non-specified
f_{11}	Object distance for first crystal
f_{12}	Image distance for first crystal
f_{21}	Object distance for second crystal
f_{22}	Image distance for second crystal
f_g	Geometric focal length
f_p	Polychromatic or single-ray focal length
f_s	Distance from source to first crystal
FOV	Field of view
FWHM	Full-width at half-max
FZ	Float zone
H	Height of expanded beam
h	Height of incident beam
HU	Hounsfield unit (a measure of pixel intensity)
θ_B	Bragg angle
θ_c	Critical angle
θ_i	Incident angle between surface and beam
ID	Insertion device (beamline)
JASRI	Japan Synchrotron Radiation Research Institute

KES	K-edge subtraction
keV	Kiloelectronvolt
L	Footprint of beam on asymmetric crystal beam expander crystal
l_1	Path length of non-diffracted x-ray through crystal
l_2	Beam height of diffracted x-rays at exit surface of crystal
m	Expansion factor
mA	millamps (a unit of current)
mrad	milliradians (NB: millirads as unit of radiation not used in this work)
μm	micrometre
$\mu\text{-CT}$	micro-computed tomography
N	(Surface) Normal
NSERC	Natural Sciences and Engineering Research Council of Canada
NIST	National Institute of Standards and Technology
ν	Poisson ratio
OSA	The Optical Society (sic)
pA	picoamps (a unit of current)
ph	photon
PCXI	Phase-based x-ray imaging
PIV	Particle image velocimetry
R	Bend radius
ROI	Region of interest
ρ	Bend radius
ρ_i	Bend radius of i th crystal ($i = 1,2$)
S	Source
Si	Silicon
SKES	Spectral K-Edge Subtraction
SNR	Signal-to-noise ratio
SPring-8	Super Photon Ring – 8 GeV
T	Crystal thickness
THRUST	Training (grant in) Health Research Using Synchrotron Techniques
UCACS	University Committee on Animal Care and Supply
W	Width of expanded beam
w	Width of incident beam
χ	Asymmetry angle

Chapter 1 Introduction

This dissertation presents a novel bent Laue double-crystal monochromator system used to vertically expand the x-ray beam at the BioMedical Imaging and Therapy (BMIT) facility at the Canadian Light Source (CLS).

1.1 Motivation

BMIT has an established track record of successful biomedical imaging experiments. Yet since its inception it, as well as most synchrotron imaging facilities, has suffered a severe limitation in its vertical beam height. This limitation is often overcome with distance (*i.e.* a long beamline) but at great expense. BMIT consists of two beamlines: a bend magnet (BM) and a wiggler insertion device (ID). The BM and ID beams reach maximum heights of approximately 6 mm and 11 mm, respectively. The vast majority of imaging samples (*e.g.* mice, rabbits, pigs) are significantly larger than the vertical beam size. This requires vertical scanning of imaging samples (*i.e.* moving the samples vertically through the fixed beam while taking multiple images throughout the travel distance), which raises challenges in both data collection and analysis. For projection (2D) imaging, this requires multiple images to be stitched together in post-processing. This process is error-prone and reduces the quality of the final images. For 3D computed tomography (CT) imaging, this requires multiple slices to be captured in succession. For high-resolution imaging, a single slice can take upwards of an hour, meaning that a limited number of slices can be captured between refills of the synchrotron ring. This imposes limits on the amount of data that can be captured during a user shift and can lead to experimental designs that are limited by the apparatus.

But by far the biggest disadvantage of the small vertical extension of the beam is for live-animal dynamic phase-based imaging, *i.e.* movies. These are used to carry out the most cutting-edge biomedical imaging experiments being performed worldwide and are improving our understanding of the function of biological systems, *e.g.* respiration and blood flow. These techniques require a full field view of the imaging sample with an x-ray beam that has a high degree of transverse coherence. While the synchrotron x-ray beams produced at the BMIT beamlines has the transverse coherence necessary to perform phase-based imaging techniques, its field of view is simply too limited to image the entire biological systems under investigation (*e.g.* respiratory or circulatory systems). Thus it was suggested that a vertical beam expander be developed in order to increase the field of view and make BMIT competitive with facilities such as SPring-8 or the European Synchrotron Radiation Facility (ESRF) which feature long beamlines that naturally expand the beam. An example of the type of imaging experiments that can be done with a full field beam is presented in Chapter 3.

1.2 Background

1.2.1 Diffraction of x-rays from perfect crystals

The theory of x-ray diffraction can be grouped into two main classes: dynamical diffraction and kinematic diffraction {Als-Nielsen 2001, Zachariasen 1945}. Von Laue's kinematic treatment {Von Laue 1915} covered the case for small crystals or mosaics of small crystals and neglects multiple scattering effects. Zachariasen's {Zachariasen 1945} treatment of the dynamical diffraction of x-rays was developed for larger perfect crystals {Ekstein 1942} that have long range atomic periodicity and accounted for multiple scattering effects and refraction. Penning & Polder {Penning 1961} developed theory for weakly strained crystals that fall between these two extremes and Suortti {Suortti 1992} introduced the application of lamella models to bent crystals used as synchrotron focusing monochromators. While the relatively large crystals used in this work are considered to be perfect (*i.e.* free from defects), the severe bending that they undergo transitions their treatment to the kinematic regime {Petrashen 1979}.

There are two modes of diffraction by perfect crystals: the Laue case refers to transmission mode and occurs throughout the depth of the crystal, and the Bragg case refers to reflection mode and occurs in the lattices near the surface. Both cases follow Bragg's Law (Equation 1.1) of crystal diffraction, where λ is the wavelength, d_{hkl} is the lattice spacing of the (h,k,l)-type reflection, and θ_B is the angle between the incident x-ray and the Bragg planes.

$$\lambda = 2d_{hkl}\sin \theta_B \quad 1.1$$

When a perfect crystal with a specific d-spacing is rocked (*i.e.* rotated in the diffraction plane) against a monochromatic beam (*i.e.* fixed wavelength), it's possible to get reflection at angles away from the exact Bragg angle dictated by the d-spacing. This produces a reflectivity curve that peaks at θ_B and falls off on either side. The width of this peak is referred to as the (angular) Darwin width. In the Laue case, the Darwin peak is typically sharp and narrow, which can create difficulties in aligning multiple crystals. However by bending the crystal, the angular width can be increased by an order of magnitude {Ren 1998}, resulting in higher intensity in the outgoing rays.

This increase in reflectivity angular width comes from the change in lattice plane orientation that an x-ray encounters as it penetrates the crystal. As will be explained in greater detail in Chapter 5, an x-ray traversing a bent crystal sees a change in Bragg angle due to lattice plane bending, compression/expansion of the planes, and small changes in d-spacing (Equation 5.3). These all work together to increase the range of crystal rocking angles at which x-rays of a

particular energy will be diffracted, while reducing the number of locations in the crystal at which a particular Bragg angle is simultaneously achieved. This has the overall effect of widening the angular width while flattening the reflectivity peak, maintaining an overall constant integrated reflectivity equal to the area under the reflectivity curve. This widening and flattening of the peak is what provides more leeway when aligning multiple crystals, however these improvements come at a cost of decreased monochromaticity and slightly increased divergence in the beam.

Another important concept is that of symmetric and asymmetric crystals. When the Bragg planes are parallel (in the Bragg case) or perpendicular (in the Laue case) to the surface, the crystal is said to be symmetric. Otherwise the crystal is said to be asymmetric and the non-zero angle between the Bragg planes and the surface (Bragg case) or surface normal (Laue case) is referred to as the asymmetry angle and denoted χ . An asymmetry angle can be produced in two ways, either offcut from a larger crystal at the desired angle to produce an inherently asymmetric crystal, or else by using an inherently symmetric crystal with a reflection that is naturally asymmetric to the surface. In this way, the descriptions symmetric and asymmetric are intrinsic to the crystal but can also depend on its orientation to the x-ray beam. For example, in this dissertation a common crystal-reflection pair is the Si(5,1,1) crystal with a (3,1,1)-type reflection. The (5,1,1)-reflection is symmetric to the surface, however the (3,1,1)-reflection naturally occurs at 3.33° from the surface normal. Another crystal-reflection pair used was a Si(2,2,0) crystal with a (1,1,1)-type reflection cut at a 5° angle to the surface.

1.2.2 Crystal geometries and sign conventions

There are two main factors that affect the signs of variables used in understanding the focusing behaviour of cylindrically bent Laue crystals (Equations 1.2 & 1.3). These are the direction of the concavity relative to the source, and the orientation of the Bragg planes relative to the incoming x-rays.

When the source is on the concave side of the bent crystal, it is said to be in Cauchois geometry {Cauchois 1932} (Figure 1.1.a), and when the source is on the convex side of the bent crystal, it is said to be in focusing geometry {Aristov 1978} (Figure 1.1.b). The focus equations follow the usual sign convention for the focus, *i.e.* that a positive focal length value indicates a real focus on the opposite side of the crystal from the source and a negative value indicates a virtual focus on the same side of the crystal as the source.

Further to which side of the concavity faces the source, focus is also affected by the relative orientation of the Bragg planes (BP), the incident x-ray from the source (S), and the

surface normal (N). Geometrically (Figure 1.2), the crystal is said to be in lower-sign geometry when the incident ray is between the surface normal and the Bragg plane; and in upper-sign geometry when the Bragg plane is between the incident ray and the surface normal. Mathematically, the upper- / lower-sign convention refers to the angle ($\chi \pm \theta_B$) between the incident x-ray and the surface normal. This sign convention is used throughout this dissertation.

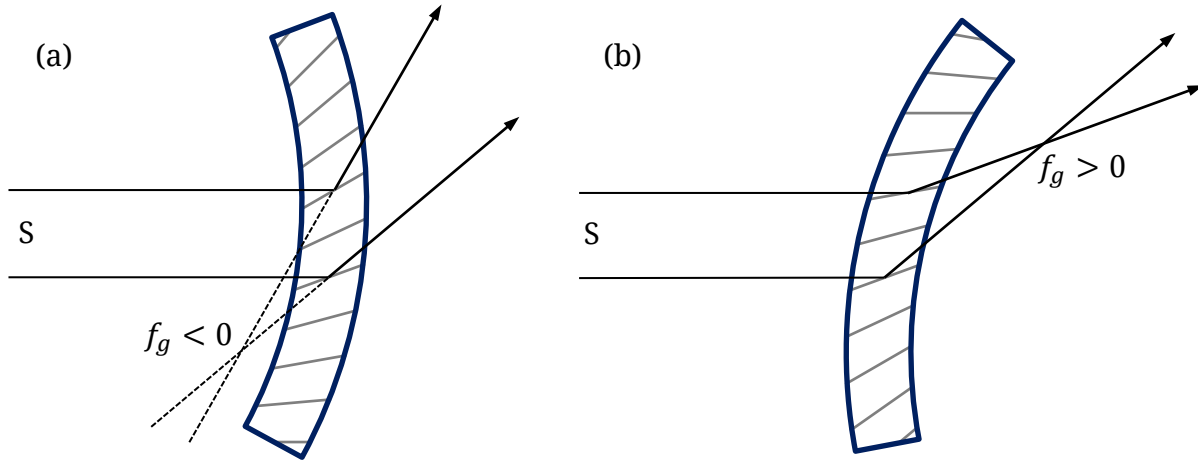


Figure 1.1 Orientations of concavity relative to source, S , in (a) Cauchois geometry with virtual geometric focus (f_g) and (b) focusing geometry with real geometric focus.

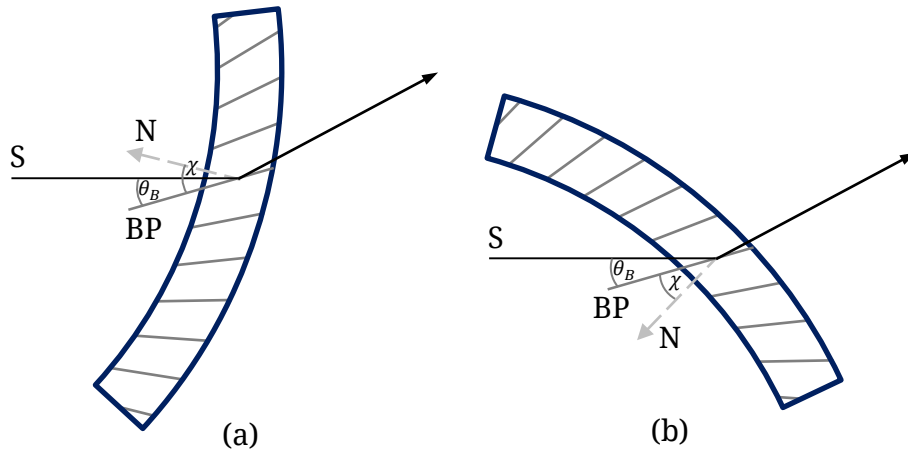


Figure 1.2 (a) Lower-sign and (b) Upper-sign orientations

1.2.3 Geometric and single-ray foci

Cylindrically bent crystals in a Laue diffraction arrangement exhibit two different types of focus. Geometric focus occurs from two independent x-rays incident at different positions on the crystal surface and in the plane of diffraction (Figure 1.1). The value of the geometric focal length f_g is given implicitly by Equation 1.2 {Schulze 1998}) and depends on the asymmetry angle χ , the

Bragg angle θ_B , the bend radius R (positive for focusing geometry, negative for diverging geometry), and the distance from the source to the crystal, f_s .

$$\frac{\cos(\chi \mp \theta_B)}{f_g} - \frac{\cos(\chi \pm \theta_B)}{f_s} = \frac{2}{R} \quad 1.2$$

Single-ray focus (Figure 1.3), on the other hand, is unique to x-ray diffraction and does not have an analogue in visible light optics. This type of focus occurs when a single polychromatic x-ray is diffracted by multiple reflections throughout the depth of the crystal. This is sometimes termed polychromatic focus (f_p), although this name is misleading as geometric focus also relies on the polychromicity of the incident beam. The single-ray focus can be real or virtual in both the Cauchois and focusing geometries, depending on the orientation of the incident beam to the surface normal and Bragg planes. More detail is provided in Chapter 5 along with full derivation of the single-ray focus Equation 1.3, but a key point is that the single-ray focus depends additionally on the Poisson ratio¹ ν . As the ray penetrates the crystal, it sees a continuous change in Bragg angle, resulting in x-rays of different energies being diffracted with a common focus.

$$f_p = \pm \frac{R \sin 2\theta_B}{2 \sin(\chi \pm \theta_B) + (1 + \nu) \sin 2\chi \cos(\chi \pm \theta_B)} \quad 1.3$$

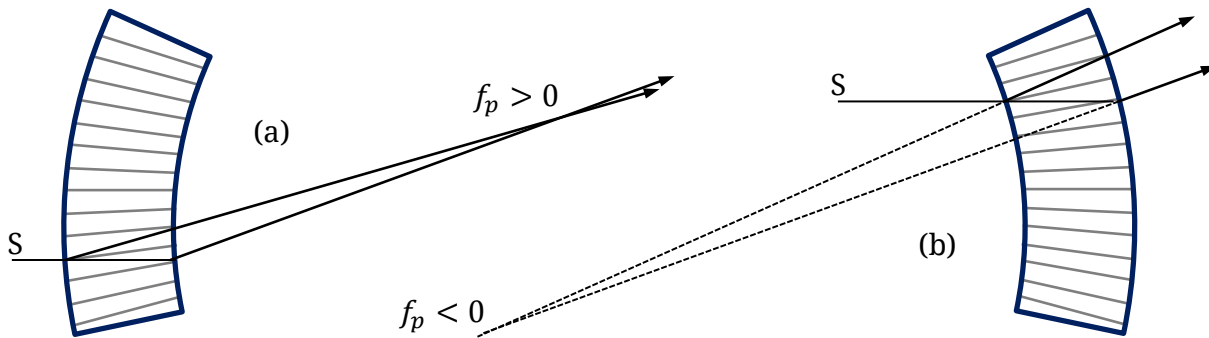


Figure 1.3 Single-ray focus in (a) focusing and (b) diverging geometries

1.2.4 Inspiration for bent Laue method to expand the beam

There are other ways to expand the beam, however these methods suffer limitations that prohibit their implementation on the BMIT beamlines (details in Section 1.3). Previous work {Zhu 2014} done by the research group on a Spectral K-Edge Subtraction (SKES) imaging system

¹ The Poisson ratio is a value that measures the tendency of the lattice planes to expand in the two directions perpendicular to the direction of compression, and which relates to the curvature in the diffraction plane of the lattice structure when the crystal is bent {Dolbow 1996}. It is treated here as isotropic, however the value is actually anisotropic and depends heavily on the cut and orientation of the crystal.

motivated a novel way to expand the beam using bent Laue crystal optics. In the SKES system, a single crystal is placed in the focusing geometry to create a narrow focused beam for imaging small animals at high resolution. The focus is made as small as possible by matching the single-ray and geometric focus, which also results in high energy dispersion. The system is then aligned to the absorption K-edge of a contrast agent, typically Iodine at 33.2 keV, and an imaging sample is placed at the focus. Transmission images are captured using a flat panel detector to create a 2-dimensional image in which each column is an absorption spectrum of a given position in the sample's cross-section. Using the jump in absorption as the energy crosses the K-edge of an element, an algorithm is implemented to map the regions in the imaging sample that contain the contrast agent.

Using our familiarity with the bent Laue optics implemented for the SKES project, it was proposed that a beam expanding system could be developed by reversing the crystal into Cauchois geometry to defocus the beam, and then placing a second crystal such that its geometric focus matches that of the first, allowing it to capture the expanded beam, thus returning it to horizontal and restoring the divergence of the source.

1.2.5 Monochromators

While complex multi-crystal synchrotron monochromators have been used to achieve high energy resolution, the most common types are either single crystal and double-crystal {Hastings 1977, Batterman 1991}. Within each of these, the crystals can be used in either Bragg or Laue mode, and the crystals can be either bent or straight, and symmetric or asymmetric. The advantage of symmetric crystals is the energy range, as an asymmetry angle limits the Bragg angle ($\theta_B < 90^\circ - \chi$). For this reason, asymmetry angles are typically small, on the order of 5° or less..

In a double-crystal system, the first crystal selects the energy by aligning to the Bragg angle for the desired wavelength; the purpose of the second crystal is primarily to return the beam to its incident direction, albeit with a vertical offset due to the monochromators. Some reflections can also capture harmonics, *i.e.* x-rays with energies that are integer multiples of a fundamental energy. As the reflectivity peaks of these harmonics is typically much narrower than the fundamental, the second crystal may be deliberately misaligned just enough to fall off the reflectivity peak for the harmonic, while staying within the peak for the fundamental {Bonse 1976}.

The most common type of beamline monochromator is a double-crystal flat Bragg symmetric monochromator {Beaumont 1974}, usually using (2,2,0)- or (1,1,1)-type reflections,

however double bent Laue monochromators are becoming more popular due to their higher bandwidth and resulting intensity {Illing 1995, Shastri 2002}. While it's possible to create single-crystal monochromators, these result in a beam that exits in a different direction than the source. For applications where the sample can be positioned arbitrarily, this is not necessarily a problem. However for imaging, it is desirable to keep the x-ray beam horizontal for ease of sample handling.

1.3 Other methods of expanding an x-ray beam

1.3.1 Distance

By far, the simplest way to achieve a large field of view is simply by building a longer beamline. Synchrotron x-ray beams have a divergence on the order of milliradians and given enough distance, the beam will naturally diverge to a large enough field of view to cover most small animal samples. This is the technique implemented at the SPring-8 BL20B2 (Medical and Imaging I) beamline, which extends 215 m into a separate building that contains the animal housing facilities {Goto 2001}. In order to match the level of expansion achieved in this thesis, the BMIT-BM beamline would have had to extend 300 m, placing it squarely in the Vaccine and Infectious Disease Organization (VIDO) building on campus. We considered asking nicely if they would tear down their building so we could make a better beamline, but thought better of it. In all seriousness, the major limitation of this method is cost. As it was, an addition was required to the CLS building in order to construct the BMIT facilities – increasing the length of the beam would have rendered the entire project cost-prohibitive.

1.3.2 Asymmetric flat Bragg diffraction

Expanding the beam using asymmetric reflections is regularly used in optical testing facilities {Spiga 2012} for applications such as rocking curve topography {Yamaguchi 2010, Kawado 2002, Kimura 1994}, where an asymmetric crystal (with an asymmetry angle comparable to the Bragg angle) is used to condition and expand the beam in order to fill a second crystal. This second crystal is then rocked in the Bragg plane and the resulting diffracted beam is recorded in some way (*e.g.* area detector or PIN diode).

The principle of asymmetric flat Bragg diffraction is based on the one-dimensional expansion of the beam when diffracted by an extremely asymmetric reflection in a perfect single crystal of silicon (Si) followed by reflection by a symmetric reflection of the same type to return the beam parallel to its incident direction. Two potential arrangements were proposed by Lewis et al. {Lewis 1990}, differing mainly by presence of a premonochromator that removes harmonics.

Horizontal expansion of a synchrotron x-ray beam using asymmetric flat Bragg diffraction was achieved experimentally by Christensen et al. {Christensen 1992} at the Synchrotron Radiation Source at Daresbury Laboratory, England. The beam was first conditioned using a single-crystal Si(111) monochromator which was calibrated using the known K-edges of copper, zinc, and nickel foils. The monochromatic beam then struck the beam expander crystal at a grazing angle of $\sim 1^\circ$ (Figure 1.4). While the most efficient use of the crystal's surface area occurs with a Bragg angle of $\theta_B = 45^\circ$, the horizontal polarisation of their beam motivated a compromise of $\theta_B = 60^\circ$. The experiment's target was an expansion of 50-100 \times in order to achieve an expanded beam of 100-200 mm from the 2.8 mm wide incident beam. Assuming an asymmetry angle χ and incident beam width w , the beam makes a footprint, L , on the expander crystal of:

$$L = \frac{w}{\sin(\theta_B - \chi)} \quad 1.4$$

This produces an expanded width of:

$$W = w \frac{\sin(\theta_B + \chi)}{\sin(\theta_B - \chi)} = L \sin(\theta_B + \chi) \quad 1.5$$

Which results in an expansion factor of:

$$M = \frac{W}{w} = \frac{\sin(\theta_B + \chi)}{\sin(\theta_B - \chi)} \quad 1.6$$

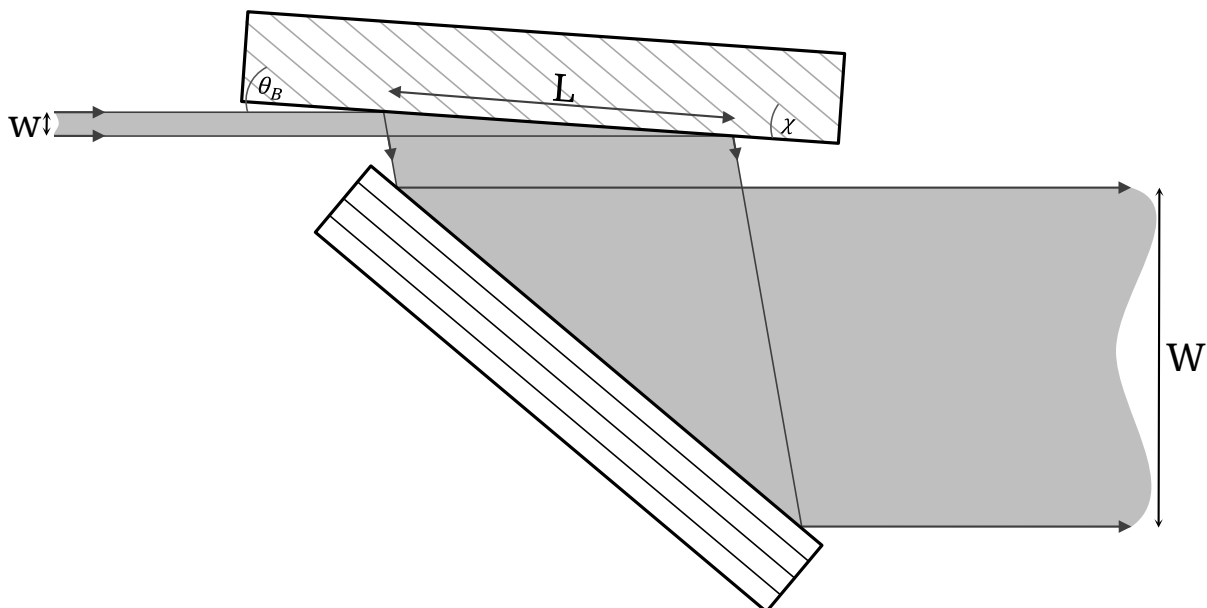


Figure 1.4 Asymmetric crystal beam expander

In principle, using $(\theta_B - \chi)$ values in the range of 0.5° - 1° , well above the critical angle² for total reflection at the energies used (6.85-11.41 keV), expansion of 50-100 \times could be achieved. In practice, the experiment achieved an expansion of 50 \times using a silicon crystal 98 mm long and 38 mm wide, cut from a silicon boule ~7.5 cm in diameter and ~10 cm long with the (111) planes perpendicular to the cylinder axis.

One major hurdle to using asymmetric crystals to expand the beam is a loss of intensity. While double-crystal monochromators are standard issue at many facilities, including BMIT, combining this with expansion results in the same number of photons being spread over a larger area. The intensity of the expanded beam is thus diminished by a factor equal to the expansion. For experiments in crystal optics or material science, this loss of intensity can be mitigated by longer exposure times; however biomedical experiments are more time-sensitive due to the considerations of working with live animals. As a major goal with the beam expander is to produce real-time movies of living subjects, these longer exposure times would be unacceptable.

Another important consideration is alignment. Flat Bragg diffraction has an extremely narrow Darwin width, meaning that the tolerance for misalignment is correspondingly tight. While it is technically possible, it is extremely difficult to maintain a stable system over long periods of time. For time-sensitive biomedical applications, the risk of losing alignment in the middle of a lengthy CT scan is simply too great for this technique to be viable. Reliable alignment of such a system may be beyond the current technical abilities of many beamlines.

1.3.3 Curved mirrors

The use of mirrors as x-ray optical devices was first proposed by Jentzsch as early as 1929 {Ehrenberg 1929}. Curved mirrors were not suggested as focusing elements until almost 20 years later in 1947 by Ehrenberg {Ehrenberg 1947}. The next year, Kirkpatrick and Baez³ {Kirkpatrick 1948} experimented with the use of concave mirrors with a spherical shape to create an x-ray microscope by focusing the beam to a small point and placing the imaging object at the focus, then allowing the beam's divergence to magnify the image. Two mirrors were placed at small grazing angles to the beam and in cross-planes in order to focus the beam in two directions (Figure 1.5) which together is termed a Kirkpatrick-Baez (K-B) mirror. This arrangement has since become a standard method to focus synchrotron x-ray beams around the world {Takeuchi 2003, Hignette 2003, Bianco 2002, Ascone 2003} using either cylindrical, toroidal, or elliptical mirrors. Such

² As with total internal reflection of optical light, an x-ray of a given energy, E_{keV} , incident upon any smooth surface will be totally reflected at incident angles below a critical angle, θ_c .

³ Albert Baez is the father of the popular folk singer Joan Baez

mirrors can also be used singly to focus the beam in only one direction {Schulze 1998}, or a combination of both single and K-B mirrors {Jiang 2007}.

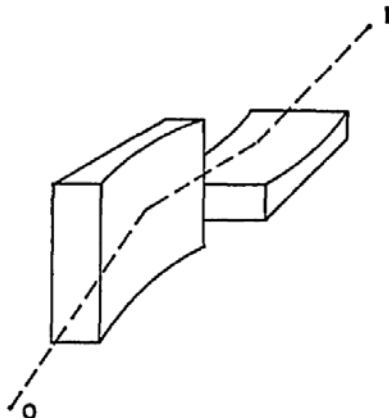


Figure 1.5 Arrangement of Kirkpatrick-Baez (K-B) mirror (figure courtesy of OSA, {Kirkpatrick 1948})

The mirrors are typically made by coating a substrate with a material that has a high atomic number, typically platinum or gold, but palladium and rhodium are also common {Kujala 2014, Liu 2005}. These are then highly polished to minimise scattering effects and increase reflectivity. These mirrors may also be multilayered, where alternating layers of high- and low-Z elements (e.g. W and C) are deposited to produce a periodic structure that diffracts the x-rays {Thompson 1987}.

A convex mirror could, in principle, be used to expand the x-ray beam in the vertical direction only, or a saddle-shaped mirror could even be used to expand the beam vertically while focusing it horizontally in order to increase the intensity of the beam and make use of the horizontal edges of the beam that are typically discarded. Indeed, toroidal mirrors for simultaneous horizontal and vertical beam shaping are widespread at synchrotron facilities. However the practical use of mirrors as x-ray optical components is limited by the angle between the beam and the mirror's surface. The critical angle decreases with increasing atomic number of the surface coating. Above this angle, the reflectivity effectively drops to zero. Conversely, for any given incident angle θ_i , there is a critical *energy* beyond which there is no reflection. For high Z surfaces (e.g. Au, Pd), the critical angle and energy are approximately related by {Batterman 1991}:

$$\theta_c \cdot E_{\text{keV}} = 77 \text{ mrad} \cdot \text{keV}$$

1.7

In focusing applications where curved mirrors are typically used, the incident beam has already been collimated or apertured in order to create a small footprint, allowing the mirrors to

be made at reasonable sizes. For the high energies used at BMIT (8-40 keV at BM, 20-100 keV at ID), a typical critical angle might be 2 mrad (at 40 keV). With an incident beam height of 6 mm, this would require a mirror 3 m long to cover the vertical extent of the incident beam. At the time of this writing, 400 mm is considered a “long” mirror {Mimura 2008} and 1.4 m is about the fabrication limit {Instrument_Design_Technology_Ltd. 2016, Crystal_Scientific 2011}, so fabricating such a large mirror with the necessary smoothness to preserve beam intensity is beyond current technical capabilities. If the technology did exist, the cost of such a mirror would be astronomical (no really – they use them for telescopes {Mao 1997}). Furthermore, spatial constraints inside the optics hutch would eliminate the possibility of such a large device.

Another limitation would be the heat load caused by the absorption of x-rays above the critical energy for a given incident angle. While the power load could be mitigated with beamline filters, this would greatly reduce the intensity, posing major limitations on the usefulness of such a system.

Chapter 2 Project Inspiration & Objectives, Summary of Manuscripts

2.1 Project Motivation & Objectives

2.1.1 Inspiration

The project was inspired by the work I did before transferring to a PhD. Dr. Robert Lewis had suggested that someone from the CLS visit Japan's SPring-8 synchrotron facility and their biomedical beamline (BL20B2), which has an excellent record of productivity and world class results, and try to translate some of their successful techniques back to the CLS. To this end, I began a mouse lung imaging project in collaboration with the Monash lung imaging group. The results of this work are published in Chapter 3.

When we considered replicating the experimental technique at the CLS, it quickly became clear that one reason for the success of the SPring-8 BL20B2 beamline is its large field of view, achieved by allowing the beam to naturally diverge over a 215 m distance to a beam size that can cover an entire mouse torso in both vertical and horizontal directions. In order to replicate these techniques at BMIT, its beams had to be expanded vertically to encompass entire small animal samples. To this end, further work on the PIV-CT project was put on hold in order to develop a beam expander system for BMIT. As the real estate and finances were not available to achieve this with a longer beamline, we sought a solution using bent Laue crystals.

2.1.2 First objective: Expand the beam

As a proof-of-principle, we first sought to demonstrate that the beam could be expanded using a double bent Laue system modelled on a Galilean telescope⁴. Silicon crystals were used for all experiments due to the availability of inexpensive, high-quality wafers from the semiconductor industry. The primary goal was to expand the beam vertically by at least 5× without specific regard to the divergence or transverse coherence of the beam. Secondary goals were to capture a live animal x-ray movie and to micro-CT an object larger than the incident beam in a single rotation in order to demonstrate the usability of the system. These goals were all achieved: we expanded the beam by 7×, imaged a live mouse using the expanded beam, and captured stunning 3D images of a pinecone. These results are presented in Chapter 4.

2.1.3 Second objective: Fix the beam

⁴ A Galilean telescope is defined as having one convex lens and one concave lens. The concave lens serves as the ocular lens, or the eyepiece, while the convex lens serves as the objective. While both “lenses” in the beam expander have the same concavity, their focal properties when combined mimic those of the optical Galilean telescope.

In the first set of experiments, it was clear that we had increased the beam divergence and degraded the transverse coherence in the vertical direction. Images of knife edges showed blurred horizontal edges (corresponding to large vertical divergence and poor transverse coherence in the diffraction plane) and sharp vertical edges. This was a serious problem as all synchrotron phase-based imaging techniques rely on the beam's extremely low divergence. Thus, the goal at this stage of the project was to fix the beam's transverse coherence in order to preserve its phase characteristics with regards to imaging. This was achieved by carefully matching the polychromatic and single-ray focal points, along with an increased expansion to 12 \times . The beam was used to capture phase-based images which confirmed that the transverse coherence problem had been eliminated. These results are presented in Chapter 5.

2.1.4 Third objective: Evaluate the beam

Knowing that the so-called “magic condition” was important for this phase preservation, a further goal was to measure how critical this condition really is. To this end, measurements were taken to evaluate the beam divergence at energies away from the magic condition for this particular crystal-reflection pair ((5,1,1) wafer with a (3,1,1)-type reflection). It was determined that the system was flexible to at least ± 5 keV. However, this was the physical limitation of the stage and, given the negligible difference in edge sharpness at all energies measured, it's presumed that the system is flexible over a much greater range. The true limitations are yet to be determined and require a rail system with greater range. These results are presented in Chapter 6.

While preserving the quality of transverse coherence of the beam, the expander system in the second set of experiments exhibited a region of missing intensity in the beam – a hole in the image. Thus the final goal for the dissertation was to explain this missing intensity and seek methods to eliminate such problems in future installations. A combination of finite element analysis (to confirm the problem was experimental not theoretical), diffraction measurements, and mechanical measurements were used to evaluate the system. It was determined that a defect in the second crystal's bending frame was responsible for distorting the crystal, thus causing a mismatch between the diffraction planes in that region of the beam. This highlights the importance of a very smooth finish on the bending frames and very careful handling to avoid even the slightest damage to the surface. These results are presented in Chapter 7.

2.1.5 Fourth objective: Upgrade the beamline

The remaining objective of the project is to permanently install the expander system in the ID beamline. This is largely an engineering problem and is outside the scope of this

dissertation. A grant proposal is in place to upgrade the BMIT facility, including modifications to the beamline vacuum chambers to enable installation of the first crystal in vacuum.

2.2 Summary of Manuscripts

2.2.1 Indirect measurement of average alveolar dimension using dynamic phase-contrast imaging (Chapter 3)

Relevance: This manuscript is included as an example of the type of experiment that could be carried out at the CLS with an appropriate beam expander and high-speed, large-field area detector.

Summary: Some lung diseases affect the growth of alveoli, the small air sacs inside the lungs, and a measure of alveolar size can aid clinicians in diagnosing and treating these diseases. However the micro-CT images that would be required to measure these air spaces is dose-prohibitive and therefore a safer technique would be useful. Particle image velocimetry (PIV) is an analysis technique that, when used for phase-based lung imaging, enables the tracking of small “spots” in the images frame to frame during a real-time video of a live animal, producing a vector map representing the lung motion. The pointwise divergence of this vector map has been shown to correlate closely with areas of lung damage {Fouras 2012}. The goal of this work was to correlate divergence to the alveolar size as measured by micro-CT in order to determine whether a phase-based imaging modality could aid clinicians in diagnosing lung disease. The conclusion was that alveolar size and divergence are extremely well correlated, and that given a suitable phase-based imaging system, PIV could be used to monitor alveolar growth with safe levels of x-ray exposure.

Contribution: I was the lead investigator in this experiment. I applied for and received beamtime at SPring-8 under the “Budding Researchers Support Proposal” program, designed the experimental procedure under the guidance of the Monash Lung Imaging Group and with their assistance (primarily with animal handling and providing the apparatus required for the experiment), carried out the collection of the data. I analyzed the data and wrote all sections of the paper.

2.2.2 Development of a bent Laue beam-expanding double-crystal monochromator for biomedical X-ray imaging (Chapter 4)

Relevance: This manuscript reports the first successful implementation of the bent Laue beam expanding system and provides a basic theoretical framework based on the geometric focus equations and the conditions under which the system will produce an expanded beam. A serious

problem (horizontal blurring) was identified with the understanding that further study was required to rectify this issue.

Summary: Proof-of-principle of the double bent Laue beam expander and preliminary results are reported. Imaging data captured using the expanded beam is presented, including full-field live animal real-time imaging and high-resolution micro-CT reconstructions. Results of different crystal types and reflections are presented along with the resulting expansion factors achieved. However a major problem with the system was known at this time, namely that the expander significantly blurred horizontal edges.

Contribution: Under the guidance of Dr. Dean Chapman and with the assistance of my colleagues, I performed the experiments reported in this work. This included: mounting and bending the crystals in the four bar bender, mounting the bending frames in the beamline, experimenting with different crystal types (*e.g.* (1,1,1), (5,1,1)) and reflections (*e.g.* (1,1,1), (2,2,0)), and collecting the data. I created the figures and wrote all sections of the paper and incorporated suggestions by other members of the group.

2.2.3 Phase-preserving beam expander for biomedical X-ray imaging (Chapter 5)

Relevance: This manuscript completes the core goal of the thesis project, namely to expand the beam without degrading the transverse coherence, and to explain the physics that allows this to happen. From this point, the remaining challenges are largely engineering problems, namely how to cylindrically bend a silicon crystal to a very small bend radius without distorting its shape.

Summary: The problem of horizontal blurring is fixed by carefully matching the geometric focus to the single-ray focus, thereby expanding the beam without degradation of the transverse coherence that enables phase-based imaging techniques. The derivation of an improved equation for the single-ray focus is presented, one that accounts for both upper- and lower-sign geometries as well as orientation of the crystal's concavity relative to the incident x-ray beam. A newly developed frame bender is also presented. This new frame bender both fixes the bending radius in order to minimise human effect, and allows water-cooling of the first crystal in order to draw out the heat load caused by the high-intensity ID beamline. Images of phase objects and knife edges are presented to demonstrate that the horizontal edge blurring has been eliminated. Plot profiles of the knife edges confirms that the horizontal and vertical edges have comparable sharpness. Finally, phase images of a biological sample are presented.

Contribution: I mounted the crystals and performed the experiments, collected and analyzed the data, and located the reference used by Dr. Ariel Gomez to develop the single-ray

focus equation, which I adapted to account for the orientation of the concavity relative to the incident beam and chose the sign convention thereof. I created the figures and wrote all sections of the paper.

2.2.4 Measuring the criticality of the “magic condition” for a beam expanding monochromator (Chapter 6)

Relevance: This manuscript demonstrates the flexibility of claims made earlier in the thesis, namely that for the purposes of biomedical imaging, the magic condition need not be strictly adhered to. This greatly extends the range of possibilities for the expander, as strict matching between foci and subsequent restriction to a single x-ray energy would present a serious limitation of the system.

Summary: In the previous paper, it was proposed that the geometric focus and single-ray focus must be carefully matched in what is referred to as the “magic condition.” However, exact matching of these foci would limit all imaging experiments to a single energy determined by the asymmetry angle. As it is desirable to have energy tunability for biomedical experiments, either to image specific types of tissue or to perform K-edge subtraction imaging, there was motivation to determine just how critical the magic condition really is. To that effect, an experiment was carried out to rock the crystals’ Bragg angles away from the magic condition for a fixed asymmetry angle, and measure the effect on the width, in pixels, of a knife edge and phase object. The results were that at all energies tested, the horizontal and vertical edges were virtually indistinguishable. It was concluded that perfect matching is not required, and that the real problem in the first experiment was that the single-ray focus and geometric focus had opposite signs, and this is what caused the blurring in the beam. At all energies, the phase fringe was more than adequate for phase-based imaging experiments.

Contribution: I designed and performed the experiments, analyzed the data, created the figures, and wrote all sections of the paper.

2.2.5 Characterisation of a bent Laue double crystal monochromator (Chapter 7)

Relevance: This paper seeks to tie up loose ends in determining the source of the non-uniformity and provides insight in how to mitigate these problems in the eventual installation to the ID beamline. The results of these experiments show that the problem is not with the theory developed in the previous chapter, but rather with a specific defect in the physical frame bender that is easily avoidable with careful machining and handling of the frames.

Summary: The expanded beam has a large area of missing intensity. This is caused by a mismatch between the crystals in that area and the resulting misalignment of the Darwin peaks. In order to understand why the crystals are misaligned in that region, they were evaluated using a variety of methods based on either physical measurements (*i.e.* a surface profile with a FaroArm tool) or diffraction methods (*i.e.* rocking curves in Bragg and Laue modes). Finite Element Analysis (FEA) was performed to confirm that this area of missing intensity is the result of imperfect bending and not inherent in the system. We found that there is an area in the second crystal that is physically distorted, and this is confirmed by matching its physical location to the area of missing intensity in the expanded beam.

Contribution: I designed and performed the diffraction experiments, collected and analyzed the diffraction data, analyzed the FaroArm data, created the figures, and wrote all sections of the paper.

Chapter 3 Indirect measurement of average alveolar dimension using dynamic phase-contrast imaging

Citation: M. Martinson, R.A. Lewis, A. Fouras, M. Siew, M. Wallace, S.B. Hooper, P. Babyn, Indirect measurement of average alveolar dimension using dynamic phase-contrast imaging, *World Congress on Medical Physics and Biomedical Engineering*, 51 (2015) 166-168.

Disclaimer: Reproduced with permission. Manuscript has been reformatted for consistency with the dissertation, including some rearrangement. References have been moved to the end of the dissertation as per CGSR requirements. Contact information has been removed. Figure 3.1 has been recreated from the source material to improve image quality. No content has been changed.

Indirect measurement of average alveolar dimension using dynamic phase-contrast imaging

M. Martinson¹, R.A. Lewis², A. Fouras³, M. Siew⁴, M. Wallace^{4,5}, S.B. Hooper^{4,5}, and P. Babyn⁶

¹ Physics and Engineering Physics, University of Saskatchewan, Saskatoon, SK

² Biomedical Engineering, University of Saskatchewan, Saskatoon, SK

³ Division of Biological Engineering, Monash University, Victoria, AUS

⁴ MIMR-PHI Institute of Medical Research, Victoria, AUS

⁵ Department of Obstetrics and Gynaecology, Monash University, Victoria, AUS

⁶ Department of Medical Imaging, University of Saskatchewan, Saskatoon, SK

Keywords: X-ray imaging, Image analysis, Micro-computed tomography, Particle Image Velocimetry, Lung disease.

Abstract: For some lung diseases, assessment of alveolar dimension could add critical information to inform patient care and disease progression. However, current clinical imaging techniques, such as computed tomography, lack the resolution required to measure these small structures in patients. While the gold standard imaging modality for measuring alveoli is micro-CT, this technique is not possible in clinical use due to the size of the patients and the radiation dose. An alternative imaging modality is phase-based contrast imaging, which would deliver a lower dose to patients and increase the size limit. Phase contrast X-ray imaging has previously been combined with particle image velocimetry (PIV) to measure lung motion, another indicator of lung disease. Thus it was hypothesised that average alveolar size could also be measured indirectly using PIV. In the work reported here, we show that average alveolar size shows a high correlation to the mathematical divergence of the velocity vector field that results from the

speckle pattern produced by phase imaging of mouse lungs. This correlation is linear with $p<0.006$. If this correlation holds in human lungs, it could potentially be calibrated to indirectly measure average alveolar size in human patients using some of the grating-based phase-contrast imaging methods that are showing great promise in clinical use.

3.1 Introduction

Gas exchange in the lung occurs in the most distal airway structures known as alveoli. The assessment of alveolar dimension is important for the understanding, diagnosis, treatment, and progression of some lung diseases. However, imaging modalities currently used in clinical settings lack the image resolution necessary to measure these tiny features. In animal models, the gold standard for measuring alveoli in live samples is micro-computed tomography (μ -CT). In humans, size constraints and the radiation dose delivered to patients makes this modality impossible for clinical use. Instead, an alternative method using phase-based contrast X-ray imaging (PCXI) is desirable.

PCXI of air-filled lungs produces a speckle pattern caused by X-ray refraction around the numerous, densely packed air sacs. As the lung inflates, points in the tissue move relative to one another, causing a displacement of the speckles over a small interval between temporally consecutive imaging frames. This produces a velocity vector field for that specific time interval. By capturing dynamic phase movies of a ventilated specimen, a series of velocity vector fields is produced. The technique of analyzing such velocity vector fields produced by small moving particles, such as the speckles produced by phase imaging of air-filled lungs, is termed Particle Image Velocimetry (PIV). These data can be analyzed by taking the spatial derivative of the vector field to find the divergence at various points in the lungs. Previous work {Fouras 2012} has established a correlation between divergence and lung compliance, which is an indicator of certain types of lung disease. In both humans and animal models, alveolarisation occurs by subdivision of larger saccules. In emphysema, the alveolar walls degrade also resulting in fewer but larger airspaces. In Bronchopulmonary dysplasia, failed alveolarisation results in fewer but larger distal airspaces. In healthy lungs, as alveoli are forming, the tissue between alveoli is also thinning, so despite new tissue outgrowth, there is an overall reduction in lung tissue relative to total lung volume in a healthy maturing lung. This suggests that the divergence in a volume of lung tissue might decrease as lungs mature. It was thus hypothesised that a correlation may exist between divergence (measured using phase-contrast imaging with PIV analysis) and alveolar dimension (measured using micro-computed tomography, μ -CT).

3.2 Methods

All procedures were approved by the SPring-8 Synchrotron Facility, the University of Saskatchewan, and Monash University Animal Ethics Committees. Balb/c mice were chosen as the animal model. In order to vary the degree of alveolarisation, and hence the average alveolar size, two age groups were chosen: 3 weeks (n=2) when alveoli are rapidly forming and 8 weeks (n=2) when mice are mature. The mice were anaesthetised (78mg/kg pentobarbitone sodium i.p.), surgically intubated, and placed in restraints for imaging using both PCXI and μ -CT. All imaging was conducted at the BL20B2 beamline of the SPring-8 synchrotron. The mice were mechanically ventilated using a custom-designed ventilator. During PCXI (frame rate of 20 Hz with exposure time of 15 ms), the mice were ventilated at a peak inspiratory pressure of 20 cmH₂O and end expiratory pressure of 3 cmH₂O. During the μ -CT (frame rate of 10 Hz with exposure time of 15 ms), the mice were ventilated at a breath hold of 3 cmH₂O. To eliminate motion artefacts, the mice were euthanised prior to μ -CT. The pixel size of the detector was approximately 13 μ m.

The two sets of data (PCXI vs μ -CT) were analyzed using completely different techniques.

The PCXI image sets were analyzed using a custom-built PIV analysis package {Fouras 2008}. As the lungs inflate and deflate, the speckle pattern created by phase imaging of air-filled lungs creates a velocity vector field between consecutive frames. These vector fields can be subdivided into regions, and the average mathematical divergence in each region can be measured. In order to correlate PCXI to μ -CT, the divergences were averaged over the entire lung region and through one full inhalation, reducing the set of projection phase images for each specimen down to a single number that represents the average divergence for one full inhalation.

The μ -CT image sets were reconstructed and analyzed using NRecon and CTAn (Bruker microCT). Because CTAn is typically used for measuring porosity of bone, the reconstructed images were rescaled so that the lung tissue had a grey level of 400 HU and the air had a grey level of -1000 HU. A region of interest (ROI) was selected to encompass the entire lung region. Using CTAn's built-in analysis tools, this ROI was then processed to measure the total pore volume and the total number of pores, corresponding to the total air volume inside the lungs and the number of detected alveoli, respectively. These values were then divided to calculate the average alveolar volume.

3.3 Results

The data (Table 3.1) from each modality were plotted (Figure 1) and found to have a linear relationship with a very strong correlation ($r^2 \geq 0.988$ & $p \leq 0.006$, calculated using Microsoft Excel's regression analysis tools) between average alveolar volume and average divergence.

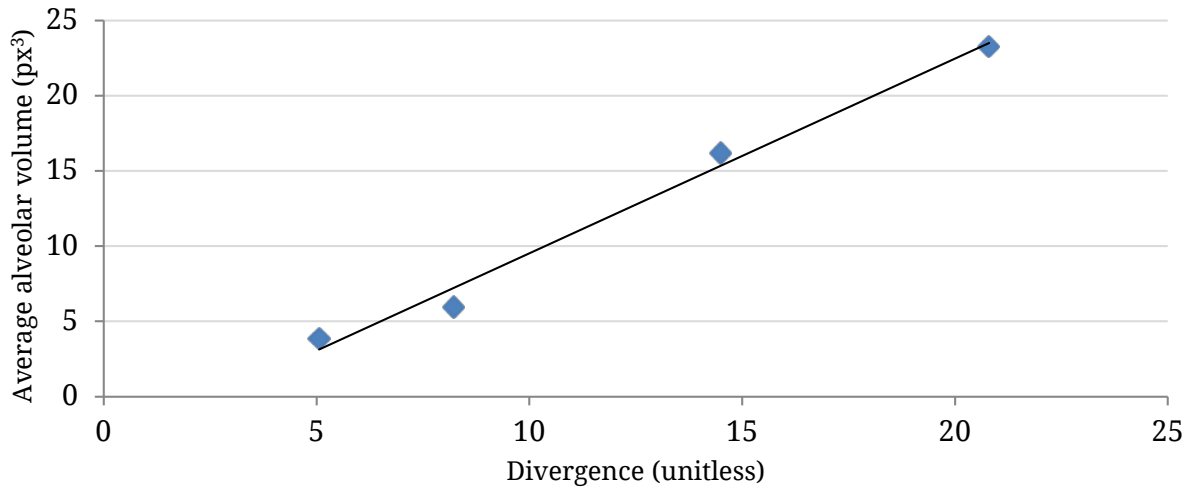


Figure 3.1 Average alveolar volume as a function of lung divergence.

Table 3.1 PCXI and μ -CT results

Mouse identifier	Age	Average Divergence	Average Alveolar Dimension (px ³)
M1	3 weeks	20.8	23.25
M2	3 weeks	14.5	16.19
M3	8 weeks	8.22	5.95
M4	8 weeks	5.06	3.83

3.4 Discussion

While the data appears to indicate that the younger mice have larger alveoli, this likely represents a normalisation to total lung volume inherent in the measurement technique. To measure the alveolar size without such normalisation, a higher resolution surface reconstruction would be required. Due to the large pixel size (~13 μm) compared to the average size of mouse alveoli (~45 μm) {Soutiere 2004}, this was not possible for the dataset acquired.

This work is a preliminary study to determine whether any correlation exists between alveolar size and lung divergence. The results clearly indicate that there is, despite the shortcomings of the alveolar measurement technique. These are easily overcome with higher resolution scanning and will be incorporated in a more in-depth study, which will also increase both the number and diversity of samples, incorporating mouse breeds with differing sizes of alveoli.

3.5 Conclusion

Clinical computed tomography lacks the spatial resolution necessary to measure small structures such as the alveoli of human patients. While micro-computed tomography is more than capable of resolving these small structures, the technique is both dose- and size-prohibitive for use in human patients. Phase contrast X-ray imaging presents a possible alternative for measuring the average alveolar dimension. Two groups of mice at different ages (3 weeks and 8 weeks) were imaged using both micro-CT and phase-based contrast imaging. The micro-CT reconstructions were used to measure average alveolar size, and the phase images were analyzed to determine the divergence of the lungs' velocity vector fields using particle image velocimetry. It was found that a strong correlation exists between average alveolar size and the mathematical divergence of the velocity vector field produced by the speckle pattern created by imaging air-filled lungs using phase-based X-ray imaging. This suggests the potential of using phase-based imaging in a clinical setting to diagnose lung disease in patients, possibly with some of the grating-based interferometry techniques that have begun to be tested in clinical use.

Acknowledgements: The synchrotron radiation experiments were performed at BL20B2 of SPring-8 with the approval of the Japan Synchrotron Radiation Research Institute (JASRI) (Proposal No. 2013A1591). MM is a Fellow, and RAL and PB are Mentors, in the Canadian Institutes of Health Research Training grant in Health Research Using Synchrotron Techniques (CIHR-THRUST). SBH and MS were supported by the Victorian Government's Operational Infrastructure Support Program.

Conflict of Interest: The authors declare that they have no conflict of interest.

Chapter 4 Development of a Bent Laue Beam Expanding Double Crystal Monochromator for Biomedical X-ray Imaging

Citation: M. Martinson, N. Samadi, G. Belev, B. Bassey, R. Lewis, G. Aulakh, D. Chapman, Development of a bent Laue beam-expanding double-crystal monochromator for biomedical X-ray imaging, *Journal of Synchrotron Radiation*, 21 (2014) 479-483.

Copyright IUCr, reproduced with permission (<http://dx.doi.org/10.1107/S1600577514003014>).

Disclaimer: Manuscript has been reformatted for consistency with the dissertation, including some rearrangement. References have been moved to the end of the dissertation as per CGSR requirements. Contact information has been removed. No content has been changed.

Development of a Bent Laue Beam Expanding Double Crystal Monochromator for Biomedical X-ray Imaging

M. Martinson¹, N. Samadi², G. Belev³, B. Bassey¹, R. Lewis², G. Aulakh⁴, and D. Chapman^{1,4}

¹ Physics and Engineering Physics, University of Saskatchewan, Saskatoon, SK

² Biomedical Engineering, University of Saskatchewan, Saskatoon, SK

³ Biomedical Imaging and Therapy Beamlines, Canadian Light Source, Saskatoon, SK

⁴ Anatomy & Cell Biology, University of Saskatchewan, Saskatoon, SK

Keywords: beam expander, bent Laue diffraction, double crystal monochromator, biomedical imaging, dynamic imaging

Synopsis: A bent Laue beam expanding double crystal monochromator was developed and tested at the Biomedical Imaging and Therapy beamline at the Canadian Light Source. The expander will reduce scanning time for micro-CT and allow dynamic imaging that has not previously been possible at this beamline.

Abstract: The Biomedical Imaging and Therapy (BMIT) beamline at the Canadian Light Source has produced some excellent biological imaging data. However the disadvantage of a small vertical beam limits its usability in some applications. Micro-CT imaging requires multiple scans to produce a full projection, and certain dynamic imaging experiments are not possible. A larger vertical beam is desirable. It was cost-prohibitive to build a longer beamline that would have produced a large vertical beam. Instead, it was proposed to develop a beam expander that would create a beam appearing to originate at a source much farther away. This was accomplished using a bent Laue double crystal monochromator in a non-dispersive divergent geometry. The design and implementation of this beam expander is presented along with results

from the micro-CT and dynamic imaging tests conducted with this beam. Flux (photons / unit area / unit time) has been measured and found to be comparable to the existing flat Bragg DCM in use at BMIT. This increase in overall photon count is due to the enhanced bandwidth of the bent Laue configuration. Whilst the expanded beam quality is suitable for dynamic imaging and micro-CT, further work is required to improve its phase and coherence properties.

4.1 Introduction

Biomedical X-ray imaging using synchrotron light sources has been well established {Suortti 2003, Lewis 2004, Thomlinson 2005, Liu 2013, Bravin 2013} . Biomedical beamlines are in use around the world for a variety of imaging techniques including in-line phase contrast and micro-CT. At the Canadian Light Source (CLS) in Saskatoon, two biomedical beamlines have been commissioned. BMIT-BM uses a bend magnet and BMIT-ID uses a wiggler insertion device. While both of these beamlines offer high flux, they suffer the drawback of small beam heights. BMIT-BM produces a maximum beam height of approximately 6 mm at the 23 m source-to-sample distance, and BMIT-ID produces a maximum beam height of 11 mm at the 55 m source-to-sample distance. As a result, most samples must be scanned vertically through the beam to image the entire region of interest.

Vertical scanning poses severe limitations in two major areas. CT scans must be made in small vertical sections, imaging roughly 5 mm⁵ per rotation. Consecutive sections require enough overlap to reliably stitch the projections together, so regions of the subject are imaged repeatedly. Not only is this time consuming, but it increases the delivered dose, which is problematic for live animal studies. In addition to the longer scan times, these vertical sections must then be stitched together during processing, which increases both processing time and likelihood of error.

The second, and even more important, limitation is with dynamic imaging {Lewis 2005}. Many important physiological processes can only be understood by capturing movies of live systems. Examples include coronary angiography and functional lung imaging {Hyodo 1998, Hooper 2009, Porra 2011, Schültke 2011, Astolfo 2013} . Scanning subjects through the beam makes it impossible to capture the entire process in one shot which represents a major limitation of the beamline for cutting edge studies into physiological processes.

4.2 Design & Implementation

A bent Laue double crystal monochromator (BL-DCM) was chosen to implement the expander as it allows full tunability of the energy from 20 – 100 keV. When a crystal wafer is

⁵ [in height]

cylindrically bent with the concave side facing the source, the diffracted beam will diverge with a virtual focus on the incident side of the crystal. Two such crystals placed in a non-dispersive divergent geometry {Suortti 1995} produce a beam with a vertical height proportional to the distance between the second crystal and the virtual focal point of the first crystal. The bending radius of the second crystal must be such that its focal point is the same as that of the first crystal in order to allow maximum reflection from the planes in the second crystal. The crystals are deemed to “match” when their centres are parallel (same Bragg angle) and their focal points are at the same location.

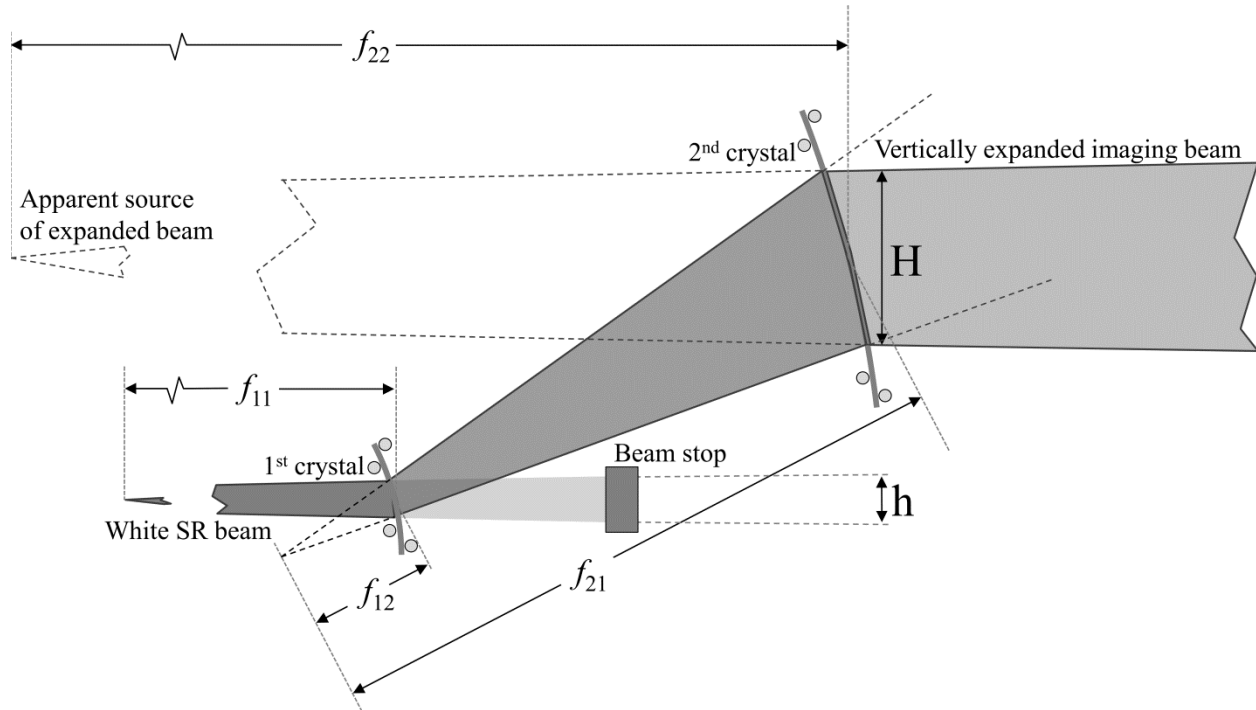


Figure 4.1 Schematic of crystal geometry and orientation, ray tracing diagrams, and focal lengths.

Unlike optical lenses, the focal point of a crystal is a function not only of the bending radius, but also the asymmetry and Bragg angles (χ and θ_B , respectively). In the setup used for these experiments, the first crystal was in an “up bounce” / positive sign geometry and the second crystal was in a “down bounce” / negative sign geometry {Erola 1990}. The relationships between focal points, f_{ij} , and bending radii, ρ_i , are given below. The indices denote the first ($i = 1$) or second ($i = 2$) crystal, and the incident ($j = 1$) or diffracted ($j = 2$) beam.

$$\frac{\cos(\chi - \theta_B)}{f_{11}} - \frac{\cos(\chi + \theta_B)}{f_{12}} = \frac{2}{\rho_1} \quad 4.1$$

$$\frac{\cos(\chi + \theta_B)}{f_{21}} - \frac{\cos(\chi - \theta_B)}{f_{22}} = \frac{2}{\rho_2} \quad 4.2$$

The expansion factor H/h is determined by the ratio of bending radii and the crystal-crystal spacing. Suppose that an expansion of m times is desired. If the distance f_{11} from the source to the first crystal is known and the bending radii are set such that $\rho_2 = m\rho_1$ and the crystal-crystal spacing is set such that $f_{21} = -mf_{12}$, then it follows from Equations 4.1 & 4.2 that $f_{22} = mf_{11}$. Since this double-crystal geometry preserves the divergence of the beam and beam height is proportional to vertical divergence and distance from the source, it follows that if the spacing between the crystals is much smaller than the distance to the source, then m is equal to the expansion factor.

Whilst a smaller bending radius produces a larger expansion over a shorter distance, elasticity limitations of crystal wafers place lower bounds on their bending radii. Based on a rule of thumb that the minimum “safe” bending radius is equal to $1000\times$ the thickness of the crystal, it was decided that the ~ 0.5 mm thick crystals could be bent no more than $\rho = 50$ cm. For the preliminary attempt, the following parameters were chosen: bending radius of first crystal: $\rho_1 = 1$ m ($f_{12} \cong -0.5$ m), bending radius of second crystal: $\rho_2 = 3$ m ($f_{21} \cong 1.5$ m), distance between crystals: $\Delta f = 1$ m.

The cylindrical bend was set optically and implemented using a four-bar bender (Figure 4.1). This system is flexible, as virtually any bending radius can be achieved. Once the bend radius was set, the bending frames were placed on crossed goniometer stages to manipulate the Bragg angles and tilts if necessary. The appropriate reflections were found by comparing the reflection pattern produced on a fluorescent screen to stereographic projection maps. The first crystal was set to the appropriate Bragg angle for the chosen reflection and energy. The second crystal was then placed in the diffracted beam at the distance calculated from the chosen bending radii and Bragg angle. After opening the beamline slits to full size, the second crystal was aligned with the first crystal to optimise the intensity and uniformity of the beam. If necessary, the distance between crystals was adjusted in order to improve beam uniformity. For measuring beam expansion, the beamline slits were used to aperture the beam in the region with the best quality. For imaging, the beamline slits were left at full size.

A preliminary experiment was performed using (1,1,1) silicon crystal wafers with a (1,1,1)-type reflection such that $\chi = 19.47^\circ$. This reflection was selected due to its broad Darwin width and resulting high intensity. The Bragg angle was determined using the K-edge absorption of iodine as an energy calibration standard. The beam size and shape were imaged on burn paper at

three locations: the incident white beam coming into the hutch, the beam diffracted by the second crystal (termed the “diffracted beam”), and the beam transmitted through the second crystal (the “transmitted beam”). Expansion was calculated as the ratio between the diffracted beam and the incident beam.

Intermediate attempts of 3 \times , 5 \times , and 7 \times expansion were made with Si (5,1,1) crystal wafers with a (2,2,0)-type reflections such that $\chi = 15.79^\circ$. Simple imaging tests were conducted to evaluate absorption, phase, and edge features. Because the beam intensity had been more uniform during the preliminary experiment, the (1,1,1) wafers were put back in place for the high-resolution micro-CT and dynamic imaging tests.

The flux was measured using a (1,1,1)-type reflection at an energy of 20.0 keV, as confirmed by the absorption K-edge using a molybdenum filter. An ion chamber was placed in the expanded beam with lead shields preventing the beam from hitting the electrodes. An image of the beam through the ion chamber was captured using a 200 μm pixel size flat panel detector (Hamamatsu C9252DK-14), allowing the exposure area to be measured precisely.

4.3 Results

Using a (1,1,1) silicon crystal wafer with (1,1,1)-type reflections placed in matching bent Laue non-dispersive divergent geometry, the beam was expanded vertically to a maximum height 7 \times larger than the incident beam. The Si (5,1,1) wafers with (0,2,2)-type reflections reached a maximum expansion of 7.7 \times . The target of 10 \times has not yet been reached and will likely require a new bending and alignment apparatus to achieve.

The beam quality was evaluated using both absorption and phase based imaging modalities, as well as visual inspection of the beam itself. Most problematic were the non-uniform intensities in some beams (Figure 4.2.a). At its worst, this non-uniformity made imaging impractical. Fortunately, in most cases, the non-uniformity occurred mostly around the edges and still allowed a suitably large region for imaging. Absorption imaging tests were conducted for both projection and CT imaging. Flat-dark corrected images were devoid of artefacts, despite a visible line of lower intensity due to another competing reflection diffracting away intensity – a glitch in the beam (Figure 4.2.b). In an effort to locate a region of the diffracted beam devoid of glitches, the Bragg angle was adjusted through a small range ($\sim 2^\circ$). While this did not remove the glitches as desired, a pleasing result was the production of an extremely large and uniform beam, covering a region approximately 40 mm vertical \times 94 mm horizontal diffracted from a white beam with an incident height of 6.5 mm (Figure 4.2.c).

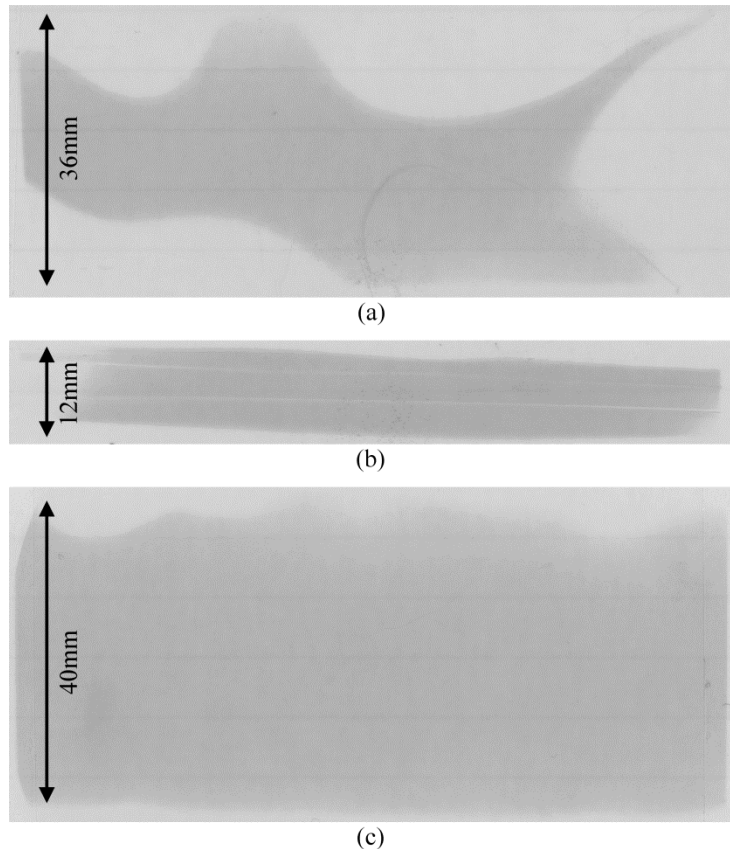


Figure 4.2 Burn paper images showing beam quality. (a) Extreme example of non-uniform intensity. (b) Beam “glitches.” (c) Large (~40 mm) beam with uniform intensity.

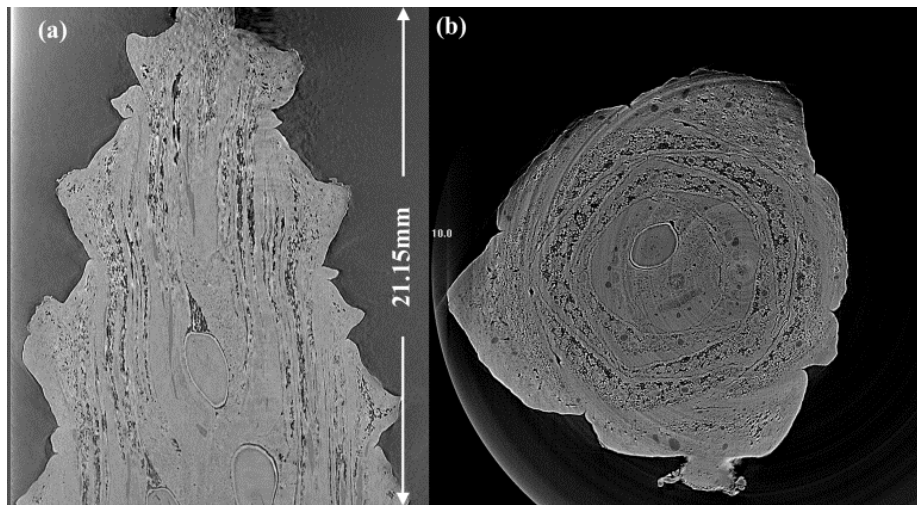


Figure 4.3 Micro-CT image of a pine cone. Image was captured in a single rotation. View A is an axial slice, view B is a sagittal slice. The vertical field of view of 21.15 mm would require 7 rotations to capture without beam expansion.

The micro-CT imaging tests used a beam measuring 28 mm vertical \times 62 mm horizontal. This beam was capable of completely filling the high resolution ($8.75 \mu\text{m}$) Hamamatsu detector (AA-60 beam monitor coupled to C9300-124 CCD camera resulting in FOV 31.08 mm H \times 23.31 mm

V) regularly used for micro-CT. This expansion would allow objects up to about 21 mm in height (Figure 4.3) to be imaged in a single rotation, rather than the vertical scanning method traditionally used at BMIT. This improvement would reduce scan times by as much as 85%.

The 40 mm beam was used to capture live animal dynamic images using the flat panel detector running at 30 frames per second. This setup allowed an entire adult mouse to be imaged laterally in a single shot (Figure 4.4). Positioning the mouse vertically, this beam would be more than large enough to capture the entire lung region, allowing for dynamic lung imaging similar to the work reported in {Lewis 2005}. All animal work was done in accordance with the Guidelines of the Canadian Council on Animal Care under the authority of the University [of Saskatchewan] Committee on Animal Care and Supply.

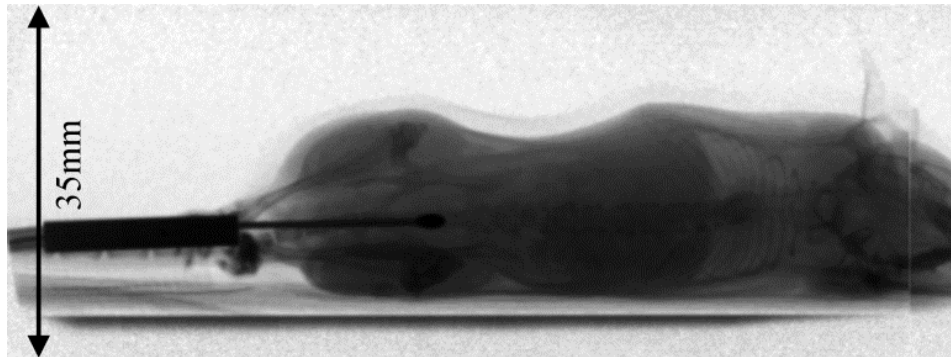


Figure 4.4 Flat-dark corrected frame from a movie of a live mouse captured with 200 μm flat panel detector (Hamamatsu C9252DK-14) at 30 fps. Movie sample available in additional data online. Vertical line on the right is an artefact of the detector, not the beam.

Table 4.1 Summary of expansion results and energy parameters

Attempt	Incident Height (mm)	Diffracted height (mm)	Expansion factor	Silicon Wafer	Reflection type	Bragg angle	Energy (keV)
Proof-of-principle	2.5	9.0	3.6	(1,1,1)	(1,1,1)	3.42°	33.16
Target of 3×	2.1	4.2	2.0	(5,1,1)	(2,2,0)	6.56°	28.3
Target of 5×	2.9	15.0	5.2	(5,1,1)	(2,2,0)	6.56°	28.3
Target of 7×	3.0	23.0	7.7	(5,1,1)	(2,2,0)	6.56°	28.3
μCT imaging	4.0	28.0	7.0	(1,1,1)	(1,1,1)	6.56°	17.3
Dynamic imaging	6.5	40	6.2	(1,1,1)	(1,1,1)	6.31°	18.0
Flux	0.54	3.8	7.0	(1,1,1)	(1,1,1)	5.67°	20.0

Flux was measured at 20.0 keV. The ion chamber measured a current of 316 pA at a ring current of 209.7 mA. The exposed area was 3.8 mm vertical \times 17.4 mm horizontal and the ion chamber path length was 15.1 cm. To protect the flat panel detector, 6.66 mm of aluminium was used as a filter. Using the attenuation coefficients provided by NIST {Hubbell 2004}, the actual flux was calculated to be 2.5×10^4 ph/s \cdot mm 2 \cdot mA, which would increase to 1.2×10^7 ph/s \cdot mm 2 \cdot mA without the filter. This would produce a surface dose of 4 μ Gy/s \cdot mA with the filter and 2 mGy/s \cdot mA without. Using this technique and the beamline's Bragg double crystal monochromator at 20 keV, the flux was measured to be 1.2×10^4 ph/s \cdot mm 2 \cdot mA, which would increase to 5.7×10^6 ph/s \cdot mm 2 \cdot mA without the filter.

4.4 Discussion

During all attempts at beam expansion, it was not found possible to create a perfectly uniform beam such as that produced by the beamline's flat Bragg DCM. The diminished expansion ($2.0\times$) during the 3 \times attempt may be explained by this non-uniformity as the image taken of the diffracted beam may have overlapped a region of low intensity. While the (1,1,1) wafers did appear to be free of glitches, the beam they produced lacked the uniformity required for high quality imaging. It is suspected that the four bar bending system produces imperfect cylindrical bending due to elasticity in the bending bars and wafers, variations in crystal thickness, anticlastic bending of the crystals, and non-parallel bending bars. This creates distortion in the crystals that prevents them from matching perfectly throughout the entire beam region, regardless of relative angle or distance. In future work the aim is to design a rigid bender with fixed bending radii so that the crystal will be forced into place.

The rigid frame bender will also provide an excellent heat sink for cooling the crystal with a liquid-metal (*i.e.* In/Ga) interface between the frame and the silicon. For these experiments, the maximum heat-load on the first crystal was calculated to be less than 25 W. During regular imaging, the filters used to protect the detector reduced the heat-load to under 200 mW.

A knife-edge placed horizontally in the expanded beam revealed significant vertical blurring which increased with the distance between the edge and detector (Figure 4.5). The blurring was not present in the horizontal direction, as a knife-edge placed vertically produced a sharp image at all distances. These results indicate that the X-rays exiting the second crystal are parallel horizontally but not vertically. The vertical beam divergence can be explained by diffraction occurring in-depth within both crystals producing a polychromatic focus and allowing rays to exit the same point in the second crystal but at different angles. This "Borrmann fan" effect is known to occur in the Laue crystal during the process of dynamical diffraction. This effect increases the beam size and apparent source size in the diffraction plan and reduces the

coherence of the beam. Such a “divergence effect,” if not controlled, will destroy the possibility of phase contrast in the vertical direction.

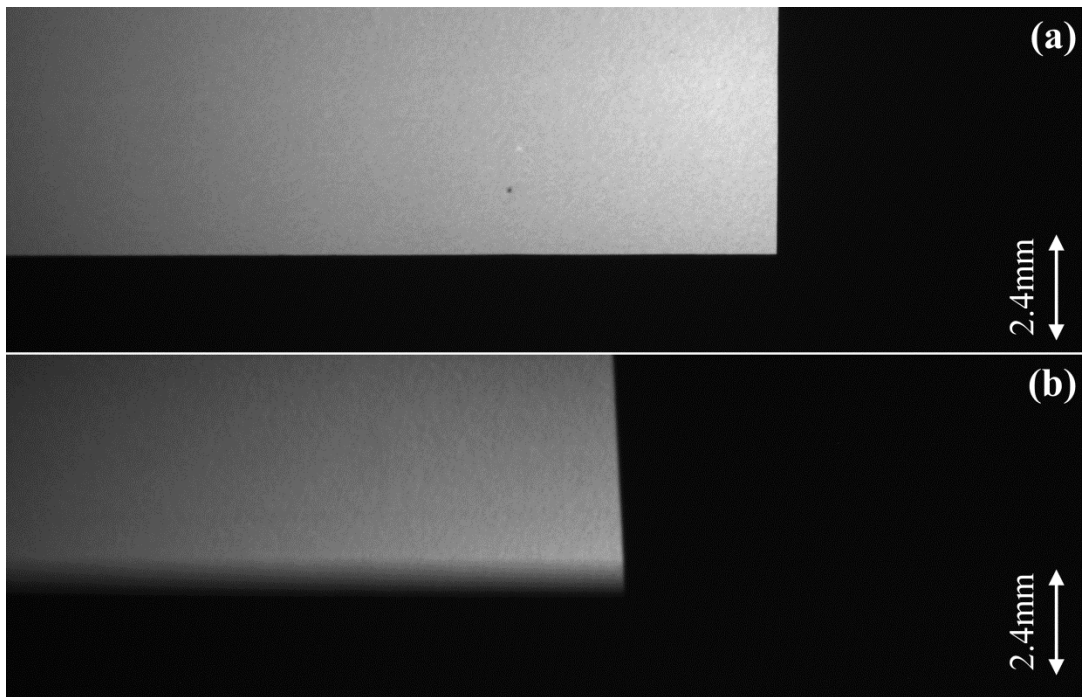


Figure 4.5 Vertical and horizontal knife edge placed at (A) 140 mm and (B) 5135 mm sample-detector distance.

4.5 Conclusion

A proof-of-principle study was made to determine whether a bent Laue beam expander could be developed for biomedical imaging applications. Beam expansion was successfully performed under a variety of conditions with expansions ranging from $2\times$ to $7.7\times$. The measured flux per unit area was comparable to that available with the flat Bragg double crystal monochromator currently used in the beamline. The increase in total photon count while expanding the beam size is made possible by the enhanced bandwidth of the bent Laue double crystal monochromator. Some initial experiments were performed to demonstrate the viability and usefulness of the method. Problems that were identified include beam divergence after the second crystal as well as non-uniformity of the beam. The latter problem will be addressed by better control over the crystal and bending process but the beam divergence effect will require further study of ways to minimise or eliminate this phenomenon.

Acknowledgements: The authors wish to acknowledge Melanie van der Loop for overseeing the live animal imaging test. Mercedes Martinson, Nazanin Samadi, Bassey Bassey,

and Gurpreet Aulakh are Fellows, and Dean Chapman and Rob Lewis are Mentors, in the Canadian Institutes of Health Research Training grant in Health Research Using Synchrotron Techniques (CIHR-THRUST). This work is supported in part by a Discovery Grant from the Natural Sciences and Engineering Research Council of Canada (NSERC) and Canada Research Chair. Research described in this paper was performed at the Canadian Light Source, which is funded by the Canada Foundation for Innovation, NSERC, the National Research Council Canada, the CIHR, the Government of Saskatchewan, Western Economic Diversification Canada, and the University of Saskatchewan.

Chapter 5 Phase Preserving Beam Expander for Biomedical X-ray Imaging

Citation: M. Martinson, N. Samadi, B. Bassey, A. Gomez, D. Chapman, Phase-preserving beam expander for biomedical X-ray imaging, *Journal of Synchrotron Radiation*, 22 (2015) 801-806.

Copyright IUCr, reproduced with permission (<http://dx.doi.org/10.1107/S1600577515004695>).

Disclaimer: Manuscript has been reformatted for consistency with the dissertation, including some rearrangement. References have been moved to the end of the dissertation as per CGSR requirements. Contact information has been removed. Some figures have been recreated from the source material to improve image quality. No content has been changed.

Phase Preserving Beam Expander for Biomedical X-ray Imaging

M. Martinson¹, N. Samadi², B. Bassey¹, A. Gomez³, and D. Chapman^{1,4}

¹ Physics and Engineering Physics, University of Saskatchewan, Saskatoon, SK

² Biomedical Engineering, University of Saskatchewan, Saskatoon, SK

³ Brockhouse Beamlines, Canadian Light Source, Saskatoon, SK

⁴ Anatomy & Cell Biology, University of Saskatchewan, Saskatoon, SK

Keywords: beam expander, bent Laue diffraction, double crystal monochromator, biomedical imaging, dynamic imaging, in-line phase imaging, polychromatic focus

Synopsis: Building on previous work, a phase preserving bent Laue beam expanding monochromator was developed with the capability of performing live animal phase contrast dynamic imaging at the Biomedical Imaging and Therapy beamline at the Canadian Light Source.

Abstract: The BioMedical Imaging and Therapy beamlines at the Canadian Light Source are used by many researchers to capture phase-based imaging data. These experiments have so far been limited by a small vertical beam size, requiring vertical scanning of biological samples in order to image their full vertical extent. Previous work has been done to develop a Bent Laue Beam Expanding Monochromator for use at these beamlines, however the first attempts exhibited significant distortion in the diffraction plane, increasing the beam divergence and eliminating the monochromator's usefulness for phase-related imaging techniques. Recent work has been done to more carefully match the polychromatic and geometric focal lengths in a so-called "magic condition" that preserves the divergence of the beam and enables full-field phase-based imaging techniques. The new experimental parameters, namely asymmetry and Bragg angles, were evaluated by analysing knife-edge and in-line phase images to determine the effect on beam divergence in both vertical and horizontal directions, using the beamline's flat Bragg double-

crystal monochromator as a baseline. The results show that by using the magic condition, the difference between the two monochromator types is less than 10% in the diffraction plane. Phase fringes visible in test images of a biological sample demonstrate that this difference is small enough to enable in-line phase imaging, despite operating at a sub-optimal energy for the wafer and asymmetry angle that was used.

5.1 Introduction

At the Canadian Light Source (CLS) in Canada, the BioMedical Imaging and Therapy (BMIT) bend magnet (BMIT-BM) beamlines and insertion device (BMIT-ID) {Wysokinski 2007, Wysokinski 2013} have been very successful in their mission to image biological tissue and conduct live animal imaging studies {Pratt 2014}. However, since their inception, they've been limited by the vertical beam size. This poses limitations for imaging modalities such as micro-computed tomography and dynamic phase imaging, techniques which are necessary to remain at the cutting edge of biomedical imaging research.

Previous results {Martinson 2014} reported a vertical beam expansion of approximately 7.7 \times . During these experiments, we discovered that the beam expander destroyed the beam's phase characteristics in the vertical direction (corresponding to horizontal edges in the object) and caused blurring of horizontal (but not vertical) knife edges placed at longer sample-to-detector distances. We have taken a two-pronged approach to solving this problem. On the theoretical side, we derived a better approximation for the polychromatic focal length, allowing us to carefully merge it with the well-established geometric focus equation. At the same time, we developed a bending frame that allowed us to more carefully control the bend radius of the crystal. The result of this effort is a great improvement in the coherence of the expanded beam, enabling techniques such as dynamic phase imaging at the BMIT beamlines.

5.2 Background Theory

In order to observe edge-enhancement refraction effects, the source must be angularly small (either physically small and/or far away), which imparts a high degree of transverse coherence to the wavefronts, hereto referred as phase coherence or simply coherence. Apparent angular source size is adversely affected when the two types of Bent Laue crystals focus – single-ray (polychromatic) and geometric (monochromatic) – are mismatched. In order to preserve the beam coherence, these two focal points must coincide {Suortti 1993} in what is hereto referred as the “magic condition” (Figure 5.1). The magic condition restores the source to its proper angular size, thus preserving the edge-enhancement effects hereto referred as the phase properties of the images.

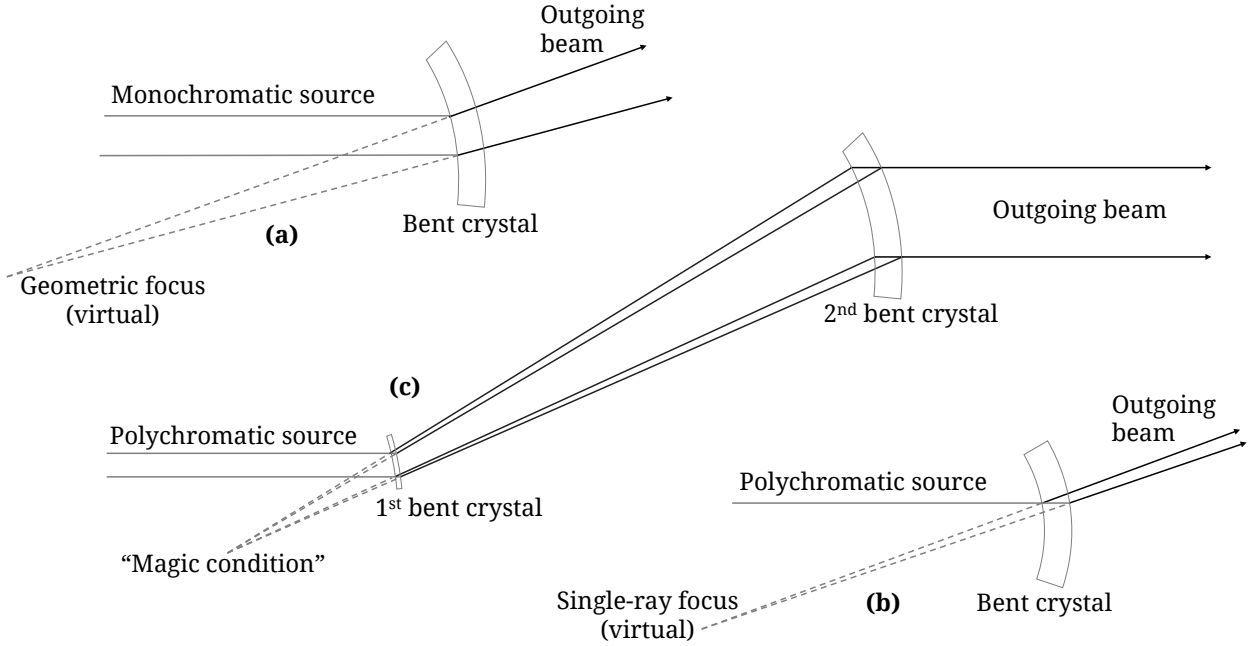


Figure 5.1 Subfigure (a) depicts the geometric (virtual) focus of two incoming monochromatic rays by a bent Laue crystal. Subfigure (b) depicts the single-ray (virtual) focus of a polychromatic beam by a bent Laue crystal. Subfigure (c) depicts the two crystals aligned such that the single-ray and geometric foci of the first crystal coincide with each other and with the geometric focus of the second crystal. The first crystal satisfies the “magic condition.”

Given a crystal with a specified asymmetry angle, the Bragg angle can be chosen so that the two focal points coincide. However, this determines the energy used for the experiment, so an alternative method is to first choose a convenient energy and reflection (preferably with high reflectivity to maximise flux), and then choose the corresponding asymmetry angle accordingly. Unfortunately, obtaining custom cut crystals with uncommon asymmetry angles is often cost-prohibitive. A compromise is to use readily available off-cut crystals with asymmetry angles close to ideal, and then to allow some variance in the Bragg angle.

Both geometric and single-ray focal lengths are a function of the Bragg angle θ_B , the asymmetry angle χ , and the crystal bending radius R . The geometric focus f_g is also a function of the source-to-crystal distance f_s and is given implicitly by {Schulze 1998}:

$$\frac{\cos(\chi \mp \theta_B)}{f_g} - \frac{\cos(\chi \pm \theta_B)}{f_s} = \frac{2}{R} \quad 5.1$$

The usual sign convention is used, where the focus is real (virtual) if $f_g > 0$ ($f_g < 0$). Assuming the source is far away ($f_s \gg R$), then f_g and R have the same sign. This motivates a sign convention for the bend radius such that $R > 0$ ($R < 0$) when the source is on the convex (concave)

side of the crystal. The upper/lower-sign convention refers to the angle ($\chi \pm \theta_B$) between the incoming beam and the surface normal, as shown in Figure 5.2.

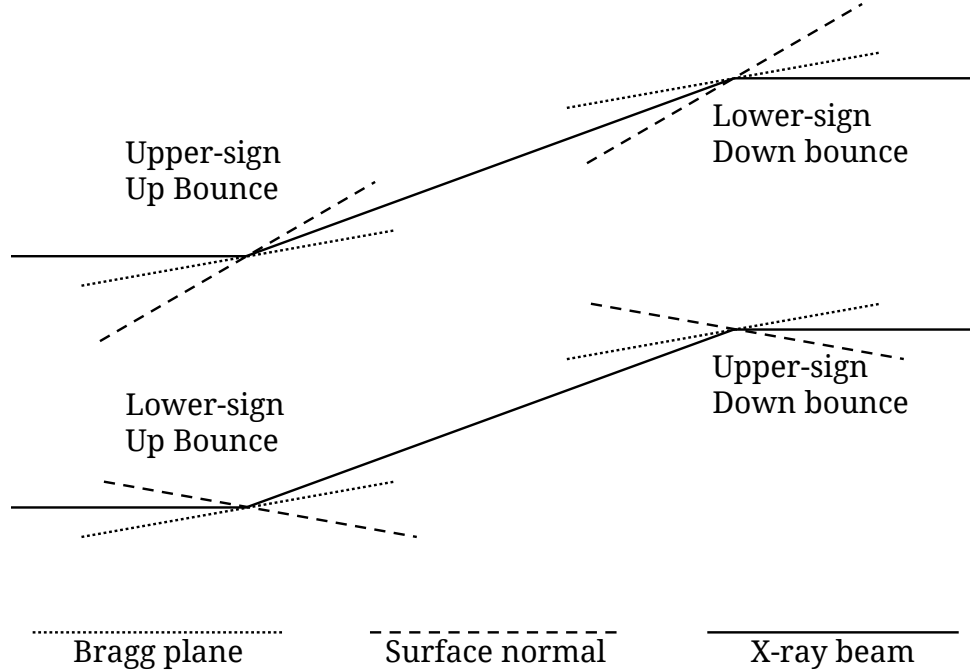


Figure 5.2 Upper-sign and Lower-sign geometries.

At a first approximation, the polychromatic focus has been previously given {Suortti 1993} as:

$$f = R \frac{\sin 2\theta_B}{2 \sin(\chi \pm \theta_B)} \quad 5.2$$

However, this does not account for the curvature of the diffraction planes induced by the elastic deformity of the crystal. For a better approximation, consider a crystal with Poisson ratio ν and thickness T . We examine the pencil beam's path through the crystal to determine the angle between a ray diffracted at the incident surface and a ray diffracted at the exit surface (Figure 3). As an incident ray traverses the crystal, it sees a change in Bragg angle {Erola 1990} of $\Delta\theta_{rot}$:

$$\Delta\theta_{rot} = \left(\frac{T}{R}\right) [\tan(\chi \pm \theta_B) + \sin \chi \cos \chi (1 + \nu) \mp \tan \theta (\cos^2 \chi - \nu \sin^2 \chi)] \quad 5.3$$

This form of the equation is useful for measuring the bandwidth of a diffracted pencil beam, however it requires modification for use in the derivation of the polychromatic focal equation. First, it provides only the magnitude of the change in Bragg angle, not the sign. This is important because a pencil beam will create either a virtual or real focus depending on the upper- or lower-sign geometry as well as the orientation of the crystal concavity relative to the source. In

keeping with our earlier sign convention for the bend radius, we modify the equation by multiplying by (-1) when we are in lower-sign geometry. The second modification stems from the third term in the equation, $\tan \theta (\cos^2 \chi - v \sin^2 \chi)$, which accounts for the change in d-spacing as the beam passes through the crystal. While this affects the energy bandwidth of the exiting beam, it does not change the focus properties, and so is dropped from our modified equation. The final form is then:

$$\Delta\theta'_{rot} = \pm \left(\frac{T}{R} \right) [\tan(\chi \pm \theta_B) + \sin \chi \cos \chi (1 + v)] \quad 5.4$$

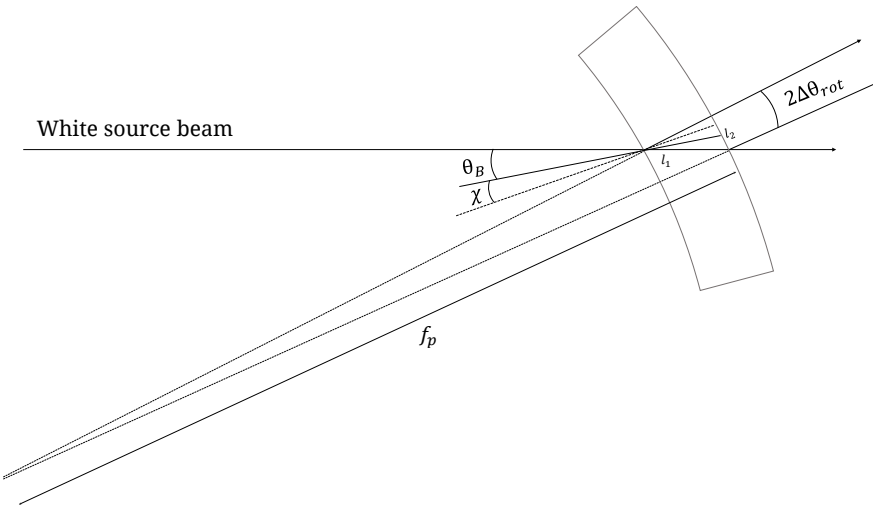


Figure 5.3 Polychromatic focus diagram.

The path length of the non-diffracted ray through the crystal is

$$l_1 = T / \cos(\chi \pm \theta_B) \quad 5.5$$

At the exit surface, the diffracted rays compose a beam with width

$$l_2 = l_1 \sin 2\theta_B = T \sin 2\theta_B / \cos(\chi \pm \theta_B) \quad 5.6$$

Using the small angle approximation,

$$l_2/f_p = 2\Delta\theta'_{rot} \quad 5.7$$

and solving for the polychromatic focus, we have:

$$f_p = \pm \frac{R \sin 2\theta_B}{2 \sin(\chi \pm \theta_B) + (1 + v) \sin 2\chi \cos(\chi \pm \theta_B)} \quad 5.8$$

This agrees with a previous result {Sutter 2008} that was derived for a bent Laue crystal in the lower-sign orientation. Their derivation appears to use the convention that $R > 0$, and instead brings the negative sign into the equation for the case where the source is on the concave side of the crystal.

5.3 Design & Implementation

Physical constraints of the imaging hutch require small Bragg and asymmetry angles. For this experiment, we had ready access to a crystal-reflection pair meeting this requirement, namely a (5,1,1) crystal wafer (5" diameter, high-resistivity FZ) with (3,1,1)-type reflection and an asymmetry angle of 3.33° . The magic condition is found by numerically solving $f_p = f_g$ for the Bragg angle. Using $\chi = 3.33^\circ$, $\nu = 0.22$, $f_s = 22$ m, and bend radius $R = -0.5$ m, we find that the magic condition is met for upper-sign geometry with $\theta_B = 7.55^\circ$. The lower-sign geometry yields a numerical solution of $\theta_B = 352.45^\circ$, which is physically the same as $\theta_B = 7.55^\circ$ in upper-sign geometry, and so is discarded. Returning the expanded beam to horizontal requires that the planes of the second crystal be aligned with those of the first. This plane matching puts the second crystal in lower-sign geometry, making it impossible to preserve the magic condition through both crystals.

In order to meet the physical constraints of the rail system installed in the BMIT-BM beamline hutch, we tolerated a slight deviation from the magic condition, specifically a Bragg angle of 6.56° . From previous work {Zhu 2014}, we knew that this Bragg angle adequately approximates the magic condition and furthermore corresponds to the K-edge of Iodine, allowing us to confirm the energy. Ideally we would have preferred to choose this energy first and then obtain custom-cut crystals to match, but this was not feasible for this experiment.

Besides merging the geometric and single-ray foci, the Beam Expanding Monochromator was improved through the development of rigid frame benders (Figure 5.4). The main advantage of a frame bender is the fixed bend radius. The four-bar bender previously used allowed too much variation between experiments and introduced uncertainty as to the true bend radius of the crystal. The frame bender improves reproducibility between crystals, allowing us to mount and swap crystals quickly. It was discovered that crystals designed for the semiconductor industry are not machined with a highly precise asymmetry angle, leading to frequent mismatch between first and second crystal. The simplest way to overcome this variation is by trial-and-error matching in the beamline, which would never have been practical with the lengthy process required for mounting crystals in the four-bar bender. As a solid metal object, the frame bender also supports heat dissipation and water cooling for the first crystal, which exposed to the full white beam of the wiggler beamline.

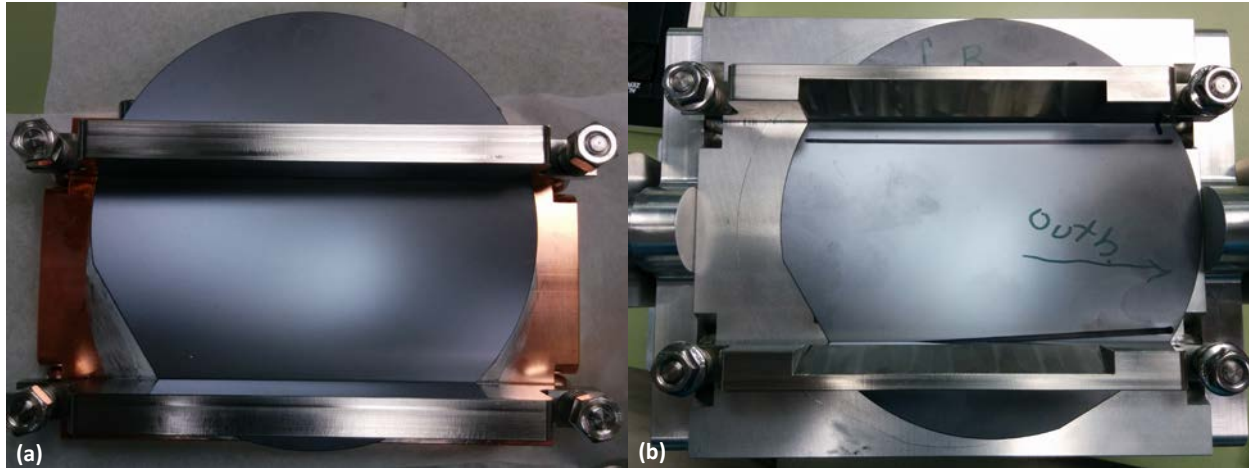


Figure 5.4 (a) First crystal (vacuum-compatible) and (b) second crystal mounted on rigid frame benders. In each figure, the wafers are 5" diameter. As shown, the beam would be coming out of the page.

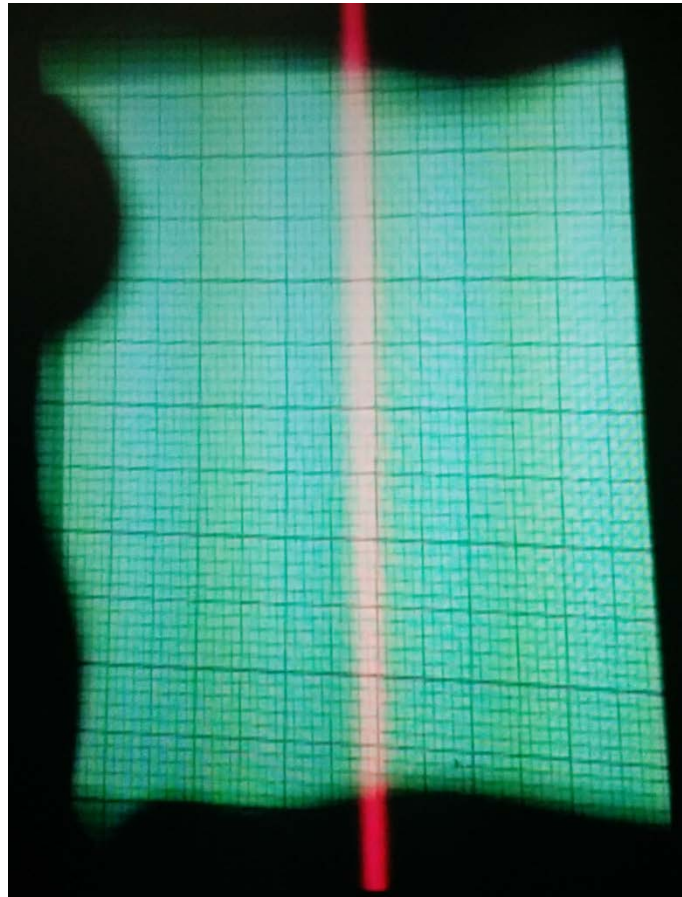


Figure 5.5 Expanded beam at BMIT-ID beamline on fluorescent paper with cm-scale major grid lines.

The biggest disadvantage of the frame bender is that it requires extremely high precision machining, which is not readily available at the CLS. Surface irregularities on the order of 10 μm

seem sufficient to distort the crystal shape enough to cause mismatch between the crystals and ultimately loss of intensity and phase characteristics. Because the first bender must be machined in solid copper for optimal heat dissipation, the additional cost renders this level of high precision machining unfeasible. Attempts to smooth the surface either by additional machining or by inserting smooth intermediate layers distorted the bend radius and triggered catastrophic loss of intensity.

Despite the challenges in machining, the wide rocking curve of the severely bent crystals allowed us to achieve an expansion of approximately 10 \times with adequate uniformity on the BMIT-ID beamline (Figure 5.5).

5.4 Image Analysis and Results

By matching the polychromatic (single-ray) focus to the geometric (multiple ray) focus, we were able to preserve the phase coherence of the X-ray beam while expanding its vertical size by a factor of 12 on BMIT-BM. The final beam size measured 50 mm (V) \times 70 mm (H), the exact size of the window in the second crystal's frame bender, leading us to believe that the true expansion may actually be greater.

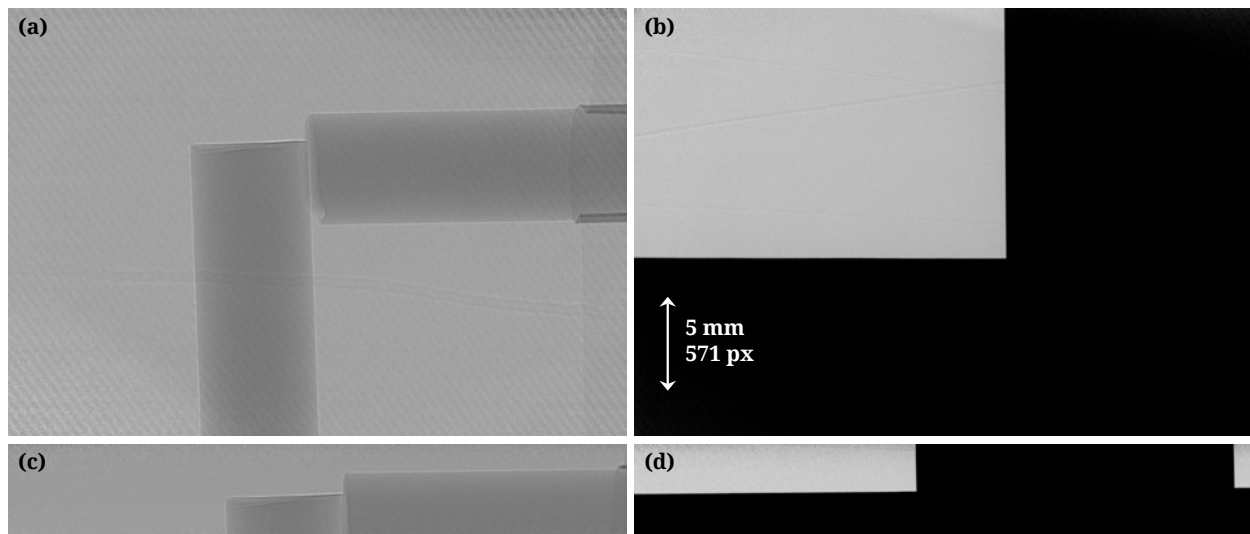


Figure 5.6 Flat-corrected phase and knife edge images used for analysis, also demonstrates field of view of respective monochromators. (a,b) bent Laue monochromator, (c,d) flat Bragg monochromator; (a,c) Lucite Rods, (b,d) Tungsten block. Propagation distance is 134cm. All images have the same scale.

A visual inspection of in-line phase images (Figure 5.6) of a strong phase producing test object (Lucite rods) and a knife edge (tungsten carbide block) showed excellent phase properties in both the vertical and horizontal directions, demonstrating preservation of beam divergence through the expander. The test objects were imaged with a sample-to-detector propagation

distance of 134 cm. These images, acquired using both the expander and the beamline (BMIT-BM) monochromator, were analysed and compared.

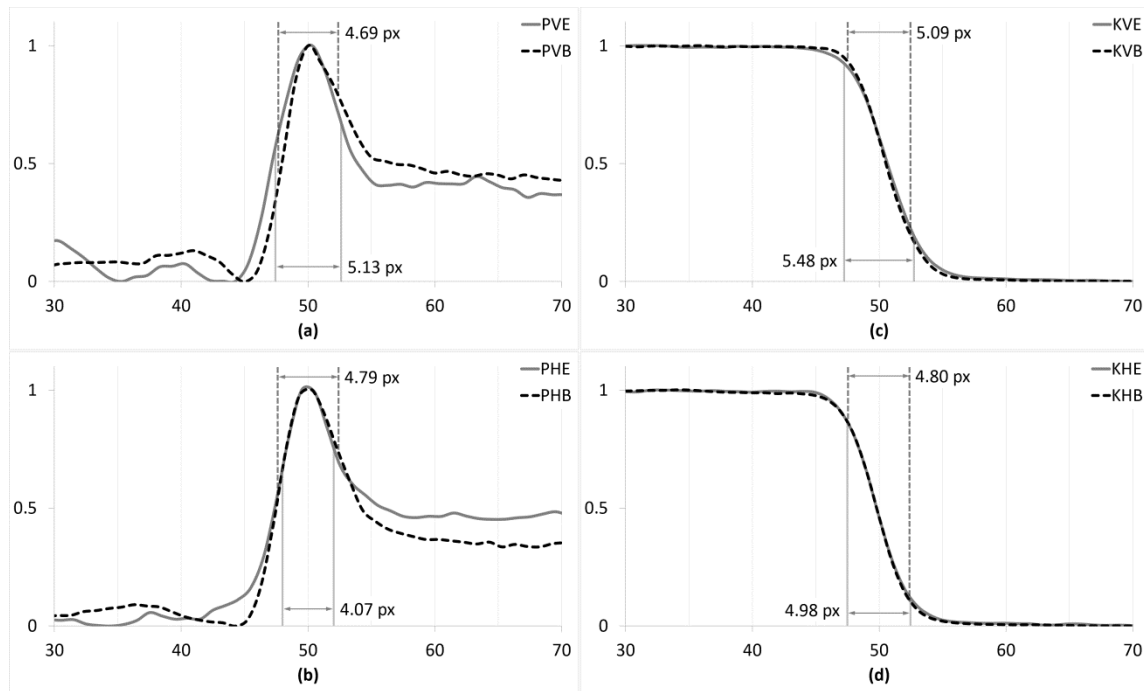


Figure 5.7 Plot profiles with relative intensity on y-axis and pixel range on x-axis. Image type: [K]nife edge or [P]hase fringe. Edge normal: [V]ertical or [H]orizontal. Monochromator type: [B]eamline or [E]xpander. (a) PVE & PVB (b) PHE & PHB (c) KVE & KVB (d) KHE & KHB.

The phase images were analysed using an asymmetric pseudo-Gaussian measurement technique. The peak width across a phase fringe was measured as the distance (in pixels) between the inflection points of the increasing and decreasing sides of the plot profile (Figure 5.7.a,b). The knife edge images were analysed by fitting the derivative of the plot profile (Figure 5.7.c,d) of the knife edge to a Gaussian and measuring the peak width as FWHM. Peak width results for each data set are reported in Table 5.1, along with the percent difference between monochromator type. Positive (negative) differences indicate that the expanding monochromator causes more (less) degradation than the beamline monochromator. From these results, it's evident that the beam is more strongly affected in the vertical direction, although there are also some horizontal effects likely caused by anticlastic bending. We expect the beam to be degraded in the diffraction plane (vertical direction), but we see that this effect is less than 10%. In the horizontal plane, the difference is less than 15%. Because the incident beam is produced by a synchrotron, the coherence of the expanded beam is still well within tolerance for phase-based imaging techniques.

Table 5.1 Summary of analysis results

Image type	Edge normal	Monochromator	Peak width (pixels)	Percent difference
Phase fringe	Vertical	Expander	5.13	9.4%
		Beamline	4.69	
	Horizontal	Expander	4.07	-15%
		Beamline	4.79	
Knife edge	Vertical	Expander	5.48	7.7%
		Beamline	5.09	
	Horizontal	Expander	4.98	3.8%
		Beamline	4.80	

Additional imaging tests were done on biological samples (euthanised mice acquired from other experiments), demonstrating the true capability of the biomedical imaging system (Figure 5.8).

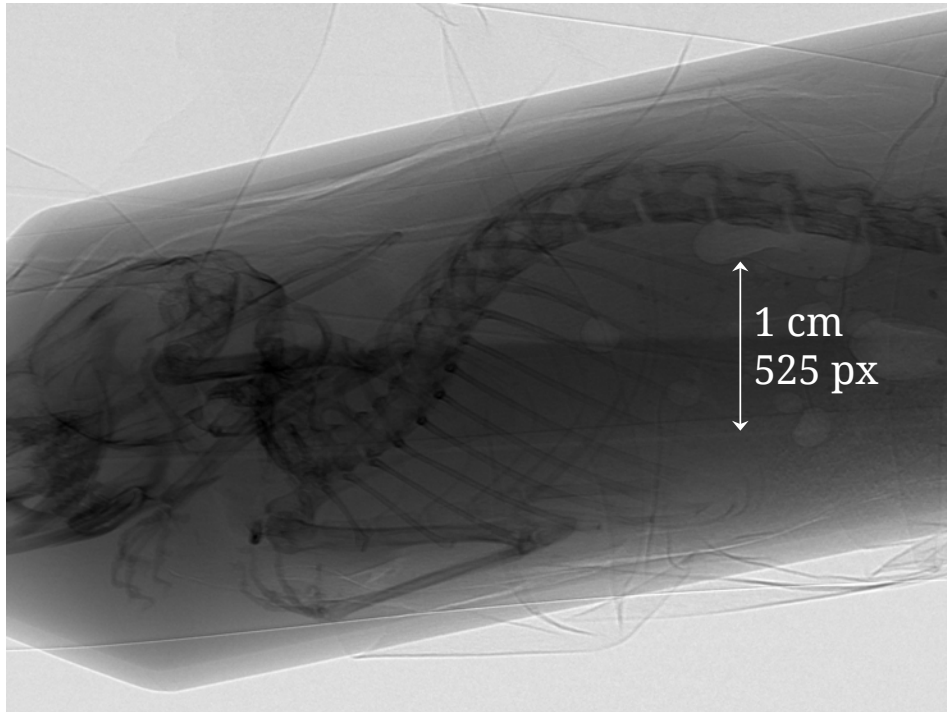


Figure 5.8 Phase image of euthanised mouse. Propagation distance approximately 200cm.

There are other potential applications for this crystal geometry using the magic condition that preserves phase. One common application of dual bent Laue crystals is microfocusing synchrotron beams. Using this particular geometry and magic condition, it should be possible to create these microbeams in a way that preserves beam coherence and phase properties. This could have applications to microprobe and crystallography.

5.5 Conclusion

We have demonstrated that a beam expanding monochromator is able to preserve the beam coherence and phase properties of a synchrotron beam by carefully matching the geometric and polychromatic focal lengths of two cylindrically bent crystals in Laue diffraction mode. Imaging experiments demonstrated excellent phase contrast in a biological sample as well as phase and knife edge test objects. Visual analysis confirmed that horizontal and vertical phase fringes and knife edges were comparably affected, and the numerical analysis confirmed that the differences between them were less than 10% in the diffraction (vertical) plane. While this is not perfect, it is noted that we were not operating at the optimal Bragg angle on account of the apparatus already in place at the beamline. Future work will repeat the phase and knife edge experiments at the exact energy determined by numerically solving the equations.

While these experiments were done in “expansion mode,” it should be possible to reverse the crystals and run the system in “compression mode.” Everything discussed in this work should hold true in the reverse orientation, as only the sign of the bend radius will change. This modality will be the topic of future work.

Acknowledgements: Mercedes Martinson, Nazanin Samadi, and Bassey Bassey are Fellows, and Dean Chapman is a Mentor, in the Canadian Institutes of Health Research Training grant in Health Research Using Synchrotron Techniques (CIHR-THRUST). This work is supported in part by a Discovery Grant from the Natural Sciences and Engineering Research Council of Canada (NSERC) and Canada Research Chair. Research described in this paper was performed at the Canadian Light Source, which is funded by the Canada Foundation for Innovation, NSERC, the National Research Council Canada, the CIHR, the Government of Saskatchewan, Western Economic Diversification Canada, and the University of Saskatchewan. The authors wish to acknowledge the excellent support received by Dr. George Belev and the other BioMedical Imaging and Therapy beamline staff.

Chapter 6 Measuring the criticality of the ‘magic condition’ for a beam expanding monochromator

Citation: M. Martinson and D. Chapman, *Measuring the criticality of the ‘magic condition’ for a beam-expanding monochromator*. Journal of Synchrotron Radiation, 2016. 23(6): p. 1498-1500.

Disclaimer: Reproduced with permission. Manuscript has been reformatted for consistency with the dissertation, including some rearrangement. References have been moved to the end of the dissertation as per CGSR requirements. Contact information has been removed. Figures have been recreated from the source material to improve image quality. No content has been changed.

Copyright IUCr, reproduced with permission (<http://dx.doi.org/10.1107/S1600577516012650>).

Measuring the criticality of the ‘magic condition’ for a beam expanding monochromator
M. Martinson¹ and D. Chapman^{1,2}

¹ Physics and Engineering Physics, University of Saskatchewan, Saskatoon, SK

² Anatomy & Cell Biology, University of Saskatchewan, Saskatoon, SK

Keywords: Magic condition; bent Laue double crystal monochromator; geometric and polychromatic focus

Synopsis: The effect of minor mismatch between the geometric and single-ray foci for a cylindrically bent Laue double crystal monochromator is examined and found to be less detrimental than previously believed. Even without exact matching, the transverse coherence of x-ray beam is not deteriorated by the system, enabling the phase-based imaging techniques critical to modern biomedical imaging experiments.

Abstract: It has been established that for cylindrically bent crystals, the optimal beam characteristics occur when the geometric and single-ray foci are matched. In the beam expanding monochromator developed for the BioMedical Imaging and Therapy beamlines at the Canadian Light Source, it was unclear how critical this “magic condition” was for preserving the transverse coherence of the beam. A study was conducted to determine if misalignments away from the ideal conditions would severely affect the transverse coherence of the beam, thereby limiting phase-based imaging techniques. The results were that the magic condition has enough flexibility to accommodate deviations of about $\pm 1^\circ$ or ± 5 keV.

6.1 Introduction

A double bent Laue beam expanding monochromator has been designed for the BioMedical and Imaging Therapy beamlines at the Canadian Light Source. During our earlier work {Martinson 2014}, significant beam blurring in the vertical direction (corresponding to horizontally oriented object edges) was believed to be caused by a mismatch between the single-ray and geometric focus types. A key improvement in the design was the preservation of the transverse coherence of the beam {Martinson 2015}, which allows phase-sensitive imaging techniques to be performed with a large field of view. This was achieved by matching the two focus types (single-ray focus, f_p , and geometric focus, f_g) in the first crystal to each other and to the geometric focus of the second crystal. At the time, it was unclear how sensitive the system was to deviations from this “magic condition.”

Single-ray focus equation {Martinson 2015}:

$$f_p = \pm \frac{R \sin 2\theta_B}{2 \sin(\chi \pm \theta_B) + (1 + \nu) \sin 2\chi \cos(\chi \pm \theta_B)} \quad 6.1$$

Geometric focus equation {Schulze 1998}:

$$\frac{\cos(\chi \mp \theta_B)}{f_g} - \frac{\cos(\chi \pm \theta_B)}{f_s} = \frac{2}{R} \quad 6.2$$

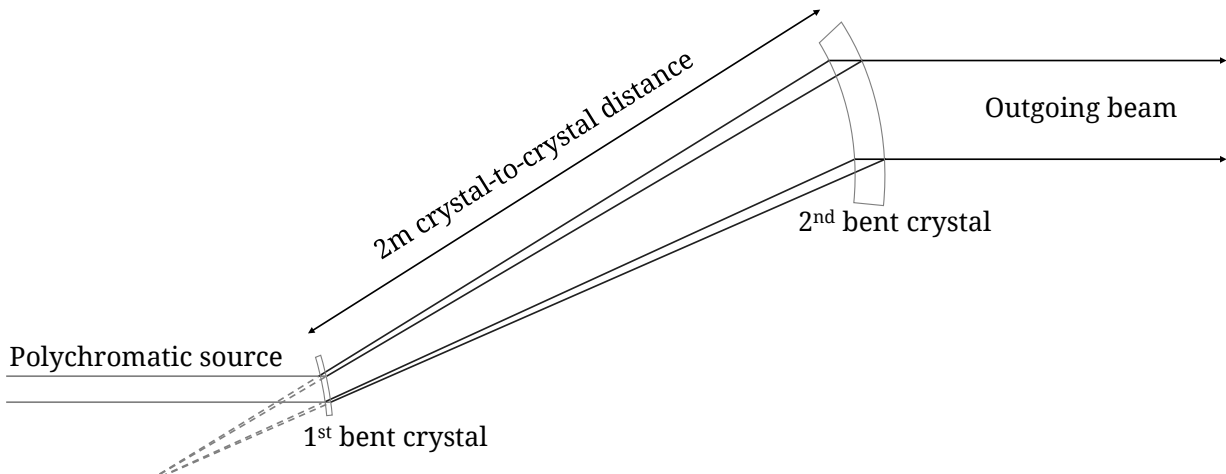


Figure 6.1 Experimental setup.

For this study, the magic condition was determined from the first crystal in the expander system, which uses a (3,1,1)-type reflection on a (5,1,1) silicon wafer (producing an asymmetry angle of $\chi=3.33^\circ$), at a bend radius $R = 0.5$ m and a source-to-crystal distance $f_s = 22$ m for the

BMIT bend magnet beamline. By setting $f_p = f_g$ and assuming a Poisson ration of $\nu = 0.22$, the magic condition is determined numerically to occur at a Bragg angle $\theta_B = 7.55^\circ$.

6.2 Experimental procedure

The beam expanding system was setup as in {Martinson 2014} with the geometric focus of the second crystal matched to that of the first crystal (Figure 6.1). The bend radii of the first and second crystals were 0.5 m and 5 m, respectively, producing an expansion factor of approximately 10, with a crystal-to-crystal distance of approximately 2 m. Using a Hamamatsu detector (AA-60 beam monitor coupled to C9300-124 CCD camera resulting in a field of view of 31.08 mm H \times 23.31 mm V and pixel size 8.75 μm) and object-to-detector distance of 134 cm, images of a knife edge (tungsten bar) and phase object (Lucite rod) were captured through Bragg angles ranging $\pm 1^\circ$ from the magic condition. At each Bragg angle, the two crystals were carefully aligned (*i.e.* diffraction planes and geometric foci were matched) to optimise beam intensity.

6.3 Analysis

Both vertically and horizontally oriented edges were analysed for each test object and Bragg angle using the procedure in {Martinson 2015}. The phase peak width was measured using a pseudo-Gaussian fit to measure the distance (in pixels) between inflection points in the plot profile. The knife edge width was measured as the FWHM (in pixels) of a Gaussian fit to the derivative of the plot profile. To account for misalignment between the samples' edges and the detector pixel lines, the peak width was minimised with respect to the rotation angle of cropped subsections (100 pixels wide across the edge and varying between 5, 10, 25 pixels wide along the edge). The final width measurement for each edge was then taken as the mean of these minimised widths, with an uncertainty equal to half the difference of the largest and smallest. The measurement results are presented in Table 6.1, where the horizontal and vertical labels refer to the orientation of the object's edge relative to physical space and are perpendicular to the vertical and horizontal diffraction planes respectively.

6.4 Discussion

In the knife edge images, the vertical and horizontal edges all agreed within experimental uncertainty at each Bragg angle, differing by at most 0.72%. The expectation of the vertical edges width being equal at all Bragg angles was very nearly realised, with the 8.55° sample failing equality by only 0.004 pixels.

In the phase images, these results do not hold. It is noted that the signal-to-noise (SNR) ratio in the phase images was very poor due to the significant noise of the images and low relative

signal of the phase fringe. This likely caused poor fits in the procedure, resulting in unreliable results. Nonetheless the measurements are presented for completeness.

Table 6.1 Peak widths of phase and knife edge images as a function of Bragg angle

Bragg angle	Energy (keV)	Knife object			Phase object		
		Fringe width in pixels	Horizontal	$\frac{ V - H }{V} \times 100\%$	Edge width in pixels	Horizontal	$\frac{ V - H }{V} \times 100\%$
6.55°	33.2	3.058 ± 0.010	3.042 ± 0.008	0.52%	3.316 ± 0.039	5.119 ± 1.162	54%
7.05°	30.9	3.059 ± 0.009	3.059 ± 0.007	0.00%	4.501 ± 0.085	4.982 ± 2.591	11%
7.30°	29.8	3.076 ± 0.020	3.063 ± 0.010	0.42%	4.718 ± 0.241	6.414 ± 2.210	36%
7.55°	28.8	3.073 ± 0.020	3.063 ± 0.010	0.33%	4.761 ± 0.010	4.505 ± 0.621	5.4%
7.80°	27.9	3.059 ± 0.012	3.037 ± 0.010	0.72%	3.621 ± 0.003	7.092 ± 2.624	96%
8.05°	27.0	3.063 ± 0.010	3.054 ± 0.005	0.29%	3.948 ± 0.190	4.302 ± 0.443	9.0%
8.55°	25.5	3.051 ± 0.001	3.058 ± 0.007	0.23%	6.868 ± 0.025	5.114 ± 0.823	26%

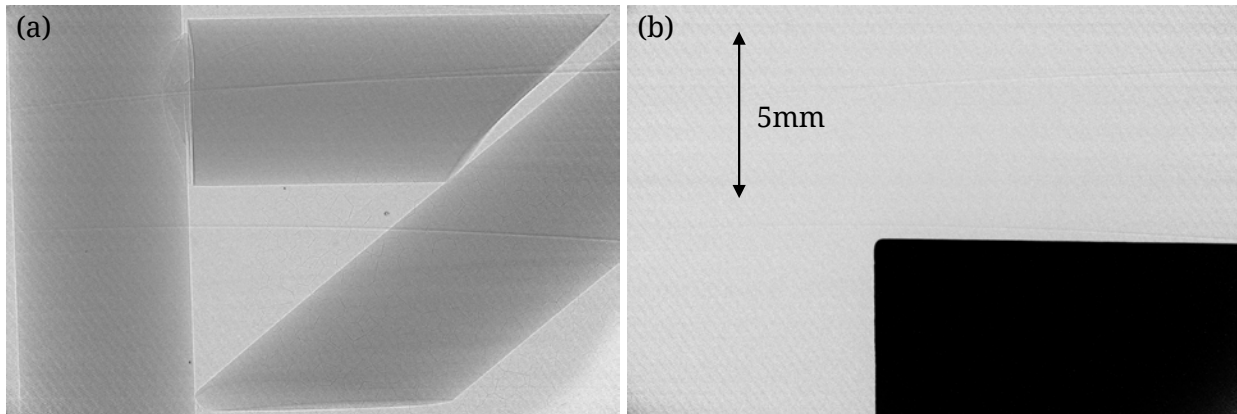


Figure 6.2 Sample (a) phase and (b) knife edge images.

6.5 Conclusion

Overall, the small difference in edge width as the angle moves away from the magic condition, along with visual inspection of the phase images at all Bragg angles measured, indicates that strict magic conditions are not required for the purposes of medical imaging. This is advantageous for applications that require specific energies (*e.g.* K-edge subtraction) or beamline configurations (*e.g.* fixed Bragg angle due to apparatus construction). This creates flexibility in the system, as a separate set of crystals with specific asymmetry angles is not required in order to change energies. While ideal matching may be required for certain microfocusing applications of bent Laue double crystal monochromators, it would appear that as long as both crystals are in the upper sign geometry (*i.e.* the tilt angle of crystal is $\chi + \theta_B$ instead of the $\chi - \theta_B$ tilt that is now believed to be the primary cause of the beam blurring observed in our earlier work {Martinson 2014}), the system will produce a suitable beam for biomedical imaging with phase contrast techniques.

Acknowledgements: Mercedes Martinson is a Fellow and Dean Chapman is a Mentor in the Canadian Institutes of Health Research Training grant in Health Research Using Synchrotron Techniques (CIHR-THRUST). This work is supported in part by a Discovery Grant from the Natural Sciences and Engineering Research Council of Canada (NSERC) and Canada Research Chair. Research described in this paper was performed at the Canadian Light Source, which is funded by the Canada Foundation for Innovation, NSERC, the National Research Council Canada, the CIHR, the Government of Saskatchewan, Western Economic Diversification Canada, and the University of Saskatchewan. Data was collected at the Biomedical Imaging and Therapy bend magnet beamline (05B1-1) at the Canadian Light Source. Research described in this paper was performed at the Canadian Light Source, which is funded by the Canada Foundation for Innovation, NSERC, the National Research Council Canada, the CIHR, the Government of Saskatchewan, Western Economic Diversification Canada, and the University of Saskatchewan

Chapter 7 Characterisation of a bent Laue double crystal beam expanding monochromator

In preparation for submission to Journal of Synchrotron Radiation

Characterisation of a bent Laue double crystal beam expanding monochromator

M. Martinson¹, N. Samadi¹, X. Shi², L. Assoufid², and D. Chapman^{1,3}

¹ Physics and Engineering Physics, University of Saskatchewan, Saskatoon, SK

² X-ray Science Division, Argonne National Laboratory, Illinois, U.S.

³ Canadian Light Source, Saskatoon, SK

Keywords: Keywords: beam expander; double bent Laue monochromator; Lang topography; Berg-Barrett topography; finite element analysis

Synopsis: Previously reported bent Laue double crystal monochromator was found to have areas of missing intensity in the final x-ray beam. Measurements of the shape of the bent crystal wafers have been made using mechanical and diffraction methods to evaluate the crystal system and provide insight into potential methods of mitigating the non-uniformities in the beam.

Abstract: A bent Laue double crystal monochromator system has been designed for vertically expanding the x-ray beam at the Canadian Light Source's (CLS) BioMedical Imaging & Therapy (BMIT) beamlines. Expansion of a factor of 12 has been achieved without deteriorating the transverse coherence of the beam, allowing phase-based imaging techniques to be done with high flux and a large field of view. However, preliminary studies demonstrated a lack of uniformity in the beam, presumed to be caused by imperfect bending of the silicon crystal wafers used in the system. Measurements have been taken to characterise the bending of the crystals using both mechanical and diffraction techniques. In particular, two techniques commonly used to map dislocations in crystal structures have been adapted to map local curvature of the bent crystals. The results of these measurements are presented here along with suggestions to improve the bending method and thereby eliminate the regions of missing intensity in the imaging beam. Results from finite element analysis of the system predicted that the second crystal would be most severely affected and this has been shown to be the case. It has been determined that the majority of the distortion occurs in the second crystal and is likely caused by an imperfection in the surface of the bending frame.

7.1 Introduction

The BioMedical Imaging & Therapy (BMIT) beamlines at the Canadian Light Source would greatly benefit from an increase in the vertical size of the x-ray beam, which would enable dynamic imaging of animal samples that are larger than what is currently possible. Preserving the quality of the transverse coherence while expanding the beam would enable phase imaging techniques in a field of view capable of completely covering many small animals, extending the beamline's capabilities to functional dynamic imaging of soft tissue such as lungs. Making full use of the large animal imaging stage, a feature unique to this facility {Wysokinski 2007}, similarly requires a larger field of view. Previous results {Martinson 2014, Martinson 2015} reported on the development of a phase-preserving bent Laue beam-expanding double-crystal monochromator: two silicon (Si) crystal wafers were cylindrically bent with the concave sides facing the x-ray beam and arranged with the geometrical foci of both crystals co-located and the diffraction planes parallel between each crystal as in Figure 7.1. This system increased the vertical size of the x-ray beam by a factor of 12 without adversely affecting the transverse coherence in the diffraction plane. These initial experiments were done on the bend magnet beamline {Wysokinski 2007}. However, the intensity of the final beam was not uniform across the entire field of view (Figure 7.2.a). In particular, one region was severely affected with a large “hole” present in the beam. In order to overcome this problem, it was first necessary to characterise the bending of the crystal wafers. Measurements of the bent crystals mounted in the solid bending frame were taken using both mechanical and diffraction methods. The mechanical measurements indicated an area of the crystal with significant physical distortion that corresponds exactly to the location of the hole in the expanded beam. The diffraction measurements also clearly indicated a large area of distortion in the second crystal corresponding both to the hole in the beam and the area of physical distortion in the crystal surface.

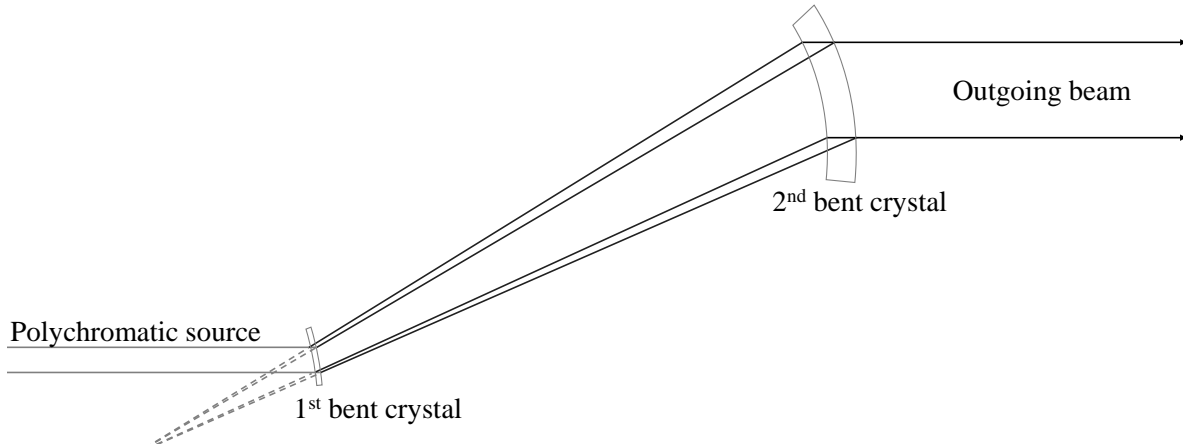


Figure 7.1 Schematic of bent Laue double crystal system.

7.2 Background

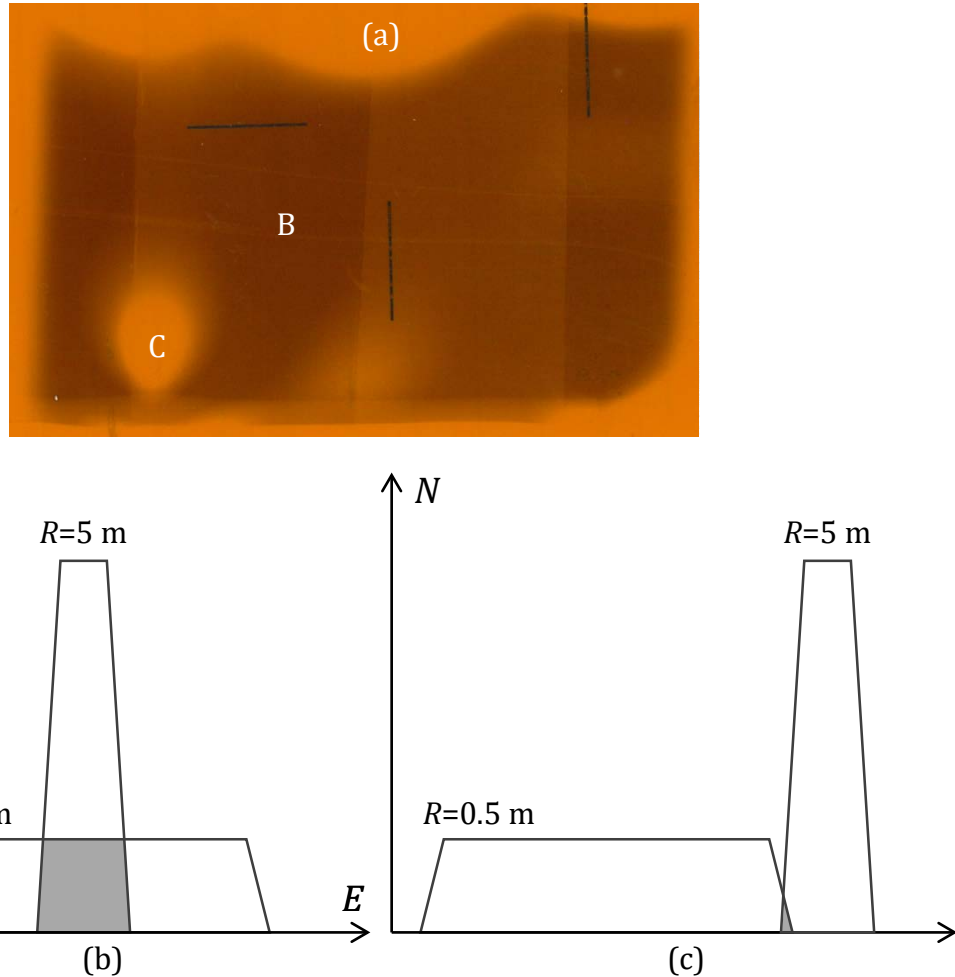


Figure 7.2 (a) Double-diffracted expanded beam showing intensity distribution due to distortion in crystal. Areas B and C show low and high intensity, respectively, and corresponding reflectivity curves (b) overlapping and (c) failing to adequately overlap.

7.3 Finite Element Analysis

The crystals used in this work were Si(5,1,1) wafers with the (3,1,1)-type reflection aligned to the Iodine K-edge (33.2 keV). At 0.5 m and 5 m bend radii, these crystals were within the kinematic limits of diffraction theory {Suortti 1997}. Thus we expect that for a given crystal thickness, the integrated reflectivity is constant and equal to the product of the peak reflectivity and the width of the reflectivity curve {Erola 1990, Suortti 1995} (Figure 7.2.b). Since the integrated reflectivity is roughly proportional to the crystal thickness (neglecting absorption), it follows that maximum efficiency from the system occurs when the ratio of the crystal thicknesses is equal to the ratio of bending radii, *i.e.* the crystal with the 5 m bend radius should be 10x thicker than that with the 0.5 m bend radius in order to completely overlap their reflectivity curves and make use of all the x-rays exiting the first crystal. It is suspected that the area of

missing intensity occurs because the reflectivity curve of the second crystal falls completely outside that of the first (Figure 7.2.c).

It is well-known that anticlastic bending is an important factor whenever crystals are bent {Zontone 1992}. It was suggested that the lack of uniformity in the beam could be caused by a severe mismatch between crystals caused by anticlastic bending. This would lead to missing intensity along the side edges of the beam due to mismatch of the crystal planes, however this effect would be mitigated as the anticlastic bending should contribute a relatively small component to the diffraction angle. Finite element analysis (FEA) was used to predict the expected shape of the crystals when bent with the solid frame bender. Using the design parameters for the bending frames (0.5 m and 5 m cylindrical slabs), the actual bend radii predicted for the crystals were 0.518 m and 5.06 m respectively, with anticlastic bend radii of 51.4 m and 70.8 m. This indicates that the second crystal may be more adversely affected by anticlastic bending due to its larger bend radius and lower tolerance for small irregularities. As the anticlastic bend radii are on the same order of magnitude and perpendicular to the diffraction plane, we don't expect serious effects on intensity, despite the comparatively larger ratio between principal and anticlastic bend radii in the second crystal. Naturally this analysis did not predict the hole of missing intensity as this was likely caused by imperfections in the physical bending frame.

7.4 Mechanical measurements

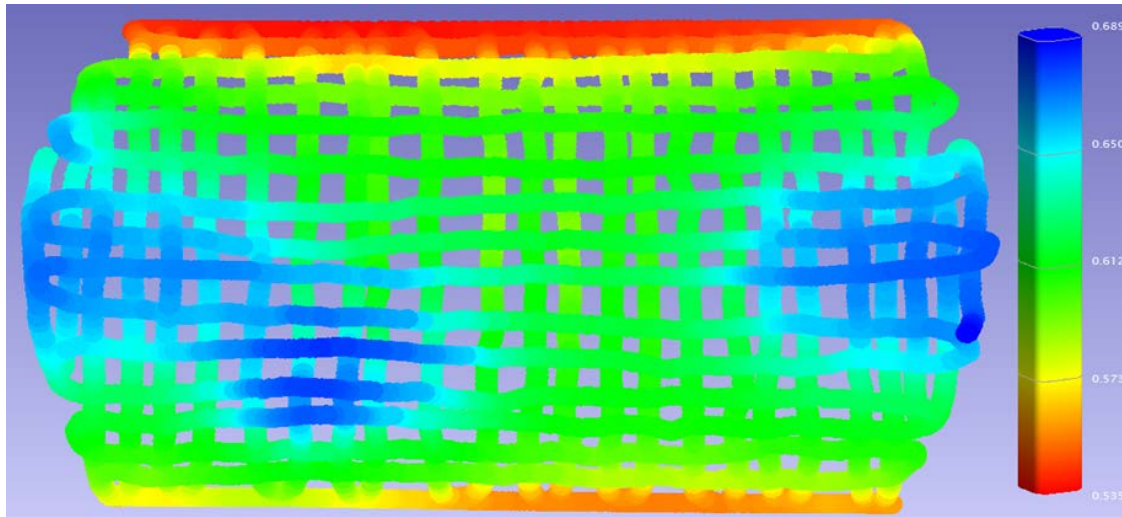


Figure 7.3 3D physical mapping of 5 m bend radius crystal surface. Colour represents distance in mm from a plane fit parallel to viewing angle and normal to centre of surface. Due to inconsistencies in the measurements, exact distortion cannot be quantified, but is easily visible in the mapping, along with anticlastic bending along the side edges.

As we suspected imperfections in the physical bend, the natural first step was to measure the bent crystals mechanically using a FaroArm (FARO Technologies Ltd). These tests indicated

that each crystal was within 1% of the desired bend radius. A 3-dimensional mapping of the surface of each crystal detected physical imperfections in the surface of the 5 m bend radius wafer, indicated by an area of raised height in the crystal surface corresponding to a small bump in the edge of the bending frame window (Figure 7.3). This area matches exactly with the hole in the expanded beam and is believed to be the cause of the missing intensity.

7.5 Bent crystal rocking curve measurements (Bragg-Bragg mode)

The first set of diffraction measurements was performed at the Advanced Photon Source Optics & Detector Testing beamline {Macrander 2016}. An 8 keV monochromatic beam produced by the beamline's double crystal monochromator was conditioned by a flat Si(3,3,3) crystal that has an asymmetry angle of 46.6°. Using this expanded beam to completely flood the surface of the bent crystals in a variation of Berg-Barrett topography {Turner 1968}, the 5 m and 0.5 bend radius Si(5,1,1) crystals were rocked in 1° and 0.1° increments, respectively (Figure 7.4). As the bent crystal is rotated in the diffraction plane, the monochromatic beam exiting the first crystal finds the matching Bragg planes at different locations in the bent crystal, producing a map of the local curvature. After diffraction from the bent crystal, the x-ray beam was imaged using a Princeton Instruments PIXIS x-ray detector (13mm × 13mm field of view with 13 μ m pixel size). These images were stitched together to form a “zebra stripe” image for each crystal (Figure 7.5).

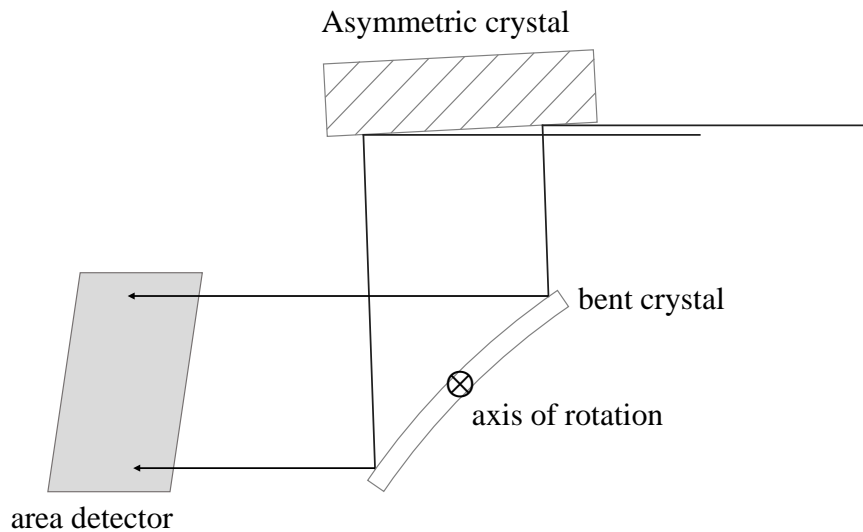


Figure 7.4 Variation of Berg-Barrett topography with bent crystal.

The Bragg-Bragg technique with a highly asymmetric conditioning crystal was chosen primarily for of the low dispersion of the beam. The main disadvantage of this technique is that the expander setup uses the crystals in Laue-Laue diffraction mode, so there were concerns that the results may not be transferrable. The technique also measures the convex side of the crystal

whereas we expected most of the distortion to be introduced by contact between bending frame and the concave side of the wafer. However, the excellent match between the regions of reduced intensity in the double-diffracted beam and the distortion in the crystal indicates that these concerns were unwarranted.

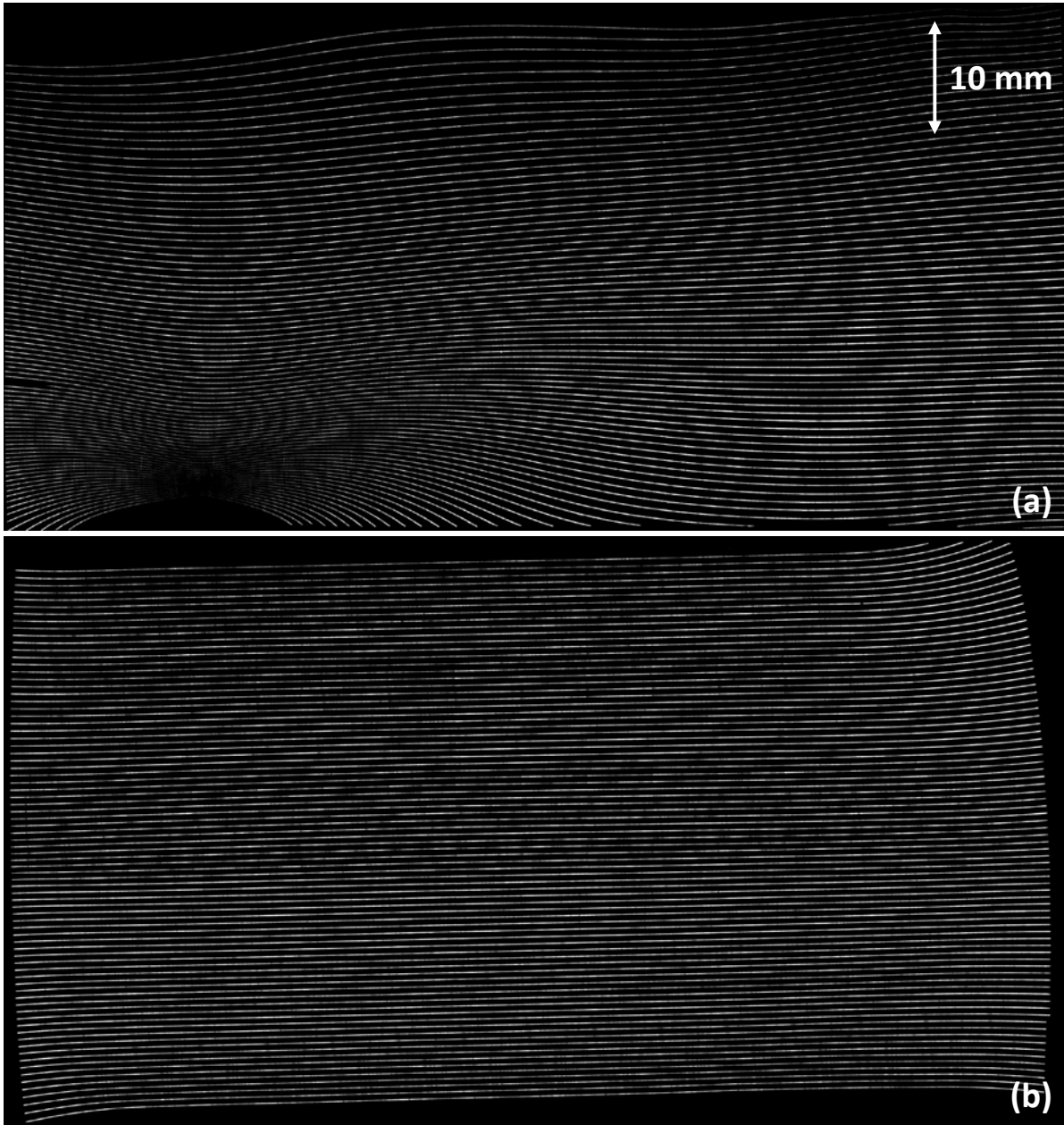


Figure 7.5 Bragg-Bragg bent crystal rocking curves. (a) 5 m bend radius; note severe distortion in lower-left corner and oscillating distortion along top edge. (b) 0.5 m bend radius; anti-clastic bending evident along sides and corners.

It was immediately clear that the region of missing intensity in the double-diffracted beam exiting the beam expander exactly corresponds to the region of severe distortion in the second

crystal (5 m bend radius). The distortion along the top of this crystal also corresponds to a region along the top of the imaging beam that is similarly missing intensity. The first crystal (0.5 m bend radius) is relatively well-bent. The effects of anticlastic bending are visible along the outer sides of the beam, however the central region where the beam passes through is nearly perfectly bent, indicating that the regions of missing intensity in the expanded beam are primarily caused by the second crystal.

7.6 Bent crystal rocking curves (Laue-Laue mode)

The second set of diffraction measurements was performed at the Canadian Light Source Biomedical Imaging and Therapy beamline. In order to match the diffraction conditions of the expander, these experiments were performed using Laue-Laue diffraction with a (3,1,1)-type reflection from a Si(5,1,1) wafer, just as in the expander experiments. In a variation of Lang projection topography {Lang 1959}, each bent silicon crystal wafer was rocked against a flat conditioning silicon crystal wafer (Figure 7.6). As the bent crystal is rotated in the diffraction plane, the monochromatic beam exiting the first crystal finds the matching Bragg planes at different locations in the bent crystal, producing a map of the local curvature. The 5 m and 0.5 m bend radius wafers were rocked in 0.02° and 0.2° increments, respectively, and the axis of rotation was offset from the crystal surface so that local changes in curvature resulted in vertical displacements of the diffraction lines in the detector (Hamamatsu AA-60 beam monitor coupled to C9300-124 CCD camera with $8.75 \mu\text{m}$ pixel size). The full-field exposure of the Berg-Barrett-type beam was simulated by scanning the bent crystal vertically and stitching the images together.

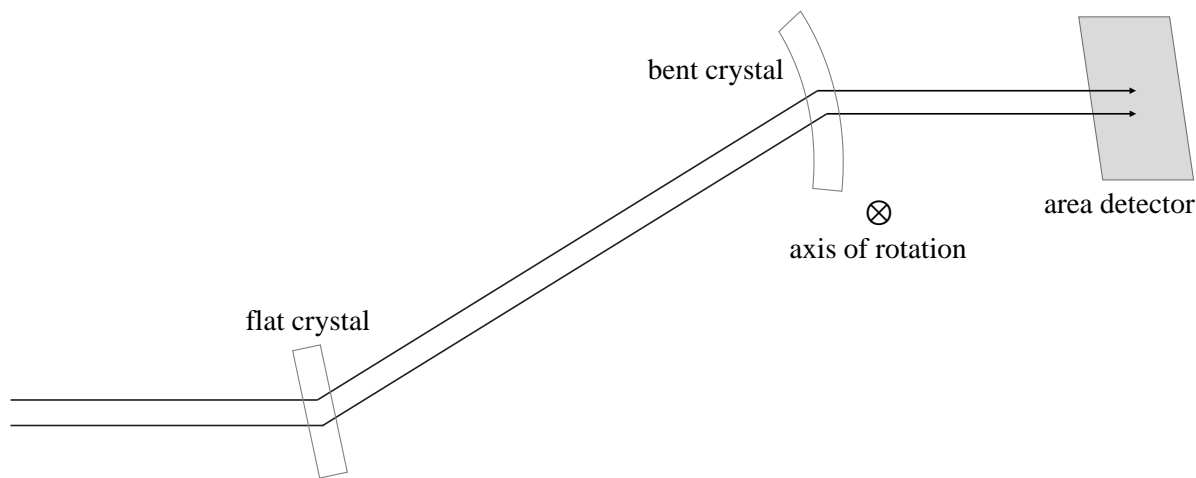


Figure 7.6 Variation of Lang topography with bent crystal.

Reconstructed images are presented in Figure 7.7. Here it is noted that for the 0.5 m bend radius, the diffraction lines show only slight signs of anticlastic bending compared to the Bragg-Bragg measurements. This is primarily because window in this frame limits the beam size and

within this region, the anticlastic bending is virtually non-existent. Once again, it is observed that the beam produced by the first crystal is of excellent quality and that the areas of missing intensity in the final beam correspond exactly to the areas of distortion in the second crystal. This is reasonable given the large bend radius, as small distortions in the surface of the bending frame or crystal are proportionally much larger, magnifying their effects as compared to the 0.5 m bend.

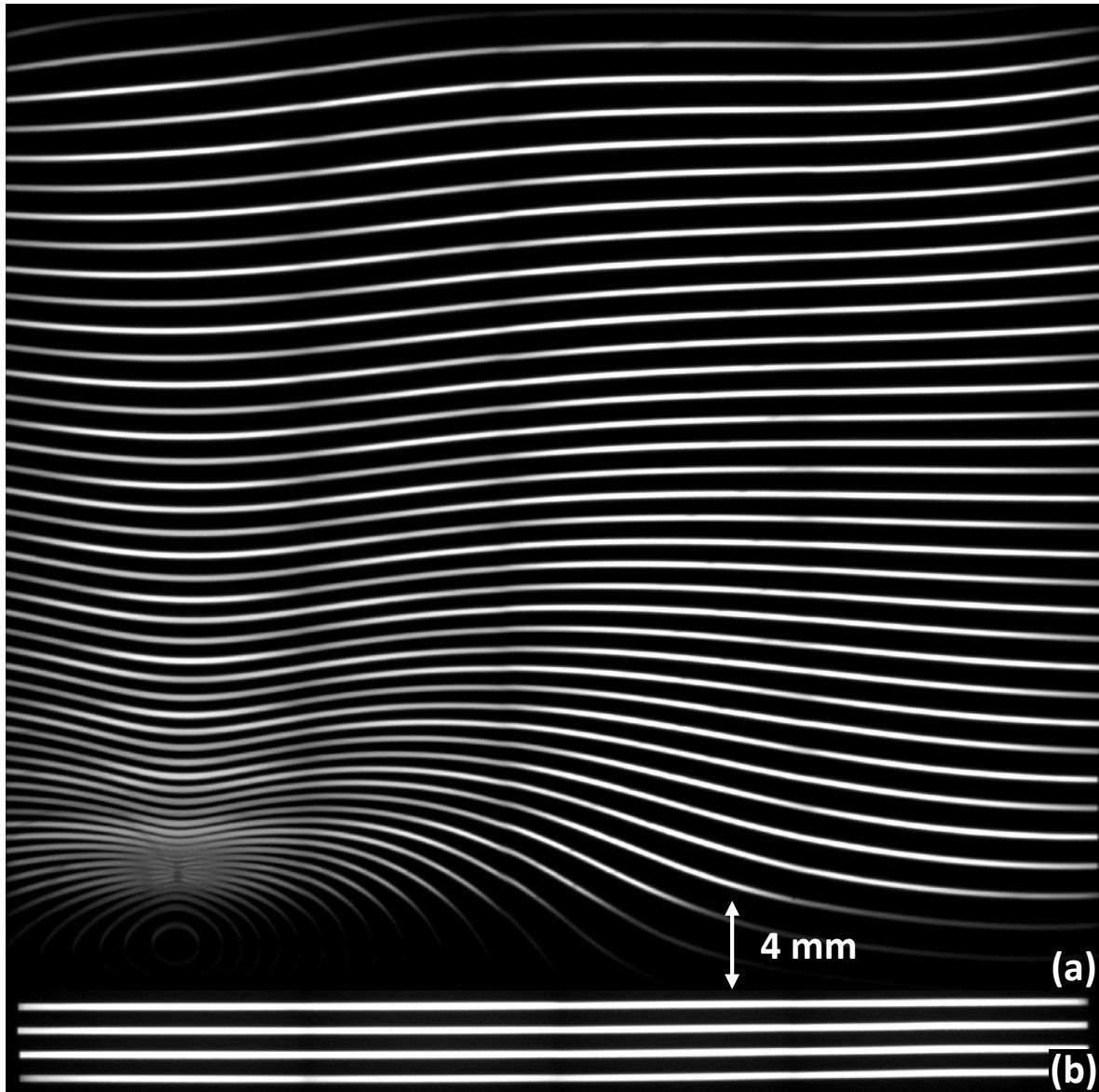


Figure 7.7: Laue-Laue bent crystal rocking curves. (a) 5 m bend radius; the areas of uniformly low intensity at the top and bottom of the 5 m image are caused by absorption in the Aluminium frame. (b) 0.5 m bend radius; Laue-diffracted rays are nearly perfectly straight and parallel.

Acknowledgements: The authors wish to thank Madison Adam, Ed Unrau, and Lawrence Pirness (Canadian Light Source, Engineering & Technical Services) for performing the FaroArm measurements and compiling its data; Albert Macrander (Advanced Photon Source, Optics Fabrication and Metrology) for assisting with data collection at APS; and George Belev (Canadian Light Source, BMIT) for assisting with data collection at CLS. MM and NS are Fellows, and DC is a Mentor, in the Canadian Institutes of Health Research Training grant in Health Research Using Synchrotron Techniques (CIHR-THRUST). This work is supported in part by a Discovery Grant from the Natural Sciences and Engineering Research Council of Canada (NSERC) and Canada Research Chair. Research described in this paper was performed in part at the Canadian Light Source, which is funded by the Canada Foundation for Innovation, NSERC, the National Research Council Canada, the CIHR, the Government of Saskatchewan, Western Economic Diversification Canada, and the University of Saskatchewan. Data was collected in part at the Biomedical Imaging and Therapy bend magnet beamline (05B1-1) at the Canadian Light Source. Data was collected in part at the Optics & Detector Testing Beamline (1-BM-B) at the Advanced Photon Source, Argonne National Laboratory. This research used resources of the Advanced Photon Source, a U.S. Department of Energy (DOE) Office of Science User Facility operated for the DOE Office of Science by Argonne National Laboratory under Contract No. DE-AC02-06CH11357.

Chapter 8 Conclusion & Future work

8.1 Conclusions

The initial set of experiments produced a beam expansion between 2 \times and 7 \times by using a Si(5,1,1) wafer with a (2,2,0)-type reflection. This produced a beam approximately 40 mm vertical \times 94 mm horizontal, which is adequate for most small animal studies (full-body) and some larger animals (*e.g.* joints or prostate). Later experiments achieved an expansion of 12 \times without dispersion.

The quality of the beam was evaluated using micro-computed tomography imaging, phase-based imaging, and dynamic imaging. While the CT images were sharp and clear with good resolution of detail, the phase images lacked a discernible phase fringe, leading us to believe there was a fundamental problem with the beam. Further investigation of knife edge images demonstrated that horizontal object edges were blurred due to excessive dispersion in the x-ray beam. This was initially attributed to imperfect matching between the polychromatic and single-ray focal points. Only after performing the focus study did it become clear the two foci were on opposite sides of the crystal, explaining the severity of the blurring in the first experiments. The true potential power of the expander was demonstrated by capturing a full speed (30 fps) movie of a live mouse. The intensity was more than adequate to expose the flat panel detector with good signal-to-noise ratio.

Further evaluation was done to measure the flux of the beam at 20 keV, a typical imaging energy. Unfiltered, the expander produces a flux of 1.2×10^7 ph/s \cdot mm 2 \cdot mA (photons per second per square millimetre of exposed area per milliamp of ring current) which would deliver a radiation dose of 4 μ Gy/s \cdot mA (microgrey per second per milliamp of ring current) to imaging samples in the beam. In comparison, the beamline's double crystal flat Bragg monochromator produces a flux of 5.7×10^6 ph/s \cdot mm 2 \cdot mA. The reason for the expander's 2.1 \times increase in flux in the expander is the result of the increased energy bandwidth and comes at the cost of pure monochromaticity.

The system was then improved by carefully matching the polychromatic and single-ray focal points. This eliminated the dispersion problem from the first set of experiments and produced a beam that did not degrade the transverse coherence, thus enabling the phase-based imaging techniques that rely on this property. In this set of experiments, an expansion of 12 \times was achieved, however with a large region of missing intensity in the final beam. The beam was evaluated using knife edge and phase object images, which produced sharp lines and clear phase fringes, respectively. Analysis of the knife edge images demonstrated that the expander did not

adversely affect the beam in the diffraction plane, and that vertical and horizontal knife edges had comparable widths with differences of less than 10%.

Further tests were done to establish the flexibility of this “magic condition” and it was found that the system is stable to at least ± 5 keV. Between all energies and knife edge orientations (vertical and horizontal), edge widths differed by at most 0.72% (less than $0.35\mu\text{m}$). It is believed that the system would be stable to a much higher energy range however testing of this was not possible with the physical limitations of the rail system in the hutch.

Characterisation of the bent crystals was performed using both diffraction and mechanical measurement techniques. Both Bragg- and Laue-based diffraction techniques located a distorted area in the second crystal that exactly matches the position of missing intensity and is believed to be its cause. The mechanical measurement confirms the presence of a bump in this region, and closer investigation of the bending frame itself confirms the presence of a defect in the surface. This confirms that the missing intensity is due to imperfect bending rather than defects in the crystal lattice structure.

8.2 Future Research

At the time of writing, analysis is being done to quantify the distortion in the second crystal using the diffraction measurements and compare them to the mechanical measurements to confirm that the missing intensity is entirely due to mechanical distortion and not crystal lattice dislocations.

Before it can be installed in the ID beamline, the beam expanding system must be made capable of repeated reliable bending. The present system requires manual tightening of the pressure points which introduces too much variability. There is also some concern that the cylindrical frame places excessive force on the centre-line of the crystal, causing compression of the crystal lattice planes. This system could be replaced with a pseudo-four-bar-bender with a cylindrical block placed in near-contact to the crystal, using thermal paste to bridge the gap. This would retain the cooling abilities of the solid crystal frame while moving the bending pressure points away from the area of the crystal hit by the beam. This should improve the overall shape of the bending and eliminate distortions due to defects in the frame surface while still drawing out the high power of the ID beamline.

Another line of research opened by this system is a “beam compressor” for high-resolution micro-CT. Instead of expanding the beam vertically, the system could be turned around to compress the beam horizontally, producing a non-dispersive semi-monochromatic beam with very high flux. This could be used for 3D phase imaging of extremely small structures with very

fine detail, the exposure times for which would typically be unfeasible at BMIT using the existing monochromatic beam.

References

1. J. Als-Nielsen and D. McMorrow, *Elements of modern X-ray physics*. 2001, New York: Wiley.
2. V.V. Aristov, V.I. Polovinkina, I.M. Shmytko, and E.V. Shulakov, *Observation of the focusing of x-rays diffracted by a perfect crystal*. Jetp Letters, 1978. **28**(1): p. 4-7.
3. I. Ascone, W. Meyer-Klaucke, and L. Murphy, *Experimental aspects of biological X-ray absorption spectroscopy*. Journal of Synchrotron Radiation, 2003. **10**: p. 16-22.
4. A. Astolfo, E. Schultke, R.H. Menk, et al., *In vivo visualization of gold-loaded cells in mice using x-ray computed tomography*. Nanomedicine-Nanotechnology Biology and Medicine, 2013. **9**(2): p. 284-292.
5. B.W. Batterman and D.H. Bilderback, *X-ray monochromators and Mirrors*, in *Handbook on Synchrotron Radiation*, G.S. Brown and D.E. Moncton, Editors. 1991, North Holland: Amsterdam. p. 105-153.
6. J.H. Beaumont and M. Hart, *Multiple Bragg reflection monochromators for synchrotron-x radiation*. Journal of Physics E-Scientific Instruments, 1974. **7**(10): p. 823-829.
7. A. Bianco, G. Sostero, and D. Cocco, *Kirkpatrick-Baez elliptical bendable mirrors at the Nanospectroscopy beamline: Metrological results and x-rays performance*, in *X-Ray Mirrors, Crystals, and Multilayers II*, A.K. Freund, et al., Editors. 2002, Spie-Int Soc Optical Engineering: Bellingham. p. 74-85.
8. BMIT. *Beamline Diagram*. 2016; Available from: http://bmit.lightsource.ca/media/uploads/diagrams/BMIT_Overview_large.jpg.
9. U. Bonse, G. Materlik, and W. Schroder, *Perfect-crystal monochromators for synchrotron x-radiation*. Journal of Applied Crystallography, 1976. **9**(JUN1): p. 223-230.
10. A. Bravin, P. Coan, and P. Suortti, *X-ray phase-contrast imaging: from pre-clinical applications towards clinics*. Physics in Medicine and Biology, 2013. **58**(1): p. R1.
11. Y. Cauchois, *X ray spectrography by transmission of a nonchanneled beam through a curved crystal (I)*. Journal De Physique Et Le Radium, 1932. **3**: p. 320-336.
12. F.E. Christensen, A. Hornstrup, P. Frederiksen, et al., *A beam expander facility for studying x-ray optics*. Review of Scientific Instruments, 1992. **63**(1): p. 1168-1171.
13. Crystal_Scientific. *Cylindrical / Toroidal Mirrors*. 2011; Available from: http://www.crystal-scientific.com/mirror_cylindrical.html.
14. J. Dolbow and M. Gosz, *Effect of out-of-plane properties of a polyimide film on the stress fields in microelectronic structures*. Mechanics of Materials, 1996. **23**(4): p. 311-321.
15. M. Drakopoulos, T. Connolley, C. Reinhard, et al., *I12: the Joint Engineering, Environment and Processing (JEEP) beamline at Diamond Light Source*. Journal of Synchrotron Radiation, 2015. **22**: p. 828-838.
16. W. Ehrenberg, *X-Ray Optics*. Nature, 1947. **160**(4062): p. 330-331.

17. W. Ehrenberg and F. Jentzscht, *release of photo electrons via x-rays from metal mirror on the boundary of total reflection*. Zeitschrift Fur Physik, 1929. **54**(3-4): p. 227-235.
18. H. Ekstein, *Connection between the kinematic and dynamical theories of x-ray diffraction*. Physical Review, 1942. **62**(5/6): p. 255-261.
19. E. Erola, V. Eteläniemi, P. Suortti, et al., *X-ray reflectivity of bent perfect crystals in Bragg and Laue geometry*. Journal of Applied Crystallography, 1990. **23**(1): p. 35-42.
20. A. Fouras, B.J. Allison, M.J. Kitchen, et al., *Altered Lung Motion is a Sensitive Indicator of Regional Lung Disease*. Annals of Biomedical Engineering, 2012. **40**(5): p. 1160-1169.
21. A. Fouras, D. Lo Jacono, and K. Hourigan, *Target-free Stereo PIV: a novel technique with inherent error estimation and improved accuracy*. Experiments in Fluids, 2008. **44**(2): p. 317-329.
22. S. Goto, K. Takeshita, Y. Suzuki, et al., *Construction and commissioning of a 215-m-long beamline at Spring-8*. Nuclear Instruments and Methods in Physics Research Section A: Accelerators, Spectrometers, Detectors and Associated Equipment, 2001. **467**: p. 682-685.
23. J.B. Hastings, *X-ray optics and monochromators for synchrotron radiation*. Journal of Applied Physics, 1977. **48**(4): p. 1576-1584.
24. O. Hignette, P. Cloetens, W.K. Lee, et al., *Hard X-ray microscopy with reflecting mirrors status and perspectives of the ESRF technology*. Journal De Physique Iv, 2003. **104**: p. 231-234.
25. S.B. Hooper, M.J. Kitchen, M.L.L. Siew, et al., *Imaging lung aeration and lung liquid clearance at birth using phase contrast X-ray imaging*. Clinical and Experimental Pharmacology and Physiology, 2009. **36**(1): p. 117-125.
26. J.H. Hubbell and S.M. Seltzer. *Tables of X-Ray Mass Attenuation Coefficients and Mass Energy-Absorption Coefficients (version 1.4)*. 2004; Available from: <http://physics.nist.gov/xaamdi>.
27. K. Hyodo, M. Ando, Y. Oku, et al., *Development of a two-dimensional imaging system for clinical applications of intravenous coronary angiography using intense synchrotron radiation produced by a multipole wiggler*. Journal of Synchrotron Radiation, 1998. **5**(3): p. 1123-1126.
28. G. Illing, J. Heuer, B. Reime, et al., *Double-beam bent Laue monochromator for coronary angiography*. Review of Scientific Instruments, 1995. **66**(2): p. 1379-1381.
29. Instrument_Design_Technology_Ltd. *Product Guide*. 2016; Available from: http://idtnet.co.uk/downloads/IDT_product_guide.pdf.
30. D.T. Jiang, N. Chen, and W. Sheng, *Wiggler-base hard x-ray spectroscopy beamline at CLS*, in *Synchrotron Radiation Instrumentation, Pts 1 and 2*, J.Y. Choi and S. Rah, Editors. 2007, Amer Inst Physics: Melville. p. 800-803.
31. S. Kawado, S. Iida, S. Yamaguchi, et al., *Synchrotron-radiation X-ray topography of surface strain in large-diameter silicon wafers*. Journal of Synchrotron Radiation, 2002. **9**: p. 166-168.

32. S. Kimura, J. Harada, and T. Ishikawa, *Comparison between Experimental and Theoretical Rocking Curves in Extremely Asymmetric Bragg Cases of X-ray Diffraction*. Acta Crystallographica Section A, 1994. **50**: p. 337-342.
33. P. Kirkpatrick and A.V. Baez, *Formation of optical images by X-rays*. Journal of the Optical Society of America, 1948. **38**(9): p. 766-774.
34. N. Kujala, S. Marathe, D.M. Shu, et al., *Kirkpatrick-Baez mirrors to focus hard X-rays in two dimensions as fabricated, tested and installed at the Advanced Photon Source*. Journal of Synchrotron Radiation, 2014. **21**: p. 662-668.
35. A.R. Lang, *The projection topograph: a new method in X-ray diffraction microradiography*. Acta Crystallographica, 1959. **12**(3): p. 249-250.
36. R.A. Lewis, *Medical phase contrast x-ray imaging: current status and future prospects*. Physics in Medicine and Biology, 2004. **49**(16): p. 3573-3583.
37. R.A. Lewis, J. Bordas, and F.E. Christensen, *Test facility for astronomical x-ray optics*. Optical Engineering, 1990. **29**(8): p. 942-945.
38. R.A. Lewis, N. Yagi, M.J. Kitchen, et al., *Dynamic imaging of the lungs using x-ray phase contrast*. Physics in Medicine and Biology, 2005. **50**(21): p. 5031-5040.
39. W.J. Liu, G.E. Ice, J.Z. Tischler, et al., *Short focal length Kirkpatrick-Baez mirrors for a hard x-ray nanoprobe*. Review of Scientific Instruments, 2005. **76**(11): p. 6.
40. Y. Liu, J. Nelson, C. Holzner, et al., *Recent advances in synchrotron-based hard x-ray phase contrast imaging*. Journal of Physics D: Applied Physics, 2013. **46**(49): p. 494001.
41. A. Macrander, M. Erdmann, N. Kujala, et al., *X-ray optics testing beamline 1-BM at the advanced photon source*. AIP Conference Proceedings, 2016. **1741**(1): p. 030030.
42. P.H. Mao, F.A. Harrison, Y.Y. Platonov, et al., *Development of grazing incidence multilayer mirrors for hard X-ray focusing telescopes*. Eux, X-Ray, and Gamma-Ray Instrumentation for Astronomy Viii, ed. O.H.W. Siegmund and M.A. Gummin. Vol. 3114. 1997, Bellingham: Spie - Int Soc Optical Engineering. 526-534.
43. M. Martinson and D. Chapman, *Measuring the criticality of the 'magic condition' for a beam-expanding monochromator*. Journal of Synchrotron Radiation, 2016. **23**(6): p. 1498-1500.
44. M. Martinson, R.A. Lewis, A. Fouras, et al., *Indirect measurement of average alveolar dimension using dynamic phase-contrast imaging*. World Congress on Medical Physics and Biomedical Engineering, 2015. **51**: p. 166-168.
45. M. Martinson, N. Samadi, B. Bassey, et al., *Phase-preserving beam expander for biomedical X-ray imaging*. Journal of Synchrotron Radiation, 2015. **22**(3): p. 801-6.
46. M. Martinson, N. Samadi, G. Belev, et al., *Development of a bent Laue beam-expanding double-crystal monochromator for biomedical X-ray imaging*. Journal of Synchrotron Radiation, 2014. **21**(Pt 3): p. 479-83.
47. H. Mimura, S. Morita, T. Kimura, et al., *Fabrication of a 400-mm-long mirror for focusing X-ray free-electron lasers to sub-100 nm*, in *Advances in X-Ray/Euv Optics and Components Iii*,

A.M. Khounsary and C. Morawe, Editors. 2008, Spie-Int Soc Optical Engineering: Bellingham.

48. P. Penning and D. Polder, *Anamolous transmission of x-rays in elastically deformed crystals*. Philips Research Reports, 1961. **16**: p. 419-440.
49. P.V. Petrashen and E.N. Kislovskii, *Experimental-study of the x-ray-diffraction in a bent crystal with a large strain gradient*. Physica Status Solidi a-Applied Research, 1979. **56**(2): p. 663-667.
50. L. Porra, H. Suhonen, P. Suortti, et al., *Effect of positive end-expiratory pressure on regional ventilation distribution during bronchoconstriction in rabbit studied by synchrotron radiation imaging*. Critical Care Medicine, 2011. **39**(7): p. 1731-1738.
51. I.V. Pratt, G. Belev, N. Zhu, et al., *In vivo imaging of rat cortical bone porosity by synchrotron phase contrast micro computed tomography*. Phys Med Biol, 2014. **60**(1): p. 211-232.
52. B.R. Ren, *A bent Laue-Laue monochromator for a synchrotron-based monochromatic x-ray computed tomography system*. Medical Physics, 1998. **25**(12): p. 2483-2483.
53. E. Schültke, M.E. Kelly, C. Nemoz, et al., *Dual energy CT at the synchrotron: a piglet model for neurovascular research*. European journal of radiology, 2011. **79**(2): p. 323-327.
54. C. Schulze, G. Heidenreich, H. Auderset, et al., *A novel monochromator concept for sagittal micro-focussing of undulator radiation*, in *Crystal and Multilayer Optics*, A.T. Macrander, et al., Editors. 1998, Spie-Int Soc Optical Engineering: Bellingham. p. 156-165.
55. C. Schulze, U. Lienert, M. Hanfland, et al., *Microfocusing of Hard X-rays with Cylindrically Bent Crystal Monochromators*. Journal of Synchrotron Radiation, 1998. **5**(2): p. 77-81.
56. S.D. Shastri, K. Fezzaa, A. Mashayekhi, et al., *Cryogenically cooled bent double-Laue monochromator for high-energy undulator X-rays (50-200 keV)*. Journal of Synchrotron Radiation, 2002. **9**: p. 317-322.
57. S.E. Soutiere, C.G. Tankersley, and W. Mitzner, *Differences in alveolar size in inbred mouse strains*. Respiratory Physiology & Neurobiology, 2004. **140**(3): p. 283-291.
58. D. Spiga, G. Pareschi, C. Pelliciari, et al., *Functional tests of modular elements of segmented optics for X-ray telescopes via an expanded beam facility*, in *Space Telescopes and Instrumentation 2012: Ultraviolet to Gamma Ray*, T. Takahashi, S.S. Murray, and J.W.A. DenHerder, Editors. 2012, Spie-Int Soc Optical Engineering: Bellingham.
59. P. Suortti, *Focusing monochromators for high-energy synchrotron radiation*. Review of Scientific Instruments, 1992. **63**(1): p. 942-945.
60. P. Suortti, U. Lienert, and C. Schulze, *Bent crystal optics for high energy synchrotron radiation*, in *X-Ray and Inner-Shell Processes - 17th International Conference*, R.L. Johnson, H. Schmidtböcking, and B.F. Sonntag, Editors. 1997, Aip Press: Woodbury. p. 175-192.
61. P. Suortti and C. Schulze, *Fixed-Exit Monochromators for High-Energy Synchrotron Radiation*. Journal of Synchrotron Radiation, 1995. **2**(1): p. 6-12.

62. P. Suortti and W. Thomlinson, *Medical applications of synchrotron radiation*. Physics in Medicine and Biology, 2003. **48**(13): p. R1.
63. P. Suortti, W. Thomlinson, D. Chapman, et al., *A single crystal bent Laue monochromator for coronary angiography*. Nuclear Instruments & Methods in Physics Research Section a-Accelerators Spectrometers Detectors and Associated Equipment, 1993. **336**(1-2): p. 304-309.
64. J.P. Sutter, T. Connolley, M. Drakopoulos, et al., *Ray traces of an arbitrarily deformed double-crystal Laue X-ray monochromator*, in *Advances in X-Ray/Euv Optics and Components Iii*, A.M. Khounsary and C. Morawe, Editors. 2008, Spie-Int Soc Optical Engineering: Bellingham.
65. A. Takeuchi, Y. Suzuki, and H. Takano, *High-resolution X-ray microbeam by using a Kirkpatrick-BaezType mirror at SPring-8*. Journal De Physique Iv, 2003. **104**: p. 235-238.
66. W. Thomlinson, P. Suortti, and D. Chapman, *Recent advances in synchrotron radiation medical research*. Nuclear Instruments & Methods in Physics Research Section a-Accelerators Spectrometers Detectors and Associated Equipment, 2005. **543**(1): p. 288-296.
67. A.C. Thompson, Y. Wu, J.H. Underwood, and T.W. Barbee, *Focusing of synchrotron radiation x-ray-beams using synthetic multilayer mirrors*. Nuclear Instruments & Methods in Physics Research Section a-Accelerators Spectrometers Detectors and Associated Equipment, 1987. **255**(3): p. 603-605.
68. A.P.L. Turner, T. Vreeland, Jnr, and D.P. Pope, *Experimental techniques for observing dislocations by the Berg-Barrett method*. Acta Crystallographica Section A, 1968. **24**(4): p. 452-458.
69. M. von Laue, *Wave optics*. Encyclopedia of mathematical sciences with inclusion of their applications, 1915. **5**(3): p. 359-487.
70. T.W. Wysokinski, D. Chapman, G. Adams, et al., *Beamlines of the biomedical imaging and therapy facility at the Canadian light source - Part I*. Nuclear Instruments & Methods in Physics Research Section a-Accelerators Spectrometers Detectors and Associated Equipment, 2007. **582**(1): p. 73-76.
71. T.W. Wysokinski, D. Chapman, G. Adams, et al., *Beamlines of the Biomedical Imaging and Therapy Facility at the Canadian Light Source - Part 2*. 11th International Conference on Synchrotron Radiation Instrumentation (Sri 2012), 2013. **425**.
72. H. Yamaguchi and H. Matsuhata, *Threading Screw Dislocations in 4H-SiC Wafer Observed by the Weak-Beam Method in Bragg-Case X-ray Topography*. Journal of Electronic Materials, 2010. **39**(6): p. 715-718.
73. W.H. Zachariasen, *Theory of X-ray diffraction in crystals*. 1945, New York : London: J. Wiley; Chapman & Hall.
74. Y. Zhu, N. Samadi, M. Martinson, et al., *Spectral K-edge subtraction imaging*. Phys Med Biol, 2014. **59**(10): p. 2485-2503.
75. F. Zontone and F. Comin, *Heat load and anticlastic effect compensation on an ESRF monochromator: An exhaustive ray-tracing study for a meridional-sagittal geometry*. Review of Scientific Instruments, 1992. **63**(1): p. 501-504.

Appendix I Reuse Licenses for Papers and Figures

License	Paper reference	Author	Reuse content	Reuse location
I.1	{Kirkpatrick 1948}	Kirkpatrick & Baez	Figure 11	Figure 1.5
I.2	{Martinson 2015}	Martinson et al.	Full paper (reformatted)	Chapter 3
I.3	{Martinson 2014}	Martinson et al.	Full paper (reformatted)	Chapter 4
I.4	{Martinson 2015}	Martinson et al.	Full paper (reformatted)	Chapter 5
I.5	{Martinson 2016}	Martinson et al.	Full paper (reformatted)	Chapter 6

I.1

Subject: RE: request to reproduce a figure

From: pubscopyright <copyright@osa.org>

Date: 2016-08-09 12:51

To: Mercedes Martinson <mercedes.m@usask.ca>, pubscopyright <copyright@osa.org>

Dear Mercedes Martinson,

Thank you for contacting The Optical Society.

OSA considers your requested use of its copyrighted material to be Fair Use under United States Copyright Law. It is requested that a complete citation of the original material be included in any publication.

Let me know if you have any questions.

Kind Regards,
Rebecca Robinson

Rebecca Robinson
August 9, 2016
Authorized Agent, The Optical Society

-----Original Message-----

From: Mercedes Martinson [mailto:mercedes.m@usask.ca]

Sent: Saturday, August 06, 2016 11:12 PM

To: pubscopyright

Subject: request to reproduce a figure

Hello,

I am writing to request permission to reproduce a figure.

Citation:

Kirkpatrick, P. and A.V. Baez, FORMATION OF OPTICAL IMAGES BY X-RAYS.
Journal of the Optical Society of America, 1948. 38(9): p. 766-774.

Figure number: 11

Intended use of the item: Inclusion in my PhD dissertation with full reference and credit provided.

Contact information:

Mercedes Martinson
Department of Physics and Engineering Physics University of Saskatchewan
116 Science Place, Rm 163
Saskatoon, SK S7N 5E2
CANADA
mercedes.m@usask.ca
1-306-966-6393

Thank you and regards,
Mercedes Martinson

I.2

SPRINGER LICENSE TERMS AND CONDITIONS

Aug 11, 2016

This Agreement between Mercedes J Martinson ("You") and Springer ("Springer") consists of your license details and the terms and conditions provided by Springer and Copyright Clearance Center.

License Number	3925730207037
License date	Aug 11, 2016
Licensed Content Publisher	Springer
Licensed Content Publication	Springer eBook
Licensed Content Title	Indirect measurement of average alveolar dimension using dynamic phase-contrast imaging
Licensed Content Author	M. Martinson
Licensed Content Date	Jan 1, 2015
Type of Use	Thesis/Dissertation
Portion	Full text
Number of copies	100
Author of this Springer article	Yes and you are the sole author of the new work
Order reference number	
Title of your thesis / dissertation	Bent Laue X-ray Beam Expander
Expected completion date	Oct 2016
Estimated size(pages)	100
Requestor Location	Mercedes J Martinson 116 Science Place, Rm 163 Saskatoon, SK S7N 5E2 Canada Attn: Mercedes J Martinson
Billing Type	Invoice
Billing Address	Mercedes J Martinson 116 Science Place, Rm 163 Saskatoon, SK S7N 5E2 Canada Attn: Mercedes J Martinson
Total	0.00 CAD

I.3

Subject: Re: Request to reproduce an article

From: Tony Weight <tw@iucr.org>

Date: 2016-08-11 02:22

To: Mercedes Martinson <mercedes.m@usask.ca>

CC: Tony Weight tw@iucr.org

Dear Mercedes

Thank you for your email.

Permission is hereby granted, on behalf of the IUCr, for you to reproduce the material specified below, subject to the following conditions:

1. Reproduction is intended in a primary journal, secondary journal, CD-ROM, book or thesis.
2. The original article in which the material appeared is cited.
3. IUCr's copyright permission is indicated next to the article in print. In electronic form, this acknowledgement must be visible at the same time as the article, and must be hyperlinked to the article (<http://dx.doi.org/10.1107/S1600577514003014>).

Material specified:

Article 'Development of a bent Laue beam-expanding double-crystal monochromator for biomedical X-ray imaging'

Martinson, M., Samadi, N., Belev, G., Bassey, B., Lewis, R., Aulakh, G. & Chapman, D. (2014). *J. Synchrotron Rad.* 21, 479-483.

With best wishes,

Tony

~ ~

Tony Weight

Managing Editor

Journal of Synchrotron Radiation

International Union of Crystallography

5 Abbey Square

Chester CH1 2HU

England

Tel: +44 1244 342878

Fax: +44 1244 314888

Email: tw@iucr.org

WWW: <http://www.iucr.org>

I.4

Subject: Re: Request to reproduce an article
From: Tony Weight <tw@iucr.org>
Date: 2016-08-12 03:40
To: "Martinson, Mercedes" <mercedes.m@usask.ca>
CC: Tony Weight tw@iucr.org

Dear Dr Mercedes

Thank you for your email.

Permission is hereby granted, on behalf of the IUCr, for you to reproduce the material specified below, subject to the following conditions:

1. Reproduction is intended in a primary journal, secondary journal, CD-ROM, book or thesis.
2. The original article in which the material appeared is cited.
3. IUCr's copyright permission is indicated next to the article in print. In electronic form, this acknowledgement must be visible at the same time as the article, and must be hyperlinked to the article (<http://dx.doi.org/10.1107/S1600577515004695>).

Material specified:

Article 'Phase-preserving beam expander for biomedical X-ray imaging'
M. Martinson, N. Samadi, B. Bassey, A. Gomez and D. Chapman (2015). J. Synchrotron Rad. 22, 801-806.

With best wishes,

Tony

~ ~ ~ ~ ~ ~ ~ ~ ~ ~ ~ ~ ~ ~ ~ ~ ~ ~ ~

Tony Weight

Managing Editor

Journal of Synchrotron Radiation
International Union of Crystallography

5 Abbey Square

Chester CH1 2HU

England

Tel: +44 1244 342878

Fax: +44 1244 314888

Email: tw@iucr.org

WWW: <http://www.iucr.org>

I.5

Subject: Re: Electronic reprint of your article YI5024

From: Tony Weight <tw@iucr.org>

Date: 2016-10-27 10:53

To: "Martinson, Mercedes" <mercedes.m@usask.ca>

CC: Tony Weight tw@iucr.org

Dear Dr Martinson

Thank you for your email.

Permission is hereby granted, on behalf of the IUCr, for you to reproduce the material specified below, subject to the following conditions:

1. Reproduction is intended in a primary journal, secondary journal, CD-ROM, book or thesis.
2. The original article in which the material appeared is cited.
3. IUCr's copyright permission is indicated next to the Figure in print. In electronic form, this acknowledgement must be visible at the same time as the Figure, and must be hyperlinked to the article (<http://dx.doi.org/10.1107/S1600577516012650>).

Material specified:

Article 'Measuring the criticality of the 'magic condition' for a beam-expanding monochromator'

Martinson, M. & Chapman, D. (2016). J. Synchrotron Rad. 23, 1498-1500.

With best wishes,

Tony

~ ~

Tony Weight

Managing Editor

Journal of Synchrotron Radiation

International Union of Crystallography

5 Abbey Square

Chester CH1 2HU

England

Tel: +44 1244 342878

Fax: +44 1244 314888

Email: tw@iucr.org

WWW: <http://www.iucr.org>

Appendix II Technical & experimental details for installation & testing

II.1 Technical specifications of RMD bending frames

The RMD bending frames (RMD Engineering Inc., Saskatoon, SK, Canada) have been fabricated in a variety of sizes. One set of frames have been manufactured to accommodate crystal wafers up to 12" in diameter. The other set has been manufactured to accommodate crystal wafers up to 6" in diameter. The schematics (Figure II.1) are provided for the 6" frames. For each bending radius, the apparatus consists of a solid metal bending plate machined with a curvature of the appropriate bending radius (0.5 m and 5.636 m for the first and second crystals, respectively) such that the crystal will be cylindrically bent in the diffraction plane. The 0.5 m frame has been manufactured from nickel-plated copper for in-vacuum compatibility. The copper acts as an excellent heat-sink material, while the nickel-plating prevents dissolving of the copper by the Indium-Gallium paste applied to the surface to improve heat dissipation. The crystals are held in place and forced to the appropriate bending radius by solid steel retaining bars. The bending plates are mounted on support frames that can be attached to the rotating stages for crystal alignment, and that can also be rotated themselves within the supports for coarse alignment. The 0.5 m support frame is water-cooled to dissipate heat caused by absorption of the white ID beam, and the support plate is also nickel-plated to protect against damage by In-Ga leakage.

II.2 Mounting crystals on frames & frames in beamline

Before attempting to mount any of the experimental crystals, acquire some inexpensive crystals to practice on. Even if you have experience bending crystals, these are bent to within microns of breaking and may present a special challenge. When practicing, deliberately misalign the crystal flats with respect to the frame edges, as crystals will readily cleave along atomic planes of small Miller indices (*e.g.* (1,1,1), (2,2,0)) and may be impossible to mount on the 0.5 m frame without breaking.

These instructions are for the RMD-made frames with proper mounting hardware. Take special care not to cause any damage whatsoever to the frame surface as this will severely degrade the beam quality, especially the second crystal frame.

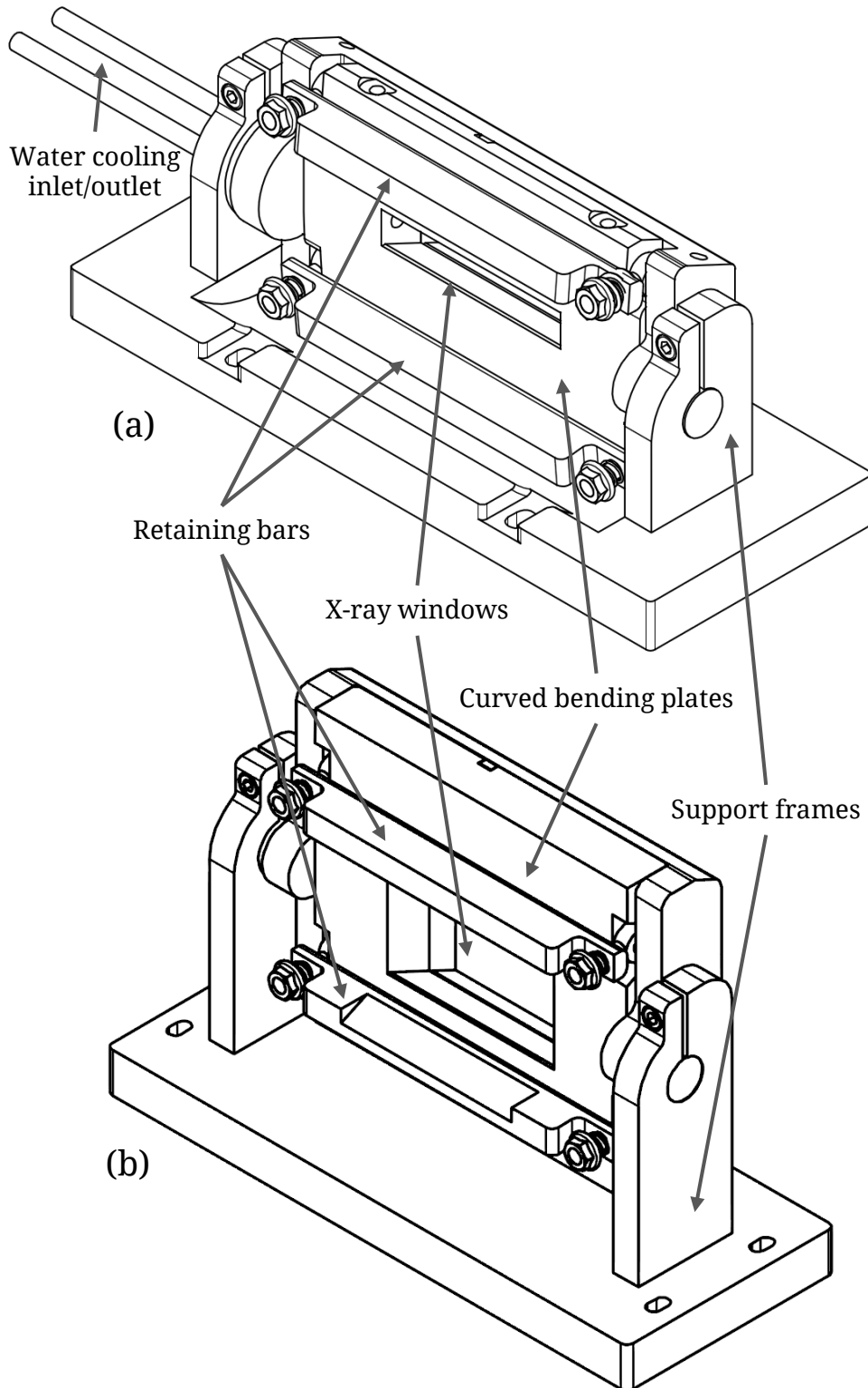


Figure II.1 Diagram of (a) 0.5 m and (b) 5.636 m RMD bending frames and related components

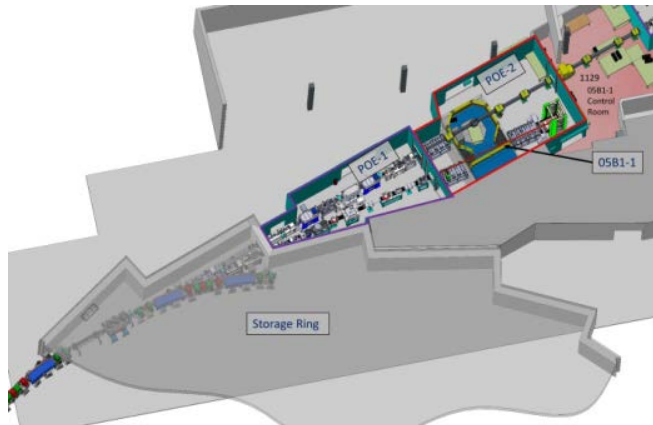


Figure II.2 Beamlne diagram {Bmit 2016}

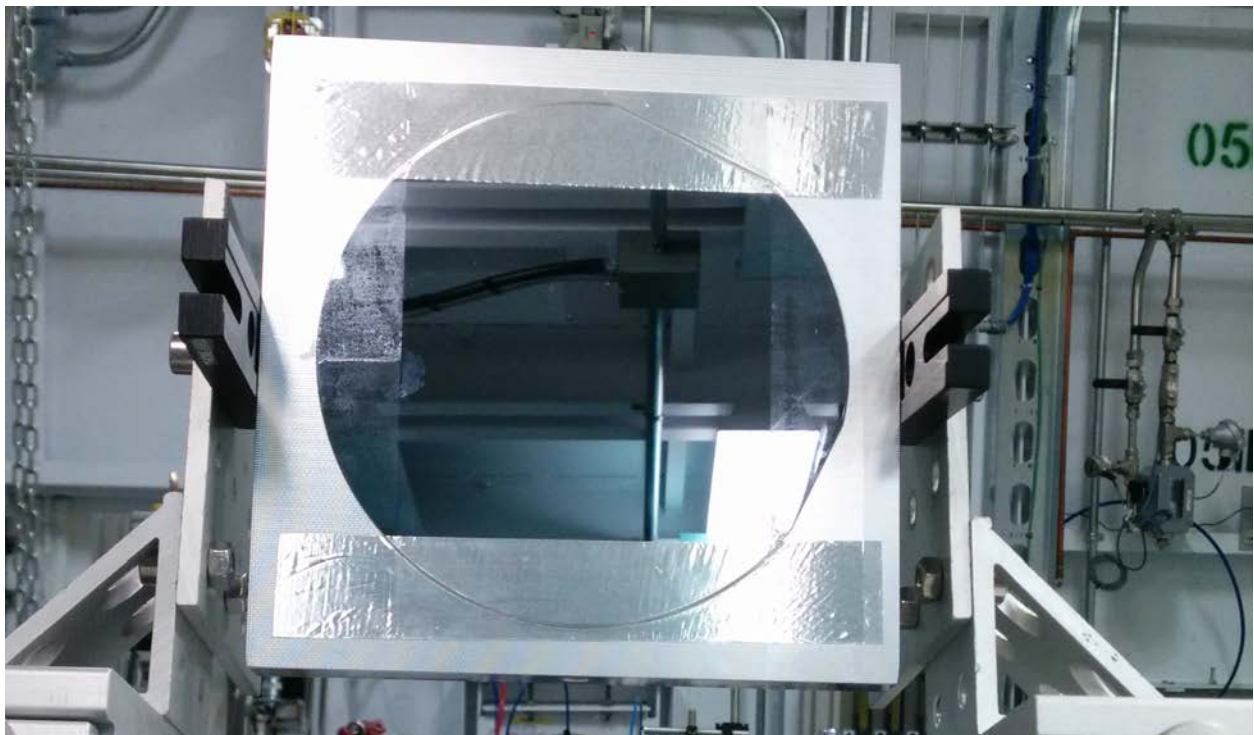


Figure II.3 Orientation of crystal on frame, looking at the convex side of the second crystal. Shown is older wafer with two flats. Single flat on newer wafers corresponds to shorter flat (lower-right).

First thoroughly clean the bending frame and both sides of the crystal using ethanol and Kim wipes. Using the alignment template (Figure II.4 or download pdf using link in caption) and a fine Sharpie, mark the flat you need to use (the single flat on the newer (5,1,1) wafers corresponds to the smaller flat on the older (5,1,1) wafers so align accordingly). Alignment of the crystal to the frame is shown in Figure II.1 (older wafer with two flats).

Align the crystal flat to the marking and gently tape in place to secure while bending. Apply bending bars to one side, making sure to include Belleville washers to equalize pressure

and ball bearing washers to reduce friction. Carefully tighten bars, making sure to tighten each nut with equal pressure. Don't allow the crystal to twist in any way, even from the light tape. After first bar is down, remove tape. Then apply second bending bar and very carefully bend the crystal. Ensure there are no gaps between crystal and bending frame. If installing to ID beamline, include a thin layer of InGa thermal paste to the first frame (WARNING: you only get one shot! Frames are nickel-plated to minimize chemical reaction between thermal paste and metal frame, but crystallization of the metal will begin to occur so crystal should not be removed once applied with paste!)

For installing the beam expander in the BM hutch (POE-2), the first crystal should be placed on the first table nearest the beam entrance port. Two crossed goniometers should be placed with the “pitch” stage on the bottom and the “roll” stage on top. The first expander frame is then mounted on the top stage with the concave side facing the source and no tilt angle (*i.e.* perpendicular to the beam). The second frame is placed at the top of the inclined rails in a similar arrangement to the first (Figure II.3).

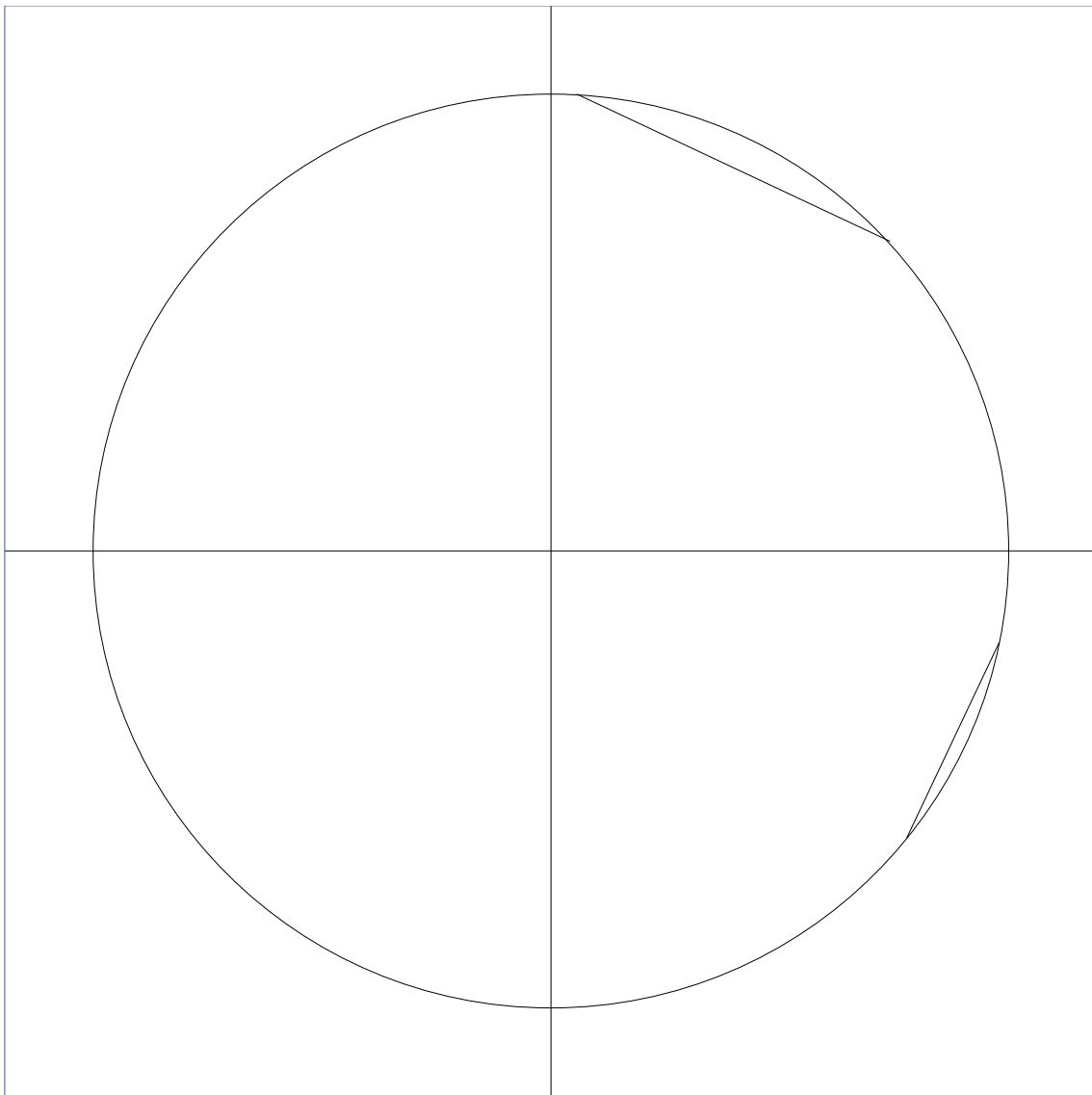


Figure II.4 Template for mounting crystal to frame.
(<https://www.dropbox.com/s/bbnzwhzf3nkuab/xtal-align.pdf?dl=1>)

II.3 Aligning crystals

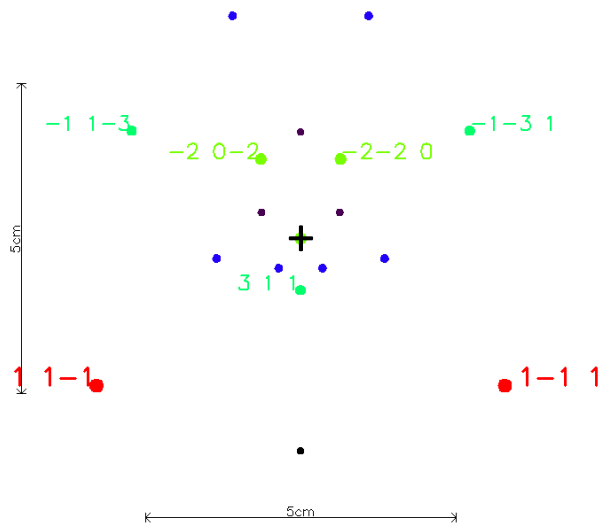


Figure II.5 Laue transmission mapping for (5,1,1) crystal perpendicular to the beam, showing the (3,1,1) reflection below the direct beam which is marked by the cross at the centre.

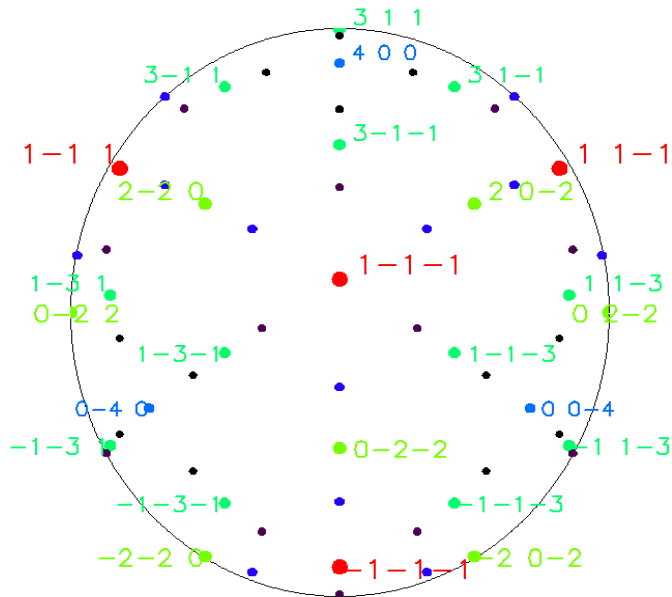


Figure II.6 Stereographic projection of Si(5,1,1) wafer with (3,1,1) reflection on the perimeter.

This description assumes a Si(5,1,1) wafer with (3,1,1)-type reflection. Refer to Laue transmission mapping in Figure II.5 and the stereographic projection in Figure II.6. Place a fluorescent screen downstream from the first crystal with the fluorescent surface downstream. Block the direct beam with several layers of lead tape on the upstream surface of the screen to

avoid damaging the screen. Place a lead brick on the shelf after the screen to avoid damaging equipment in the hutch and minimise scatter. With the beam on and a camera focused on the fluorescent screen, note whether the (3,1,1) reflection is above or below the direct beam. In order to match the geometric and single-ray focal points, the first crystal must be in the $\chi + \theta_B$ orientation, which occurs when the (3,1,1) reflection is initially below the direct beam and then is rocked by $2\chi + \theta_B$ to bring it above the direct beam and to the appropriate Bragg angle for the energy. If it is above, rotate the frame 180° around the beam (*i.e.* in the z-axis), placing the reflection below the direct beam.

Align the first crystal to the iodine K-edge as follows. Turn off the beam and manually tilt the frame to 77° from horizontal to bring the Bragg angle to within range of the iodine K-edge. Place a sample of iodine solution upstream from the first crystal (be sure to protect against spills as the white beam can burn holes through the container and leak iodine; I use a layer of the plastic-backed absorbent sheets from the animal prep lab). Slowly rock the first crystal back and forth in Bragg, increasing range each pass, until you see the (3,1,1) spot go through the k-edge (it should be obvious if you have enough iodine). To confirm, try to rock the crystal by $\theta_B = 6.6^\circ$ (the Bragg angle for Iodine at (3,1,1)) twice so that it passes through the direct beam and then goes through the k-edge again on the other side (*note:* the stage may run out of range and/or the centre of rotation may be offset from the middle of the bending frame window, causing the frame to block the beam, so this may not be possible). Now the first crystal is aligned to the iodine k-edge, place a smaller screen on the second crystal in order to locate the position of the beam at the second crystal.

Place second crystal at a distance of $\frac{1}{2}(R_2 - R_1)$ from the first crystal and oriented the same way. Translate the second crystal vertically and horizontally in order to centre the beam on the window. Use a digital protractor to measure the tilt of the first crystal and manually align the second crystal to this angle for coarse alignment. Then place a fluorescent screen behind the second crystal. Right away you will see one beam diffracted by the first crystal and directly transmitted through the second crystal. Rock the Bragg very slowly until you see two beams. The double-diffracted beam will appear below the transmitted beam and should be similar in shape and size. Sometimes false reflections will appear as narrow diagonal smears across the screen – *these aren't the beams you're looking for.* If the beam is not the same shape, try moving the second crystal up/downstream on the rails to exactly match the geometric focal points of both crystals.

II.4 Testing

Testing of mounted crystals can be performed as per the procedures described in Chapter 7. The most accessible method at the beamline is the Laue-Laue rocking curve topography. A flat

panel detector with a large field of view can be used to observe the entire width of the crystal in a single exposure, allowing quick survey of the crystal to find any distortions. The FARO arm can mar the crystal surface and especially the frame so physical measurements are not recommended on equipment expected to be installed permanently.

Testing of the expander system is achieved by setting up both crystals as described above in the BM beamline and imaging suitable test objects. Generally a vertical extension must be installed on the translation stages in order to lift the sample into the beam. For permanent installation to the ID beamline, the large animal lift has adequate range to reach the beam.